



UNIVERSITÀ
DEGLI STUDI
DI BRESCIA

DIPARTIMENTO DI INGEGNERIA CIVILE, ARCHITETTURA,
TERRITORIO, AMBIENTE E DI MATEMATICA

Corso di Laurea Magistrale
in Civil and Environmental Engineering

Tesi di Laurea

Enhanced resolution mapping of melting over the Greenland
and Antarctica ice sheets (1979 - 2016) using passive microwave
brightness temperatures

Relatore: Prof. Roberto Ranzi
Correlatore: Prof. Marco Tedesco

Laureando:
Paolo Colosio
Matricola n. 706113

Anno Accademico 2018/2019

Index

Abstract.....	1
Sommario.....	3
Acknowledgements	6
Section 1	7
1 Introduction	8
2 Continental ice sheet melting and sea level rise.....	12
References of section 1.....	22
Section 2	24
3 Remote sensing of the cryosphere	25
4 Enhanced resolution passive microwave data	36
References of section 2.....	64
Section 3	68
5 Snowmelt over Greenland and Antarctica.....	69
6 Conclusions.....	101
References of section 3.....	103
Appendix	107

Abstract

The cryosphere is a main component in climatic and hydrological processes, interacting with the other parts of the climate system. Defined as the portion of Earth where water is in its solid form, it is a sensitive indicator of changes in climatic conditions. In particular, the arctic regions have been affected by the strongest variations in climate parameters, presenting the highest increment in average temperature recorded on the planet. One of the components of the cryosphere are the Antarctica and Greenland ice sheets, holding the 70 of freshwater on Earth and being crucial in the assessment of water resources. Surface mass balance and ice loss of the biggest masses of ice on the Earth are also a direct term into the mass balance for the calculation of sea level rise. Long term analysis of the parameters indicating changes in climatic conditions are thus of paramount importance. One of these parameters is the surface melting on glaciated surfaces.

Surface melting plays a key role on the ice sheet surface mass balance and ice dynamics with changes in surface melting spatial patterns potentially affecting hydrological processes, supraglacially, englacially and subglacially. Passive microwave (PMW) brightness temperature observations are of paramount importance in studying long-term climate and earth surface processes. Specifically, PMW data are characterized by large temporal coverage (1979-2018) and high temporal resolution (at least daily) due to the capability of microwave data to be collected in all-weather conditions. However, a major limitation of PMW datasets has been the relatively coarse spatial resolution.

Here, after a presentation of the impact of climate change on cryosphere components and a summary of basic principles of passive microwave remote sensing, describing the electromagnetic properties of snow and ice, we assess the potential of an enhanced spatial resolution (3.125 km) passive microwave dataset recently made available through the NASA MeASURES program.

At first, we present the data characteristics, compare data from different sensors providing linear relations to intercalibrate SMMR and SSM/I sensors over Greenland and Antarctica ice sheets in order to build the full 37 years dataset of brightness temperatures.

Then, we assess five different threshold-based melt detection algorithms by using surface/air temperature data from automatic weather stations and compare the outputs of the

selected algorithms applied to the high resolution dataset with the coarser resolution data by means of the outputs of a regional climate model (MAR).

Finally, we discuss long term trends of the main indicators of melting season at pixel scale, melt onset date (MOD), melt end date (MED) and melt duration (MD), and synthetic parameters, mean melt duration (MMD), melting index (MI) and maximum melting surface (MMS) obtaining 95% statistically significant trends, with higher confidence on the results obtained for Greenland. Then, the example of the extreme melt event occurred in 2012 is presented.

We showed the capability of the enhanced resolution product to detect and map surface melting over Greenland and Antarctica, providing a melting maps dataset at unprecedented spatial resolution and temporal coverage.

Sommario

La criosfera è uno degli elementi principali del sistema climatico, interagendo le altre componenti di questo ed influenzando i processi idrologici. Definita come la frazione della terra in cui l'acqua si trova al suo stato solido, è una importante sentinella dei cambiamenti del sistema climatico, come indicano sempre più recenti studi ed osservazioni, anche nel panorama italiano. Si pensi al processo di ritiro dei ghiacciai della catena Alpina, primo tra tutti il ghiacciaio dell'Adamello (Ranzi et al., 2010). Riportano però i più significativi cambiamenti i ghiacciai nella regione Artica, zona del globo in cui è stato misurato il più forte aumento della temperatura media. Tra le parti della criosfera polare, le calotte di ghiaccio di Groenlandia ed Antartide rappresentano le più grandi riserve di acqua dolce del pianeta, conservandone in stato solido il 70%. Il loro studio è quindi fondamentale in un'ottica di gestione delle risorse idriche. Inoltre, il contributo del bilancio di massa superficiale e le perdite di grandi masse di ghiaccio sono un diretto contributo nel calcolo dell'innalzamento del livello medio del mare. Sono quindi di grande importanza le analisi a lungo termine dei parametri che possano indicare cambiamenti delle condizioni climatiche. Uno di questi parametri è la fusione superficiale del manto nevoso sulle superfici glacializzate.

La fusione superficiale svolge infatti un ruolo chiave per le calotte di ghiaccio sia per quanto riguarda il bilancio di massa superficiale, sia per la valutazione dinamica dei ghiacciai. La neve, una volta fusa e trasformata in deflusso superficiale può infatti defluire sulla superficie glacializzata oppure, tramite passaggi all'interno della massa ghiaccio (i mulini glaciali), raggiungere zone intermedie o basali delle calotte, influenzando e accelerando i processi idrologici e dinamici a livello supraglaciale, endoglaciale e subglaciale.

Il telerilevamento tramite a sensori a microonde passivi, che misurano la temperatura di brillantezza naturalmente emessa dalla superficie terrestre, svolge un ruolo di primaria importanza nello studio dei processi climatici e le variazioni di questi su grande scala temporale e spaziale.

Nello specifico, i dati ottenuti da telerilevamento satellitare a microonde passivo sono caratterizzati da una grande copertura temporale (1979-oggi), una vasta copertura spaziale che li rende applicabili a studi su larga scala e un'alta risoluzione temporale grazie alla proprietà delle onde elettromagnetiche nelle frequenze delle microonde di non essere influenzati dalla copertura delle nuvole e alla possibilità di ottenere anche misure notturne non essendo necessaria la

radiazione solare per i sensori passivi. Il limite principale di questi sensori era la relativamente bassa risoluzione spaziale.

In questo lavoro di tesi, dopo una introduzione relativa agli impatti del cambiamento climatico sul ciclo idrologico, le risorse idriche e, in particolare, la criosfera ed un riassunto dei principi generali del telerilevamento passivo, descrivendo le proprietà elettromagnetiche di neve e ghiaccio, vengono presentate le potenzialità di un nuovo dataset a migliorata risoluzione spaziale recentemente reso disponibile dal programma NASA MeASURES. La risoluzione disponibile tramite questo prodotto varia a seconda della frequenza del canale selezionato, raggiungendo un miglioramento massimo da 25 km a 3.125 km.

Per prima cosa sono stati presentate le caratteristiche del dataset, con attenzione alla banda selezionata (37 GHz, polarizzazione orizzontale). Sono stati poi confrontati i dati provenienti dai diversi sensori selezionati (SMMR, SSM/I-F08, SSM/I-F11, SSM/I-F13 e SSMI/S-F17) e calcolate le regressioni lineari tra questi per poter inter-calibrare i diversi sensori nei casi di Groenlandia ed Antartide per poter costruire la serie temporale delle mappe di temperatura di brillantezza per tutti i 37 anni disponibili. Viene poi discussa la disponibilità spazio-temporale dei dati, mostrando la necessità di interpolare per ottenere le mappe complete a scala giornaliera.

In seguito, vengono presentati ed implementati cinque diversi algoritmi basati sul principio di superamento di soglia e confrontate la capacità di questi di individuare contenuto liquido nel manto nevoso con dati di temperatura superficiale raccolti tramite stazione meteorologica. Viene poi presentato un confronto tra gli stessi dati alle risoluzioni 3.125 km e 25 km, confrontandoli con i risultati ottenuti da un modello atmosferico regionale (MAR).

Sono stati infine calcolati i principali indicatori utilizzati in letteratura per analizzare le variazioni delle stagioni di fusione avvenute nel corso delle ultime decadi, sia a scala locale (pixel per pixel), sia a livello generale su tutta la superficie glacializzata di Groenlandia e Antartide tramite i più usati parametri sintetici.

In particolare, a scala locale sono stati calcolati la data di inizio della fusione (melt onset date, MOD), di fine della fusione (melt end date, MED) e durata della fusione (melt duration, MD); per quanto riguarda i parametri sintetici sono stati analizzati la durata media di fusione (mean melt duration, MMD), la superficie cumulata di fusione (melting index, MI) e la superficie massima di scioglimento (maximum melting surface, MMS) calcolata come la superficie in fusione per almeno un giorno di Groenlandia ed Antartide. Sono stati calcolati i trend statisticamente significativi al 95% sugli anni disponibili, con maggiore confidenza sui risultati ottenuti per la Groenlandia rispetto all'Antartide, a seguito di un confronto con i risultati

presentati in letterature. Infine, è stato presentato il caso emblematico dell'evento di fusione straordinario avvenuto nel luglio 2012 in cui il 99% della superficie della Groenlandia era in fusione.

In conclusione, tramite questo lavoro di tesi è stata dimostrata la potenzialità e l'applicabilità degli algoritmi utilizzati ai nuovi dati ad alta risoluzione spaziale nell'identificazione di contenuto di acqua liquida sulle calotte di ghiaccio di Groenlandia ed Antartide, è stato creato un dataset (a breve disponibile per download e utilizzo) delle mappe di fusione superficiale caratterizzato da copertura temporale e risoluzione spaziale senza precedenti e sono state studiati gli effetti delle modificazioni climatiche delle ultime decadi ai capi dei due emisferi sui processi di scioglimento superficiale.

Acknowledgements

Voglio ringraziare in primo luogo il professor Roberto Ranzi, mio relatore di tesi e riferimento universitario nell'ultimo anno e mezzo, per avermi dato la possibilità di vivere esperienze che hanno reso unico il periodo di studi del corso di laurea magistrale, quali i mesi trascorsi ad Hanoi e a New York, ed avermi proposto argomenti di studio stimolanti e che hanno soddisfatto la mia costante curiosità.

Un grande ringraziamento va al mio correlatore, il professor Marco Tedesco, per il costante supporto, per aver valorizzato le mie qualità e creduto in me, per esser stato per me mentore ed amico durante mesi trascorsi a New York.

Ringrazio H2CU e l'Università degli Studi di Brescia per il supporto economico fornitomi tramite l'alloggio presso il College Italia e la borsa di studio per tesi all'estero senza i quali la mia esperienza a New York non sarebbe stata possibile.

Ringrazio i miei colleghi, compagni di ufficio e amici della Columbia University, Patrick Alexander e Shujie Wang, per aver reso gioiosa ogni giornata al lavoro.

Grazie a Sandra, Beppe, Andrea ed Alberto, perché sono stati sempre presenti e hanno sempre creduto profondamente in me e mi spingono sempre a dare il meglio. Ringrazio tutti i miei famigliari, in particolare i miei nonni che spero sempre di rendere orgogliosi.

Ringrazio tutti i miei amici, gli anni dell'Università sono stati unici anche, e soprattutto, per merito vostro.

Infine, un sincero grazie a Roberta per pazienza ed insostituibile supporto su cui posso contare ogni giorno.

Brescia, 15 Luglio 2019

Paolo Colosio

Section 1

1 Introduction

“Spring thaw strikes early in Arctic region”, New York Times, June 20th, 2019.

“Groenlandia, il ghiaccio si scioglie. E i cani da slitta corrono sull'acqua”, La Repubblica, June 18th, 2019.

“What to know about the rapid melting of the Greenland ice sheet, a significant contributor to rising sea levels”, ABC News, June 20th, 2019.

The New York Times

Soaring Temperatures Speed Up Spring Thaw on Greenland's Ice Sheet

Figure 1: The New York Times title (June 20th, 2019)

These are only a few of the many articles and titles that filled all the newspaper pages at the end of June (2019), after the record of an extremely early and extent melt event occurred in Greenland on June 12th and the emblematic picture reported in Figure 2 has been shared, traveling all around the world. Even if it has been proven that the famous picture does not represent any climate change or gravity of the problem, since a similar picture has been taken also in 1984 by the scientist Heide Jørgensen (<https://www.ilpost.it/2019/06/26/foto-cani-slitta-acqua-1984/>), this year summer melts started earlier than usual due to a stagnant zone of high-pressure air that brought warm air from the south. This is only the last of other highly significant melt events that affected Greenland and the Arctic in general, a clear evidence and signs of the modifications in climatic conditions, attracting the interest not only of people from the scientific area. In fact, there is a strong effort coming in this regard also from people of the religious sphere. An emblematic example is Pope Francis, who defined in his *Laudato sii* the climate as “a common good, belonging to all and meant for all”, stressing the importance of human activities and lifestyle. But attention does not come from the only Catholic world. Also people from Islam and the Orthodoxes spent some words in this regard, for example in *His All-Holiness Ecumenical Patriarch Bartholomew at the Opening of the Ecological Symposium*: “We must recall that the climate change is

an issue that is closely related to our current model of economic development. An economy that ignores human beings and human needs inevitably leads to an exploitation of the natural environment. Nevertheless, we continue to threaten humanity's existence and deplete nature's resources in the name of short-term profit and benefit. How can we possibly imagine a sustainable development that comes at the expense of the natural environment?". For what concerns international governments, they started taking actions since 1992 with the UN Conference on Environment and Development, then with Kyoto Protocol in 1997 till the last Paris Climate Agreement of 2015. Hence, climate change effects are an everyone's area of interest and a crucial component of nowadays policies and political discussions, being no longer negligible and affecting horizontally every sector of our society.



Figure 2: The viral picture of dogs dragging a sled in meltwater in Greenland (Steffen M. Olsen/Denmark's Meteorologiske Institut, via Associated Press).

Since the last century, variations in the most significant climate variables have been observed on both temporal and spatial scales. Climate change is defined according to IPCC as the modifications attributed directly or indirectly to human activity that alters the composition of the global atmosphere and which is in addition to natural climate variability observed over comparative time periods. Causes in modifications in climatic conditions can be divided in natural and anthropogenic (or human, or man-made) causes. The formers account volcanic eruptions, ocean

currents, Earth orbital changes or variations in Solar activity; the latter comprehend the increment of greenhouse gasses emissions driven by deforestation, coal mining, burning of fossil fuels, industrial processes, agriculture etc. Among the greenhouse gasses, carbon dioxide emissions take the largest percentage of the total, accounting for the 64% of the emissions. The greenhouse gasses increment in the atmosphere (in particular CO₂) have been recorded by NOAA since the middle of the past century (<https://www.esrl.noaa.gov/gmd/ccgg/trends/>). The sun's visible wavelengths of radiation can easily reach the Earth surface passing through the atmosphere and a portion of this energy (48%, almost 163 W/m²) is absorbed by the surface. Some of this energy is then emitted by the earth as infrared radiation which can be absorbed by water vapor, carbon dioxide and methane in the atmosphere creating a second source of radiation emitted back to the Earth surface. If the amount of greenhouse gasses is in their natural concentration, this effect is called natural greenhouse effect and it is the responsible of the average global temperature ranging around 15 °C. On the other hand, if the concentration of greenhouse gasses increases, the amount of energy kept into the atmosphere increases as well, enhancing the greenhouse effect. The greenhouse effect, causing an increment of the average global temperature, is not the only effect coming from increased concentration of carbon dioxide in the atmosphere. In fact, a higher concentration in the atmosphere changes also the balance at air-ocean interface, increasing the CO₂ passing to the ocean. An increment of carbon dioxide into a water body causes an acidification of it and it has been recorded that nowadays the oceans are more acid than 50 years ago. By means of climate models of NASA Goddard Institute for Space Studies (GISS), it has been proven that the increment of global average temperature can be explained only considering both natural and anthropogenic causes. Actually, by looking at the model results, the natural factors did not change significantly in the past century. The main driver has to be accounted by the emission of greenhouse gasses.

Among the large variety of effects of climate change, the water cycle is one of the most crucial aspects. Its response to changes in mean temperature is driven at first by the water vapor climate positive feedback loop, regulated by Clausius-Clapeyron equation of water vapor pressure in the atmosphere. An increment of average temperature allows the atmosphere to hold more water vapor that acts as a greenhouse gas, absorbing energy and providing a further increment in temperature.

Moreover, water cycle is strongly affected by modifications of the cryosphere. In fact, it plays a major role in the adjustment of the global climate system (Barry and Gan, 2011) and many studies suggested that glaciers and polar ice caps are large organic carbon reservoirs. Glaciers,

ice sheets and ice caps are also frozen reservoirs whose runoff is mainly controlled by temperature; the increment in surface temperature would translate in reduction of freshwater stored in these solid reservoirs increasing runoff. Thus, observing and monitoring components of the cryosphere is of crucial importance to understand and make previsions on water resources.

2 Continental ice sheet melting and sea level rise

Ice sheets and glaciers are the largest reserve of freshwater on Earth, accounting for almost the 70% of the total. Their role is crucial in the study of hydrological cycles and water resources management.

In this chapter the different parts of the cryosphere are presented and described, followed by the effects of climate change in polar region. Finally, it is presented the effect of ice sheet melting on sea level rise.

2.1 The cryosphere

The cryosphere is the portion of earth where water is in its solid form, either seasonally or annually (Tedesco, 2015). It is composed by snow cover, glaciers, ice sheets, ice shelves, ice caps, freshwater ice, sea ice, icebergs, permafrost and ground ice. Some of these components are defined by glaciologists as perennial and represent the slowly changing/transforming component (Kargel et al., 2014).



Figure 3: Representation of the cryosphere components of Earth
(<http://maps.grida.no/go/graphic/cryosphere>)

Here we briefly describe the different components of the cryosphere represented in Figure.

1) *Frozen ground (seasonally frozen and permafrost)*

This is the most extensive component of the cryosphere (55 million km² in the Northern Hemisphere), occurring when the mean annual air temperature is lower than -1°C. The top part of the layer is defined as active layer and plays a key role in the hydrological cycle.

2) *Snow*

Snow is the second largest portion of the cryosphere with a maximum extent of 47 million km². Its large coverage and high albedo make snow a major player in reflecting solar radiation back to space and regulate the climate on earth. Moreover, the presence of snow in mountain areas represents a big component of summer runoff, during the melting season.

3) *Sea ice*

Approximately one-ninth of the world's oceans are covered by sea ice and, as snow, is an extremely sensitive indicator of climate change since heat loss through open water is roughly 100 times the value through thick ice. Sea ice is mainly divided into first-year (FY) ice and old ice, divided in second-year (SY) ice and multi-year (MY) ice. The last types are FY ice survived at least at one melting season.

4) *Ice sheet*

Ice sheets are a mass of land ice of continental size thick enough to cover the underlying bedrock topography. If during glacial periods there were more ice sheets, today there are two ice sheets only: Antarctica and Greenland. Ice sheets are a major component of world water resources balance, holding 77% of freshwater (90% for Antarctica and 10% for Greenland).

5) *Ice shelf*

Glaciers flowing to coastal areas create a thick floating slab of freshwater ice. Almost the totality of ice shelves is in Antarctica, being the most readily part contributing to sea level rise.

6) *Glacier*

Mass of ice on land flowing downhill and balanced by ablation zone (net losses areas, negative surface mass balance), accumulation zone (where snow falls, generally higher altitudes) and percolation zone (where meltwater percolate into the snowpack). The equilibrium line altitude is the elevation where the surface mass balance turns from negative to positive.

7) *Ice cap*

Similarly to ice sheets, ice caps are land ice but of a smaller extension with a dome shape and radial flow.

In the following parts of this chapter interaction of the cryosphere and the climate system will be described, focusing on Greenland and Antarctica ice sheets (objective of this work) and looking at their contribution to sea level rise.

2.2 Climate change in polar regions

Modifications in climate conditions have been observed all around the planet. However, the experienced changes are not spatially homogeneous, producing different (and sometimes opposite) effects according to the location. Moreover, according to the fourth IPCC report, the high latitudes are the most likely to be affected by the largest changes. In this part similarities and differences of climatic changes in the two polar regions are presented and discussed.

The two polar regions have been observed to present different changes over the last decades. An important changing component of the polar cryosphere, in opposite directions considering the Arctic and Antarctica, is sea ice. In fact, sea ice is generally strictly seasonal in Antarctica, growing in Antarctic winter and melting in summer. On the other hand, Arctic sea ice comprehend multi-year ice and it used to survive in summer. However, in the last decades, if Antarctic sea ice is growing, Arctic sea ice is performing a significant reduction, shrinking dramatically. One of the main reasons of these modifications is the different conditions in topography and land/sea distribution. While the North Pole is characterized by the presence of the Arctic Ocean, leading to a higher net solar radiation in summer, the presence of Antarctic ice sheet at the South Pole reduces the albedo positive feedback. The ice-albedo feedback is one of the greatest responsible of the polar amplification effect. This process is a positive feedback involving the net incoming solar radiation and its relation with the presence of sea ice. Sea ice has a higher albedo than ocean water, leading to a smaller amount of solar radiation absorbed by the surface. With an increment of average temperature, the presence of sea ice in extent and duration is decreased, leading to a higher exposition to solar radiation of a lower albedo surface. As a consequence, the net energy balance is positive leading to a further increment of temperature and a following further decrement of sea ice presence. This is a positive feedback, one of the most difficult processes to be implemented in circulation models and a key point in the understanding how melting of the parts of the cryosphere and climate change are related. In fact, the albedo feedback can be strongly affected by the duration and the extension of surface melting on the ice

sheet. This because the presence of liquid water in the snowpack makes it undergo metamorphosis that increase the size of snow particles, reducing the albedo of the surface.

As a result, it has been recorded far larger temperature anomalies at the highest latitude of the northern hemisphere with respect to the southern. In addition, the effects on atmospheric circulations of the Antarctic ozone hole increased the westerly winds over the Southern Ocean (Turner and Overland, 2009).

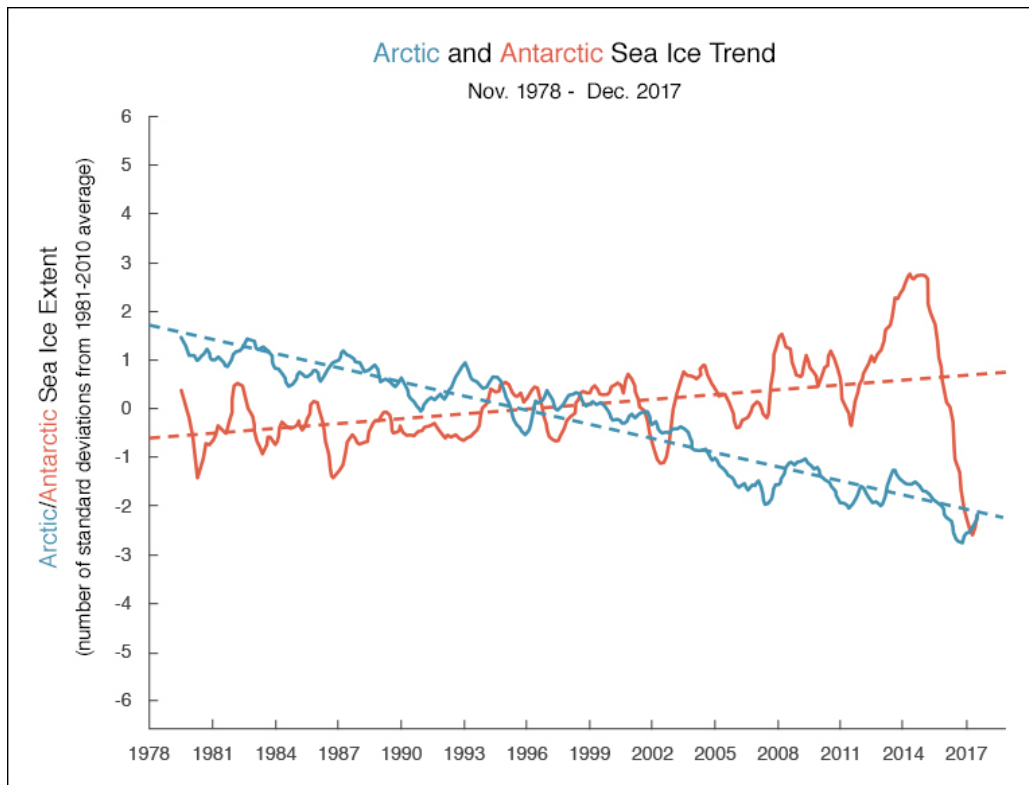


Figure 4: Arctic sea ice extent underwent a strong decline from 1979 to 2012 and Antarctic sea ice underwent a slight increase, although some regions of the Antarctic experienced strong declining trends in sea ice extent. The solid lines indicate 12-month running averages, while the dotted lines indicate the overall trend. Units of extent are shown as standard deviations, which refers to the extent of change from the average. (Source: National Snow and Ice Data Center).

Moreover, Arctic sea ice is a floating platform over the Arctic Ocean, being highly vulnerable not only by the increased occurrence of strong storm events that could break the sea ice but also by the increasing ocean temperature. With reference to sea ice, the Arctic is becoming much like the Antarctic, having more seasonal sea ice. In fact, Stroeve & Notz (2018) found that Arctic sea ice decreased in extent, age and thickness. However, after a long time (almost 3 decades) positive trend, Parkinson (2019), using passive microwave records, found that a

precipitous decline in the last 5 years, reaching the minimum in 2017. Still, considering the last 4 decades, Antarctic sea ice presents a positive overall trend.

Hence, according to satellite measurements and climate models analysis, the behavior of the two Poles is responding oppositely to climate change.

2.3 Greenland and Antarctica ice sheets and sea level rise

Antarctica and Greenland are the only nowadays existing ice sheets, holding the 77% of the total freshwater on Earth and being, respectively, the first and the second largest land ice masses. Greenland ice sheet (GrIS), the largest ice mass of Northern Hemisphere, has a glaciated surface estimated between 1,801,000 km² and 1,824,000 km²; on the other hand, Antarctic ice sheet (AIS) covers approximatively an area of 14,000,000 km².

The thickness of the ice sheets can reach values up to 3 km for Greenland and overcomes 4 km in Antarctica, as shown in Figure showing data from Antarctic Mapping Toolbox (Greene et al., 2016) and bedmachine (Morlighem et al., 2017).

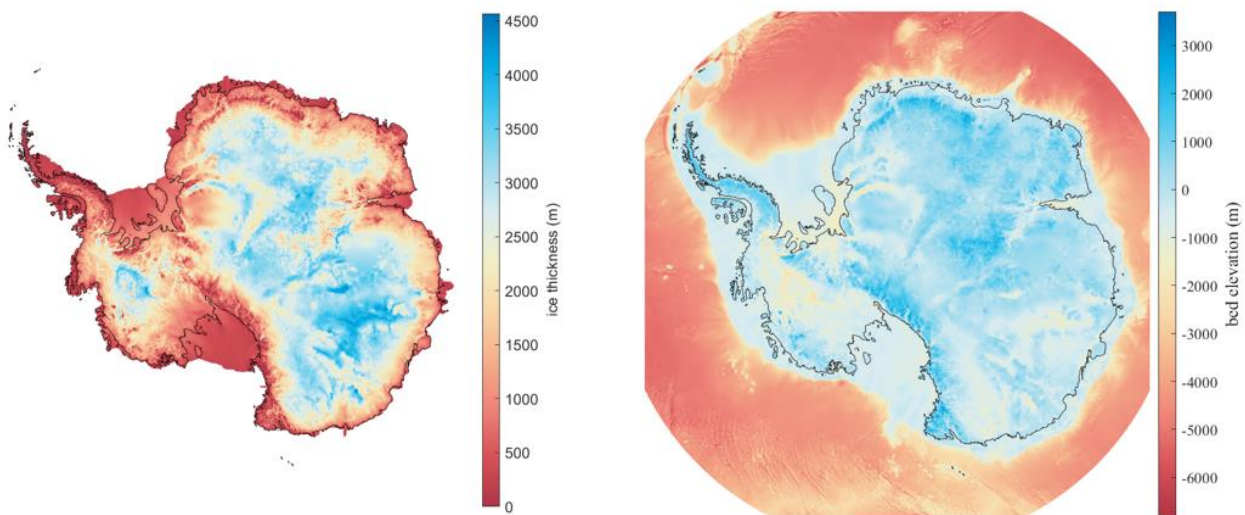


Figure 5: On the left, Antarctic ice thickness (m). On the right, Antarctica bed elevation. To be noticed that West Antarctica bedrock is below sea level. Studies on stability of this part of the continent are crucial for sea level rise estimates.

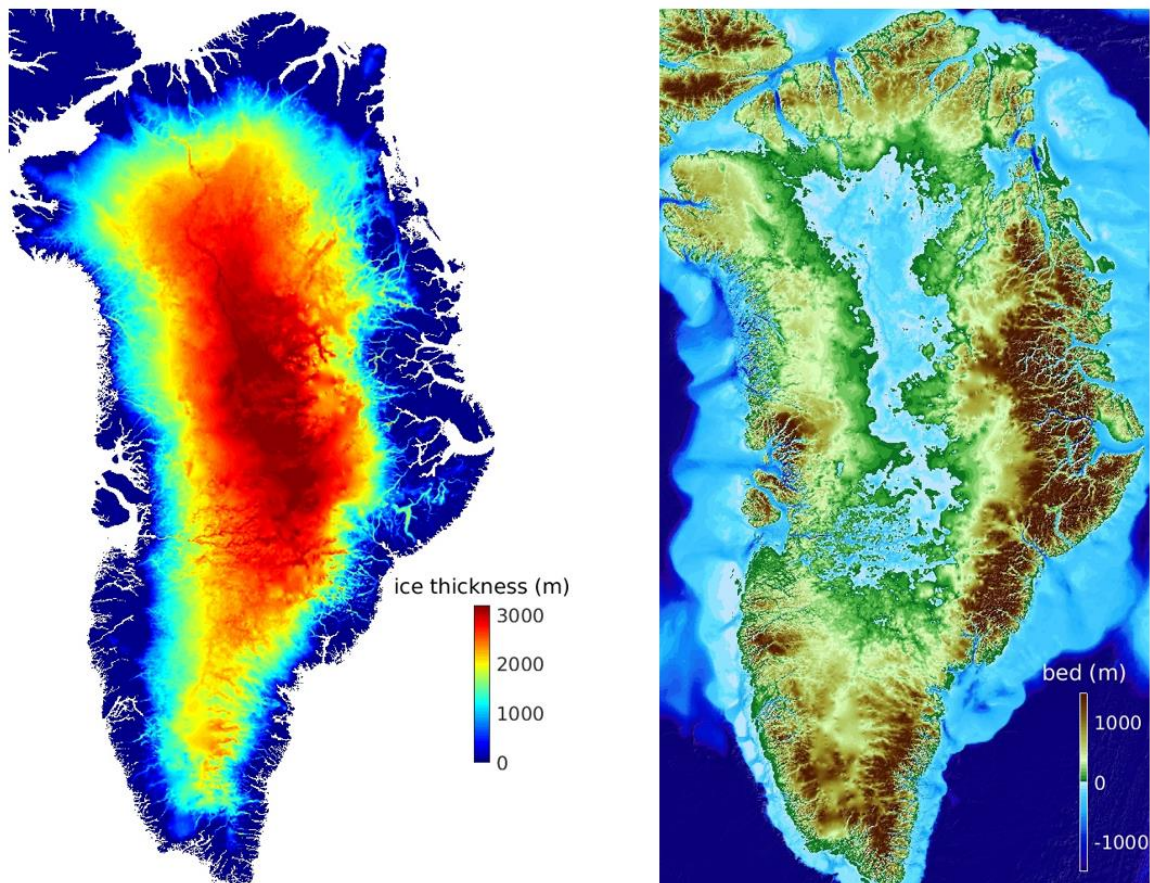


Figure 6: On the left, Greenland ice thickness (m). On the right, Greenland bed elevation.

Due to their large volumes and areas, Greenland and Antarctica Ice sheets take part in the influencing factors of global weather and climate over timescales of days to millennia (Kargel et al., 2014). Measurements of ice mass changes are crucial to better understand rates and variations of processes in climate system and sea level rise. According to GRACE (Gravimetry Recovery and Climate Experiment) data, satellite mission recording changes in Earth's gravitational field, an average of 281 gigatons of ice per year have been lost by Greenland and 125 gigatons per year by Antarctica.

The direct loss of land ice towards the oceans is a direct positive term of the ocean mass balance in the estimation of the sea level rise. According to the IPCC report (2009), the estimated sea level rise for the next century would be, depending on the considered scenario and its uncertainties, ranging between 30 cm and 1 m. Sea level rise is driven by two major components: the thermal and salinity expansion (called thermosteric and halosteric rise, together steric rise) and the ice losses from glaciers and ice sheets (eustatic rise). According to Mengel et al., PNAS, 2016, at current state thermal expansion contribution accounts for the 53% of the average sea level rise, continental glaciers mass loss for 21%, Greenland ice sheet for 21% and Antarctica for

5%. The future projections according to RCP 8.5 IPCC scenario estimates that the thermal expansion contributions will be the 31%, the continental glaciers will account for the 11%, Greenland for the 37% and Antarctica for 21%. Rignot et al. (2011) found that the contribution of both GrIS and AIS to sea level rise is accelerating ($21.9 \pm 1 \text{ Gt/yr}^2$ for Greenland and $14.5 \pm 2 \text{ Gt/yr}^2$ for Antarctica), three times faster than for mountain glaciers and ice caps ($12 \pm 6 \text{ Gt/yr}^2$).

Thus, if nowadays Antarctica ice sheet mass loss plays a minor contribution to sea level rise if compared with thermal expansion and Greenland ice sheet mass loss, in the next centuries (2200-2300), if these trends continue, its role will become dominant and will likely exceed the IPCC report projection (Rignot et al., 2011).

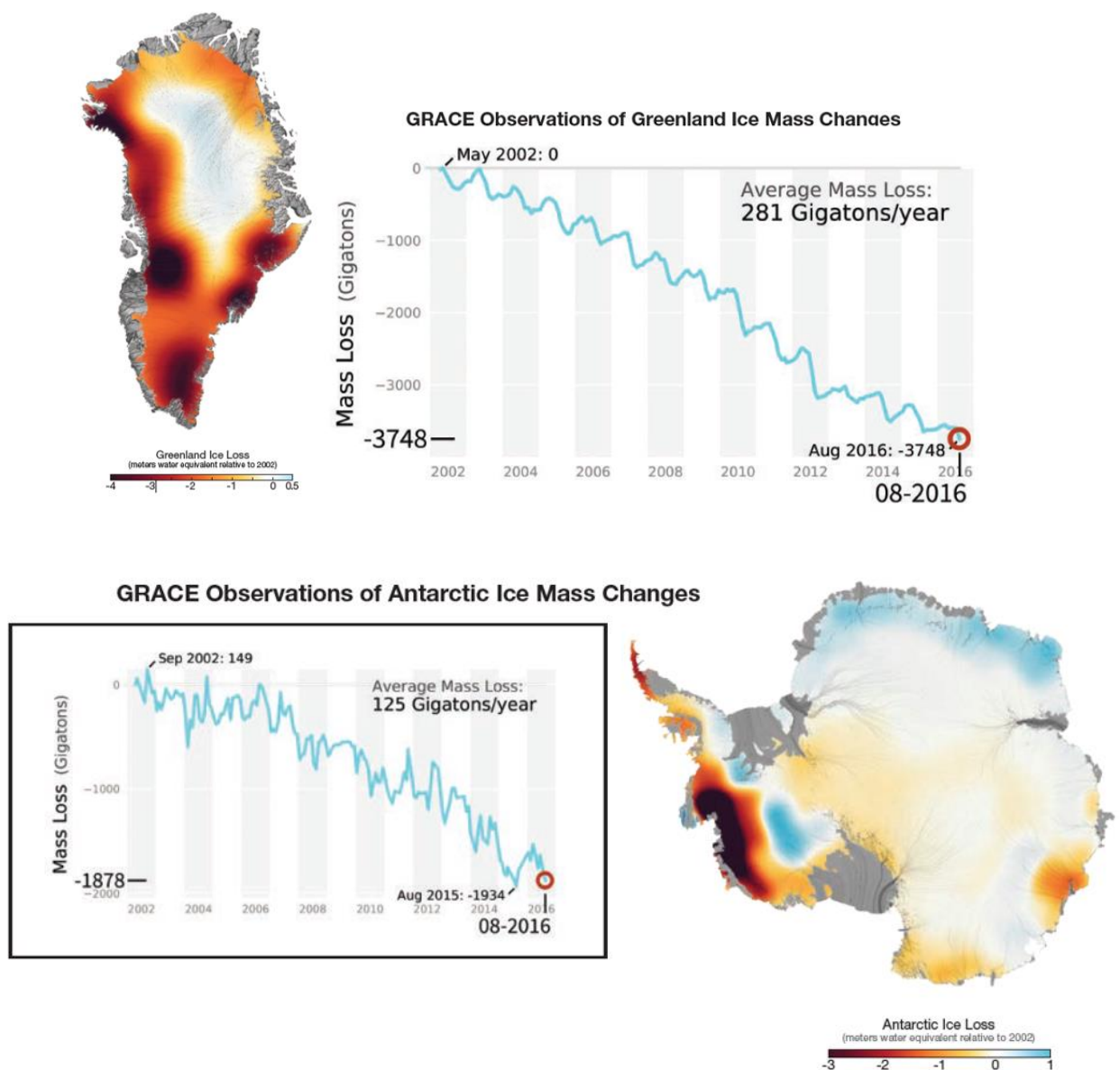


Figure 7: Greenland and Antarctica ice mass loss from GRACE observations. Noticeable are the negative trends (light blue) in some areas of Antarctica, showing the higher stability of the Southern Hemisphere (The Earth Observer, May 2018).

The thermal expansion is not directly dependent on mass addition to the ocean but depends on changes in water temperature changing the density of the water. The other factor affecting seawater density is the salinity, being inversely proportional to the expansion. According to Wadhams and Munk (2004), the equivalent steric sea level is computed as

$$\delta h_{steric} = - \int dz \frac{\delta \rho}{\rho} = \delta h_T + \delta h_S = (0.5 + 0.05) \text{ mm/y}, \quad (1)$$

Where $\delta \rho / \rho = -\alpha \delta T + \beta \delta S$ is the variation of density due to the contributions of temperature changes and salinity changes, parameter.

Consider a global mixed ocean of depth h and density

$$\rho = \rho_{fresh} + \Delta \rho = 1000 + 27 = 1027 \text{ Gt/km}^3, \quad (2)$$

where $\Delta \rho$ is the incremental density associated with salinity. Continental melting adds a layer dh of fresh water (to include melting sea ice we would need to take into account the expansion of the fluid ocean domain into the volume previously occupied by the ice). The salinity of the mixed ocean is then slightly reduced in the ratio

$$\delta \rho / \Delta \rho = -\delta h / h, \quad (3)$$

In terms of the traditional representation by the steric sea level we have

$$\delta h / h = -\delta \rho / \Delta \rho = -(\rho / \Delta \rho)(\delta \rho / \rho) = 36.7 \delta h_s / h. \quad (4)$$

For what concerns the mass loss coming from the ice sheets and the contribution to sea level rise, in order to compute the sea level equivalent (SLE) of the mass loss of Greenland and Antarctica, it is necessary to take into account ice, pure water and sea water densities

	Greenland	Antarctica
Total Mass Loss [Gt]	3748	1878
Ice density [Gt/km³]	0.9167	0.9167
Volume loss [km³]	4088.58	2048.65
Ocean surface [km²]	361800000	361800000
SLE [mm]	11.30	5.66
Record period GRACE [months]	172	172
SLR [mm/month]	0.07	0.03
SLR [mm/year]	0.79	0.40

Table 1: Greenland and Antarctica ice mass loss contribution to sea level rise according to GRACE measurements.

Considering that the oceans cover an area of $3.618 \times 10^8 \text{ km}^2$, according to the estimates previously reported about the trend in mass loss measured by GRACE the sea level rise due to

the loss of mass from Greenland and Antarctica ice sheets is equal to 0.78 mm/year for Greenland and 0.39 mm/year for Antarctica.

In this regard, by accounting the loss of the whole volume of ice of the Greenland and Antarctica ice sheet, it is possible to estimate a SLE, respectively, of ~7 m and ~70 m. By considering the fact that the West Antarctica has a negative bedrock topography that, reasonably, would be occupied by the meltwater, the final estimation of SLE of Antarctic Ice Sheet is closer to 55-60 m. This estimation is the eustatic component of the sea level rise.

Not only eustatic and steric expansion are influencing the changes of sea level around the world. A third component, related to the gravitational field of the Earth, is responsible for the spatial distribution of the sea level changes. In fact, as the ice sheets are losing mass, not only this ice mass is becoming a positive component in the ocean mass balance, but also it is subtracted to the whole ice sheet mass. The ice sheet mass exerts a gravitational (tidal) attraction on the surrounding ocean, which leads to a build-up of water close to the ice mass. Melting of a part of the ice sheet translates to a reduction of the total tidal attraction exerted on the closest mass of ocean. This process leads to an actual decrement of the sea level in the nearest part of the ice sheet, accentuated by the isostatic adjustment process (assumption of elastic deformation of the ground below the ice sheet leading to an uplift after the removal of the weight of the ice), and to a further positive contribution to areas of the ocean far from the ice sheet. This process is schematized in Figure (Gomez et al., 2010).

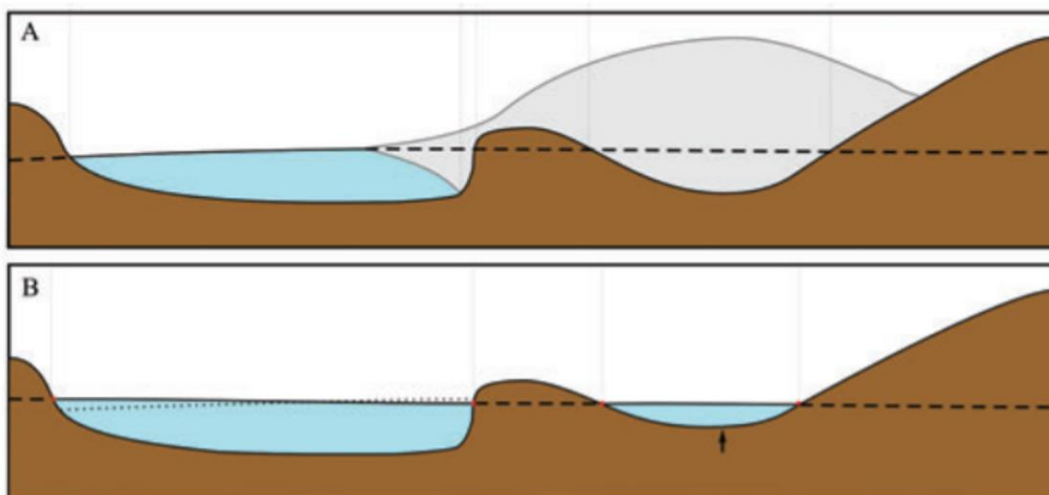


Figure 8: Schematic representation of gravitational effect of ice mass loss to sea level rise (Gomez et al., 2010).

Hence, the predictions of sea level rise contribution of ice sheet melting can take into account more and more details and additional processes, building models from the simplest

(eustatic contribution, a simple mass balance) to more complex models (accounting for shoreline, rotational feedback, Earth elasticity). A detailed description and evaluation of robustness of SLR estimation can be found in Mitrovica et al. (2011). According to this approach, sea level rise prediction to a certain location can be addressed not only to the melting amount and rate but also to the original location of the ice mass lost.

Since ice melting and increased freshwater runoff can dramatically affect European climate (Khromova, 2010), the understanding and monitoring of the processes driving ice melting are crucial to estimate the ice storage and make provisions useful to manage water resources. The GLIMS project (Kargel et al., 2014) works in this regard, monitoring land ice from space and providing an assessment and methodology of the current studies on glaciated areas.

References of section 1

- Barry, R., & Gan, T. Y. (2011). *The global cryosphere: past, present and future*. Cambridge University Press.
- Gomez, N., J.X. Mitrovica, M.E. Tamisiea, and P.U. Clark (2010), A new projection of sea level change in response to collapse of marine sectors of the Antarctic Ice Sheet, *Geophys. J. Int.*, 180, 623–634 doi:10.1111/j.1365-246X.2009.04419.x
- Greene, C. A., Gwyther, D. E., & Blankenship, D. D. (2017). Antarctic Mapping Tools for Matlab. *Computers & Geosciences*, 104, 151–157. Elsevier {BV}. Retrieved from <https://doi.org/10.1016%2Fj.cageo.2016.08.003>
- IPCC First Assessment Report, FAR (1990).
- IPCC Second Assessment Report, SAR (1995).
- IPCC Third Assessment Report, TAR (2001).
- IPCC Fourth Assessment Report, AR4 (2007).
- IPCC Fifth Assessment Report, AR5 (2009).
- Kargel, J. S., Leonard, G. J., Bishop, M. P., Käab, A., & Raup, B. H. (Eds.). (2014). *Global land ice measurements from space*. Springer.
- Khromova, T. E. (2010). Cryosphere and climate. In *IOP Conference Series: Earth and Environmental Science* (Vol. 13, No. 1, p. 012002). IOP Publishing.
- Mitrovica, J. X., N. Gomez, E. Morrow, C. Hay, K. Latychev, and M. E. Tamisiea (2011), On the robustness of predictions of sea level fingerprints, *Geophysical Journal International*, 187(2), 729-742, doi: <http://dx.doi.org/10.1111/j.1365-246X.2011.05090.x>.
- Morlighem, M., Williams, C. N., Rignot, E., An, L., Arndt, J. E., Bamber, J. L., Catania, G., et al. (2017). {BedMachine} v3: Complete Bed Topography and Ocean Bathymetry Mapping of Greenland From Multibeam Echo Sounding Combined With Mass Conservation. *Geophysical Research Letters*, 44(21), 11,051–11,061. American Geophysical Union ({AGU}). Retrieved from <https://doi.org/10.1002%2F2017gl074954>
- Mouginot, J., Rignot, E., Bjørk, A. A., van den Broeke, M., Millan, R., Morlighem, M., ... & Wood, M. (2019). Forty-six years of Greenland Ice Sheet mass balance from 1972 to 2018. *Proceedings of the National Academy of Sciences*, 116(19), 9239-9244.

Parkinson, C. L. (2019). A 40-y record reveals gradual Antarctic sea ice increases followed by decreases at rates far exceeding the rates seen in the Arctic. *Proceedings of the National Academy of Sciences*, 201906556.

Ranzi, R., Grossi, G., Gitti, A., & Taschner, S. (2010). Energy and mass balance of the mandrone glacier (Adamello, Central Alps). *Geografia Fisica e Dinamica Quaternaria*, 33(1), 45-60.

Rignot, E., Velicogna, M. R. van den Broeke, A. Monaghan, and J. Lenaerts (2011), Acceleration of the contribution of the Greenland and Antarctic ice sheets to sea level rise, *Geophys. Res. Lett.*, 38, L05503, doi:10.1029/2011GL046583.

The Earth Observer. May - June 2018. Volume 30, Issue 3.

Turner, J., & Overland, J. (2009). Contrasting climate change in the two polar regions. *Polar Research*, 28(2), 146-164.

Wadhams, P., & Munk, W. (2004). Ocean freshening, sea level rising, sea ice melting. *Geophysical Research Letters*, 31(11).

Xiao, C. D., Wang, S. J., & Qin, D. H. (2015). A preliminary study of cryosphere service function and value evaluation. *Advances in Climate Change Research*, 6(3-4), 181-187.

Section 2

3 Remote sensing of the cryosphere

Remote sensing is the ensemble of techniques that allows the collection of information about an object or a phenomena without physical contact with the object (*Tedesco, 2015*). The collection of information is performed by sensing and recording reflected or emitted energy from the earth surface. Sensors can be airborne, spaceborne or *in situ* and are based on the record of the electromagnetic radiation emitted by the earth surface. Sensors differentiate by the band of the electromagnetic spectrum they can detect and from different sensors, by means of different techniques, it is possible to have qualitative and quantitative information about the earth surface in space and time.

In this chapter fundamentals of electromagnetic radiation are presented, focusing on electromagnetic properties of snow and ice, in particular in microwave region. Then a summary of active and passive remote sensing instruments characteristics and finally passive microwave snowmelt detection techniques will be discussed.

3.1 Electromagnetic radiation of a blackbody and brightness temperature

Remote sensing is based on the record of the energy emitted or reflected by the earth surface in the form of electromagnetic radiation, mathematically described through the wave propagation theory of classical electrodynamics. Starting from source-free (total charge $Q=0$ and current density $\underline{I}=0$) Maxwell's system of first order differential equations it is possible to derive wave propagation equations.

$$\text{Gauss law for electric field} \quad \nabla \cdot \underline{E} = 0, \quad (5)$$

$$\text{Gauss law for magnetic field} \quad \nabla \cdot \underline{B} = 0, \quad (6)$$

$$\text{Faraday's law} \quad \nabla \times \underline{E} = -\frac{\partial \underline{B}}{\partial t}, \quad (7)$$

$$\text{Ampere's law} \quad \nabla \times \underline{B} = \mu\epsilon \frac{\partial \underline{E}}{\partial t}, \quad (8)$$

By applying the curl to the Faraday's law and recalling Ampere's law and Gauss law for electric field, it is possible to obtain

$$\nabla^2 \underline{\mathbf{E}} = \mu\epsilon \frac{\partial^2 \underline{\mathbf{E}}}{\partial t^2}, \quad (9)$$

which relates spatial and temporal second order derivative of the electric field and is called wave equation. Similarly, it is possible to obtain the wave equation for the magnetic field.

$$\nabla^2 \underline{\mathbf{B}} = \mu\epsilon \frac{\partial^2 \underline{\mathbf{B}}}{\partial t^2}, \quad (10)$$

It is possible to prove that by considering an electromagnetic wave propagating in \underline{e}_3 direction the electric field can have components only in \underline{e}_1 and \underline{e}_2 directions, perpendicular to \underline{e}_3 . In the same way, magnetic field can have components such that $\underline{\mathbf{E}}$, $\underline{\mathbf{B}}$ and \underline{e}_3 are perpendicular each other. Thus, according to wave theory, both electric and magnetic fields propagate orthogonally to wave propagation direction with the same velocity c , related also to two other fundamental properties of waves: wavelength λ and frequency ν , and $\mu\epsilon = c^{-2}$.

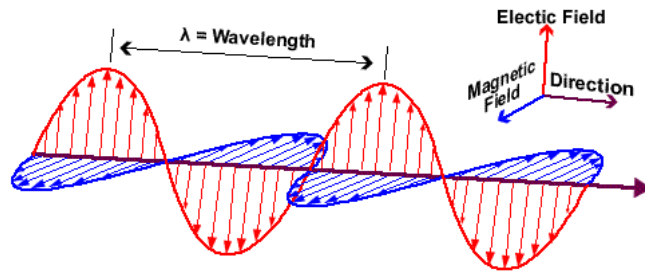


Figure 9: Schematic representation of electromagnetic wave.

$$c = \lambda\nu, \quad (11)$$

It is called polarization the direction of the electric field with respect to the earth surface: if the electric field is parallel to the earth surface the polarization is horizontal, if it is perpendicular to the earth surface the polarization is vertical.

It can be noticed that the propagation of the electromagnetic radiation is related to two different physical properties of the media: permeability and permittivity. The electromagnetic permittivity ϵ is represented by a real and an imaginary part

$$\epsilon = Re(\epsilon) + Im(\epsilon)i, \quad (12)$$

where the real part represents the scattering while the imaginary one the absorption.

Electromagnetic radiation is emitted by any object having absolute temperature higher than 0 K. The power radiated by a blackbody is related to the thermodynamic temperature through the Stefan-Boltzmann's law, considering all the wavelengths, while the spectral density of the radiation is described by Planck's law, either in wavelength and frequency forms. The peak emission of the blackbody at a given temperature is related to the wavelength (or frequency) through Wien displacement law. Planck law, in frequency formulation, can be expressed as

$$B(\nu, T) = \frac{8\pi\nu^2}{c^3} \frac{h\nu}{e^{\frac{h\nu}{k_b T}} - 1}, \quad (13)$$

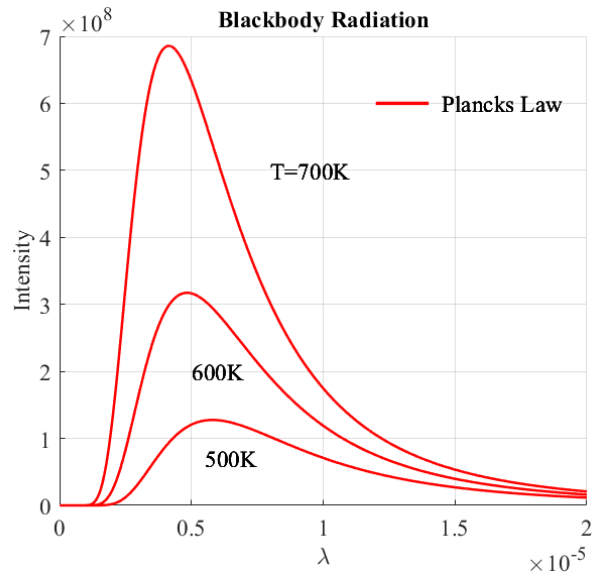


Figure 10: Intensity of blackbody radiation in function of the wavelength according to Plank's law at different temperatures. The higher the temperature the higher the emitted radiation. The peak is shifted to lower wavelengths as the temperature increases.

In microwave region (long wavelength, low frequency, [300MHz,300GHz]) the term $h\nu \ll k_b T$ make possible to expand the term at the denominator according to the Taylor expansion

$$e^x = 1 + \frac{x}{1!} + \frac{x^2}{2!} + \frac{x^3}{3!} + \dots, \quad (14)$$

Leading to the expression

$$B(\nu, T) = k_b T \frac{8\pi\nu^2}{c^3},$$

Representing the radiation of a blackbody at low frequency: the Rayleigh-Jeans approximation. The brightness temperature is defined as the temperature of a blackbody having the same brightness of the considered surface. The brightness temperature is dependent only by the physical temperature of the emitting surface and by the electromagnetic permittivity which are frequency and polarization dependent; only in the case of blackbody the brightness temperature

is the same for all frequencies. The expression of the brightness temperature according to the Rayleigh-Jeans approximation is

$$T_b = \varepsilon T, \quad (15)$$

In the following parts of this chapter we discuss the permittivity characteristics of the parts of the cryosphere of our interest for the purposes of this work.

3.2 Electromagnetic properties of snow and ice in microwave region

Microwave emission properties of glaciers and ice sheets are substantially dependent on ice and snow properties. During the winter season the emission is driven either by the interaction of snow and ice layer (low frequencies) or mostly by the snow cover (higher frequencies). On the other end the summer season is characterized by wet snow covering the glacier or melting ice. In both cases, the presence of liquid water leads to a significant increment of the imaginary part of permittivity.

3.2.1 Ice

Pure ice dielectric permittivity, in microwave region, does not depend on frequency and weak depend on temperature for the real part while depends on both of them for the imaginary part. The weak dependence on temperature is the basis of the relations proposed to model the real part of the dielectric constant (here the example of Matzler and Wegmuller, 1987):

$$Re(\varepsilon_{ice}) = 3.1884 + 9.1 \cdot 10^{-4}(T - 273), \quad (16)$$

The imaginary part presents in microwave region dependency on temperature and frequency as

$$Im(\varepsilon_{ice}) = \frac{A(T)}{f} + B(T)f, \quad (17)$$

where f is the frequency and A and B are coefficients dependent on temperature and relation have been proposed based on data fitting (here for example Stogryn, 1986)

$$A(T) = \frac{e^{[12.5 - \frac{3.77 \cdot 10^3}{T}]}}{T}, \quad (18)$$

$$B(T) = 10^{-4} Re(\epsilon_{ice}) \cdot (273.41 - T)^{-0.5}, \quad (19)$$

These relations from literature are referred to pure ice. In reality, in ice impurities are generally present and play a significant role in the changes of the permittivity. As impurities can have different origins: debris coming from the bed of the glacier, dust, carbon or presence of ice algae (Wang et al., 2018).

3.2.2 Snow

Snow is considered as a complex medium, consisting in different parts. A layer of snow can be classified as dry or wet. Dry snow is a medium composed by ice crystals in an air background while wet snow is a mixture of ice particles, water droplets and air. The scattering properties of the layer are dominated by the ice particles (Ulaby et al., 1986).

According to the emission characteristics, different types of snow have been classified according to the following scheme (Schanda et al, 1983):

- 1) *Winter snow*: dry snow that has not undergone melting metamorphism, generally found at high altitude areas in winter period (November-March for Northern Hemisphere, March-November for Southern Hemisphere);
- 2) *Wet spring snow*: snowpack composed by a thick layer of wet, quasi-spherical ice crystals formed day-time at T above freezing point;
- 3) *Dry spring snow*: snowpack consisting of a layer of refrozen snow formed during cold nights.

The following figure (from Ulaby et al. 1986, from the study of Schenda et al. 1983) shows the spectra in microwave region of the mentioned typologies of snow. At 37 GHz, it is possible to notice that the difference between winter dry snow and refrozen spring snow is around 30 K.

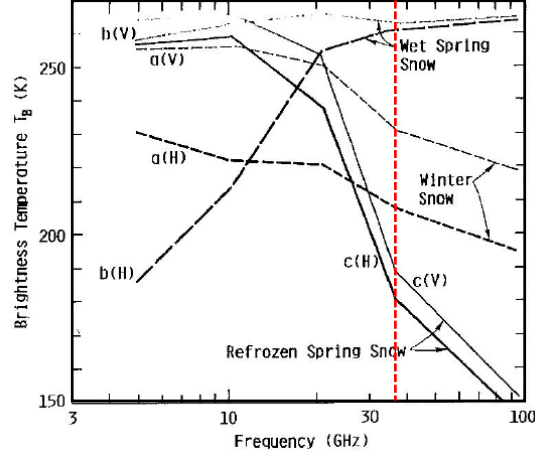


Figure 11: Emission behavior of wet spring snow, winter snow and refrozen spring snow at different frequencies in microwave region.

The microstructure of snow with presence of liquid water can be divided in pendular and funicular regime. The former, characterized by low wetness, presents water bubbles divided by a continuous air background through the ice crystals; the latter, characterized by high wetness, presents a continuous liquid phase.

Hence, dry and wet snow electromagnetic properties are fundamental to understand the emission behavior of the surface sensed by passive microwave sensors. As previously said, dry snow from an electromagnetic point of view is a medium composed by ice and air. The electromagnetic permittivity is thus a function of the physical properties of the components of the snowpack. The real part is considered constant with respect to frequency and temperature and function of fractional volume only. Empirical relationships have been proposed in literature to define both real and imaginary part as function of snow density (Mätzler,1987; Sihvola, 1999) as:

$$Re(\epsilon_{drysnow}) = a + b\rho_{drysnow}, \quad (20)$$

$$Re(\epsilon_{drysnow}) = \frac{1+\alpha\rho_{drysnow}}{1-\beta\rho_{drysnow}}, \quad (21)$$

$$Im(\epsilon_{drysnow}) = Im(\epsilon_{ice}) \cdot F(\rho_{drysnow}), \quad (22)$$

For what concerns wet snow, it can be seen as a medium composed by ice, air and liquid water: dry snow with the appearance of liquid water content. The general expression for wet snow permittivity is

$$\epsilon_{wetsnow} = \epsilon_{drysnow} + \Delta\epsilon, \quad (23)$$

where $\Delta\epsilon$ is generally expressed as polynomial function of the wetness. Generally speaking, the presence of liquid water has a major effect on the imaginary part of the electromagnetic permittivity, the absorption term leading to an increment of the emission.

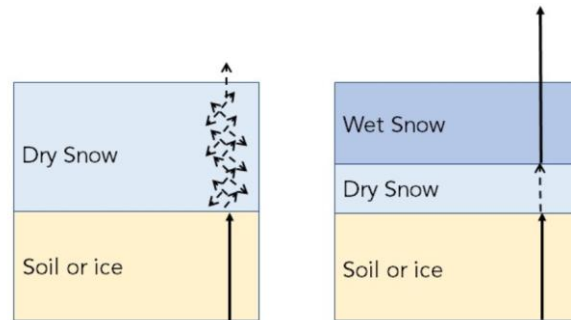


Figure 12: Schematic representation of emission behavior of snow in dry and wet conditions.

3.3 Passive microwave remote sensing of melting snow and ice

3.3.1 Background and rationale

Since microwave sensors can detect directly the change in electromagnetic properties of snow passing from dry to wet conditions, many remote sensing techniques have been developed and applied to detect melt events. Unlike other sensors, passive microwave (PMW) sensors are not sensitive to weather conditions and clouds. Moreover, since the PMW sensors measure the energy naturally emitted by the surface they do not require solar illumination. These two characteristics allow to detect and map melting at high temporal resolution. The first satellite with the Scanning Microwave Multichannel Radiometer (SMMR) has been launched in 1979, it has been followed by the Special Sensor Microwave/Imager (SSM/I, from 1987) and the Special Sensor Microwave Imager/Sounder (SSM/I-S, from 2006) flying on Defense Meteorological Program Satellites (DMSP) and the Advanced Microwave Scanning Radiometer- EOS (ASMR-E) flying on the NASA AQUA satellite (2002- to date). Thus, PMW data are also characterized by a temporal coverage longer than 30 years. A long time series of data is necessary to evaluate changes in hydrological and climate systems, hence PMW represent an irreplaceable tool.

Spaceborne PMW sensors can measure the radiation emitted at different frequency of the microwave part of the electromagnetic spectrum. (mostly K and Ka bands). Different frequencies

are characterized by different penetration length which means that every channel is representative of a certain depth at which the energy is emitted. This characteristic allows to detect sub-surface melting even when surface snow is frozen because of near-surface temperature is below zero but below the frozen layer snow is experiencing melting because of radiative forcing.

Spatially, PMW sensors can cover a larger area if compared with optical/thermal system due to a larger Ground Instantaneous Field of View (GIFOV) on the order of tens of kilometers. The large swath combined with the multiple passages of the satellites above the polar regions make PMW sensors extremely suitable for large scale studies. The large spatial and temporal coverage and the high temporal resolution were counterbalanced by a slightly low spatial resolution.

Passive microwave data have been widely adopted in melt detection studies [Macelloni et al. (2005), Pampaloni et al. (2004)] and different remote sensing techniques have been proposed. These techniques to detect snowmelt events by means of PMW data are based on the detection of the sudden increase of the signal of brightness temperature coming from the presence of liquid water in the snowpack. Brightness temperature is the measurement of the emission of the earth surface in microwave spectrum. In these bands, since the frequency of the electromagnetic radiation is small enough, Plank law can be approximated with Rayleigh-Jeans law (Equation 24) that linearly relates the electromagnetic emission (T_b) to the physical temperature of the surface (T) through a scalar parameter called emissivity (ϵ), inversely proportional to the electromagnetic permittivity.

$$T_b = \epsilon T, \quad (24)$$

Thus, the variability of brightness temperature is governed by the physical temperature and the electromagnetic properties of the media. Considering that in polar region it is unlikely to have very high gradients of temperature at daily timescale and that during melting events snow temperature ranges around 273.15 K, the sudden increase of brightness temperature is related to the sudden increase of emissivity. In fact, the presence of liquid water in the snow pack, contributing to the imaginary part of the electromagnetic permittivity (absorption), produces an increment in emissivity of several orders of magnitude with respect to the dry snow condition, dominated by the real part of the permittivity (scattering), according to frequency and polarization (Ulaby et al., 1986). Hence, by looking at the abrupt increment in T_b time series, it is possible to detect liquid water content in the snowpack (Macelloni et al., 2001), distinguishing between dry and wet pixels (Fig. 13) and consequently map melting areas.

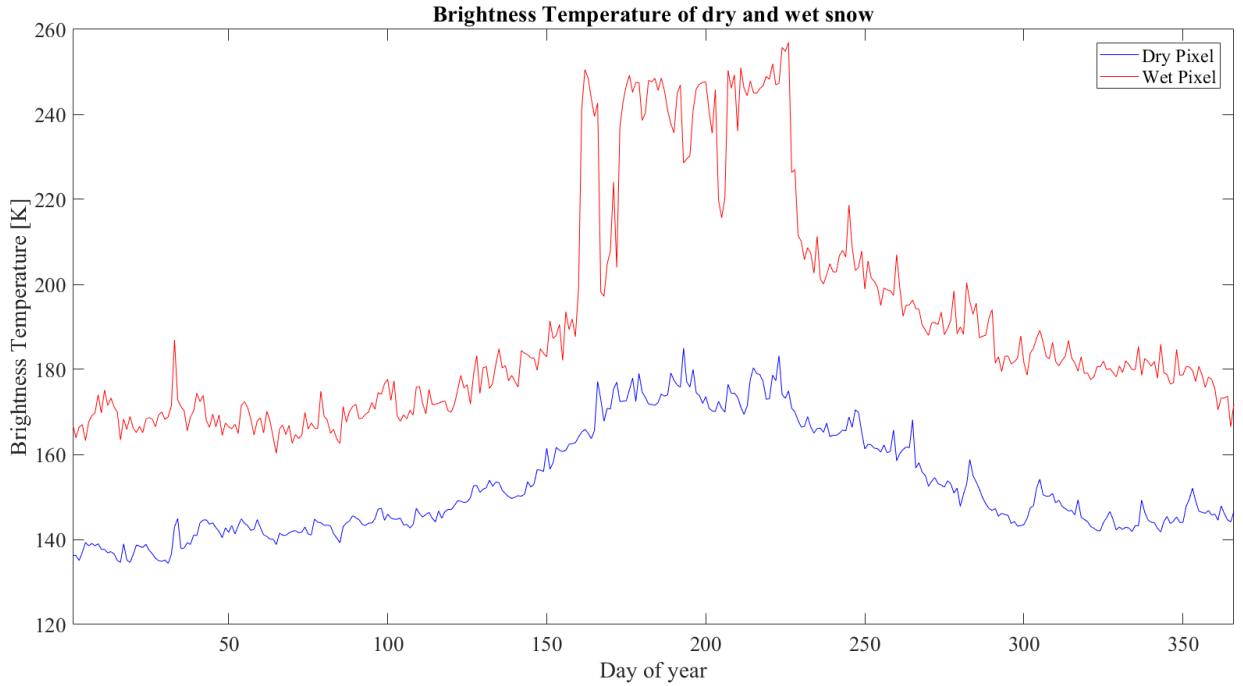


Figure 13: Brightness temperature of dry and wet pixels over Greenland ice sheet sensed by 37 GHz passive microwave radiometer, horizontal polarization.

3.3.2 Melt detection algorithms in literature

According to the emission properties described, several snowmelt detection algorithms have been developed and proposed in literature. A first classification can be done distinguishing in threshold-based (T-B) and edge-detection (E-D) algorithms. Another distinction can be done between single-channel (S-C) and multi-channel approaches (M-C). Threshold based algorithms detect melting days when a defined threshold is exceeded while edge-detection algorithms look for the sudden change of the T_b signal. For what concerns T-B algorithms, Steffen et al. (1993) used the normalized gradient ratio $GR = (T_{b19H} - T_{b37H}) / (T_{b37H} + T_{b19H})$ to detect wet pixels fixing a threshold based on in situ measurements. This method has been improved by Abdalati and Steffen (1995) introducing the cross-polarized gradient ratio $XPGR = (T_{b19H} - T_{b37V}) / (T_{b37H} + T_{b19V})$, changing the Ka-band component of the algorithm from horizontally to vertically polarized. These techniques both use a M-C approach. Other methods based on S-C approach have been proposed, using fixed and space-time variable thresholds. A fixed threshold equal to 245 K, derived from the outputs of electromagnetic model and defined as the threshold above which there is no significant increment in T_b after a further increase in LWC (Tedesco et al., 2007). Aschraft and Long (2006) proposed a threshold based on dry (winter) and wet snow T_b as $T_c = \alpha T_{winter} + (1 - \alpha) T_{wet}$ where T_{winter}

is the average of winter temperature and T_{wet} fixed as 273 K. The mixing coefficient $\alpha=0.47$ was derived considering LWC=1% in the first 4.7 cm of snowpack. Other studies have been done using a threshold value based again on the winter mean temperature plus an increment coming from the presence of LWC.

$$T_c = T_{winter} + \Delta T, \quad (25)$$

Torinesi et al. (2003) proposed a value of $\Delta T=N\sigma$ with T_{winter} and σ that vary in space and time but fixed $N=3$ derived by comparison with weather station temperature data. Similarly, Zwally and Fiegles (1994) used $\Delta T=30$ K. In this work we tried to increase this value in order to perform a sensitivity analysis to 35 K and 40 K. Tedesco (2009) proposed another approach based on Microwave Emission Model of Layered Snowpack (MEMLS) outputs. The model simulated, varying the input parameters (as density and temperature) and fixing others (frequency, polarization and LWC), the brightness temperature at two different values of LWC considering a surface layer of 0.05 m. From MEMLS the increment above the winter mean is also linearly dependent to the winter mean as follows

$$\Delta T = \varphi T_{winter} + \omega, \quad (26)$$

Values of the coefficients (φ , ω) have been computed as (-0.2, 58 K) in case of LWC=0.1% and (-0.52, 128 K) in case of LWC=0.2%. Inserting this expression of the ΔT into Eq. (25), T_c can be written as

$$T_c = T_{winter} + \varphi T_{winter} + \omega = (1 + \varphi)T_{winter} + \omega = \gamma T_{winter} + \omega, \quad (27)$$

where (γ , ω) assume the values (0.8, 58 K) in case of LWC=0.1% and (0.48, 128 K) in case of LWC=0.2%. According to the results showed by Tedesco (2009), in this work we apply and study on the enhanced resolution dataset the coefficients related to the presence of LWC=0.2% only.

Differently, a technique based on the diurnal amplitude variation (DAV) have been proposed by Ramage and Isacks (2002) to detect melt in Alaska considering a fixed threshold value on both 37 GHz brightness temperature (246 K) and DAV ($DAV_c=10$ K). Tedesco (2007) improved this technique considering not only the Ka-band channel but also the 19 GHz brightness temperature to detect melting on Greenland ice sheet, passing from a S-C to a M-C technique. A further improvement of this technique has been proposed by Tedesco et al. (2009) with the D-DAV approach. If in the previous studies the thresholds T_c and DAV_c were spatially fixed, in D-DAV the threshold DAV_c is computed as $DAV_{jan,feb} + 10$ K while T_c comes from the modelling of a bimodal PDF as $B(m_1, s_1, m_2, s_2, p) = pG(m_1, s_1) + (1-p)G(m_2, s_2)$ where p is the percentage of dry pixels and m_i and s_i are respectively the mean and the standard deviation of the two parts of the

curve. The threshold is expected to be between the two means. With this method both thresholds are dynamically computed in space.

On the other hand, E-D approaches are based on signal processing techniques with the aim of detecting the sudden change of the PMW record signals. Liu et al. (2005) proposed the use of the wavelet transform evaluating the optimal edge threshold value by minimizing the probability of erroneous pixel classification from the parameters of a bimodal distribution. This method has been improved by applying a neighborhood operation, correcting possible errors in detecting melt onset date by looking at the closest pixels. Joshi et al. (2001) adopted a filter based on the derivative of Gaussian to analyze trends of melt duration over Greenland. Steiner and Tedesco (2014) adopted a wavelet-based algorithm applied to scatterometer data to detect melt over Antarctica.

4 Enhanced resolution passive microwave data

4.1 Data characteristics

We use spaceborne passive microwave enhanced resolution horizontally polarized brightness temperatures generated within the framework of a NASA MeASUREs project [<https://earthdata.nasa.gov/community/community-data-system-programs/measures-projects>] and distributed by NSIDC in the Equal-Area Scalable Earth Grid (EASE 2.0) projection at a spatial resolution ranging from 25 km to 3.125 km, depending on the frequency. In this work we use data over both the Northern and Southern Hemispheres to study the potential of this dataset to be applied over both the Greenland and Antarctica ice sheets for melt detection and mapping. Specifically, we use the Ka band (37 GHz), horizontal polarization in view of its sensitivity to the presence of liquid water within the snowpack (Ulaby et al., 1986) and because of the relatively high spatial resolution (3.125 km) at which this dataset is produced. The dataset produced by Brodzik et al. (2018) consists in both low resolution, characterized by low noise, and high resolution data, supposed to be more noise affected, and is produced with two different swath-to-grid algorithms. The coarse resolution dataset is based on a drop in a box algorithm that averages every swath measure falling in the considered pixel and is the same algorithm used to produce precedent gridded data. The enhanced resolution dataset is the result of a radiometer version of Scatterometer Image Reconstruction (rSIR) technique that transforms swath data to gridded format that derives the T_b value from all the overlapping measurements, weighted by antenna gain. The approach used to generate the enhanced resolution product addresses also another issue in the historical PMW dataset, consisting in the need for meeting the requirements of modern Earth system Data Records or Climate Data Records (CDRs), most notably in the areas of inter-sensor calibration and consistent processing methods. Overall, the historical gridding techniques for these passive microwave sensors (Armstrong et al., 1994, updated yearly; Knowles et al., 2000; Knowles et al., 2006) were relatively primitive and were produced on grids (Brodzik and Knowles, 2002; Brodzik et al., 2012) that are not easily accommodated in modern software

packages. In the reconstruction algorithm used for the enhanced Tbs, the so-called effective measurement response function (MRF), determined by the antenna gain pattern and being unique for each sensor and sensor channel, is used in conjunction with the scan geometry and the integration period. The technique uses the Backus-Gilbert technique (Backus and Gilbert, 1967; 1968), a general method for inverting integral equations, which has been applied for solving sampled signal reconstruction problems (Caccin et al., 1992; Stogryn, 1978, Poe, 1990), for spatially interpolating and smoothing data to match the resolution between different channels (Robinson and Olson, 1992), and improving the spatial resolution of surface brightness temperature fields (Farrar and Smith, 1992; Long and Daum, 1998). More information about the product can be found at <https://nsidc.org/data/nsidc-0630>.

Our time series starts in 1980, with data available from the SMMR sensor and ends in 2016 for a total of 37 years. Data is provided twice a day, as morning and evening passes and the melt detection algorithms are applied to both datasets in order to capture melting that could be present in either or both passes. For our analysis, we use data collected by the SMMR-Nimbus 7, SSM/I-F08, SSMI-F11, SSM/I-F13, SSMI/S-F17 because of the higher stability over the working period [<http://www.remss.com/support/crossing-times/>]. Two main problems in building a multisensor time series are the differences associated with the use of different sensors and associated degrading of performance as well as the difference in the availability of data from multiple datasets. In order, to address these issues we cross-calibrate the different sensors using concurrent acquisitions and interpolate the obtained brightness temperatures to obtain a continuous time series between 1980 and 2017 over both hemispheres (see Chapter 4).

An example of enhanced PMW data collected over Greenland on July, 2008 is reported in Figures 14 and 16, showing the enhanced spatial detail that the new product can capture with respect to the one previously used at 25 km. As can be noticed from map, the spatial distribution of Tb at large scale can be well captured by both coarse and enhanced resolution products. A considerable improvement in defining spatial patterns can be noticed by looking closer to the selected validation site. The enhanced resolution not only shows more precisely the spatial variability of brightness temperature, but also provides a better representation of the ice sheet edges, reducing the problem of mixed ice-land-ocean pixels. In Figure 15 is reported an example of the timeseries at Swiss Camp at coarse and enhanced resolution and reporting two of the threshold values studied in this paper. It can be noticed that the two timeseries appears to be similar and sensitive to the presence of liquid water. However, in some days melt is not detected

in both timeseries, showing the different spatial sensitivity of the enhanced resolution gridded data we assume to represent better melting events in each location.

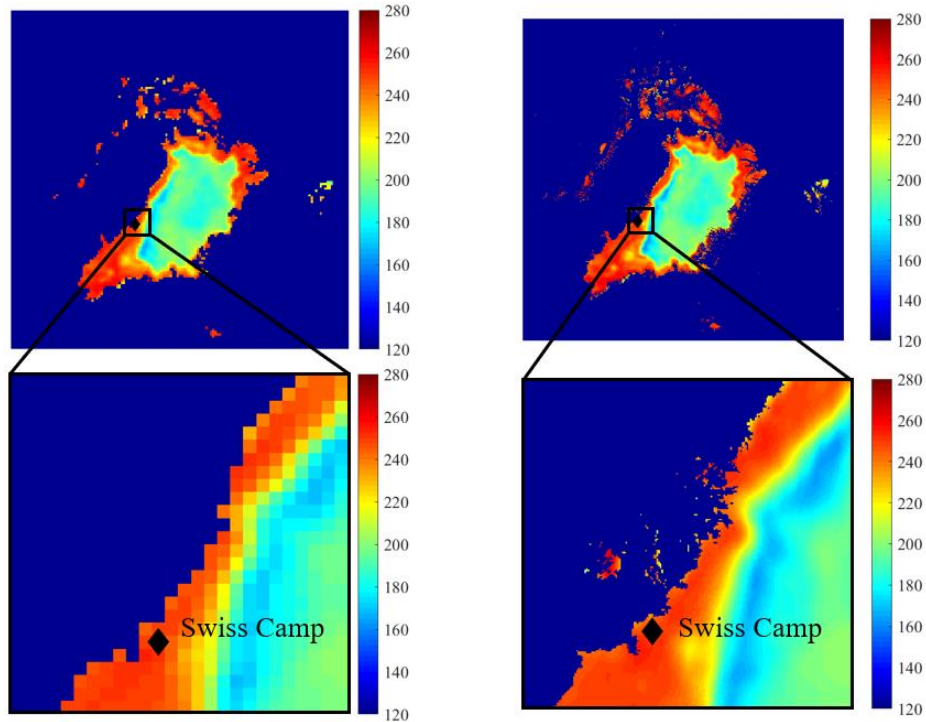


Figure 14: Passive microwave brightness temperature image over Greenland ice sheet at 25km and 3.125km spatial resolution. Below a detail of the area surrounding Swiss Camp.

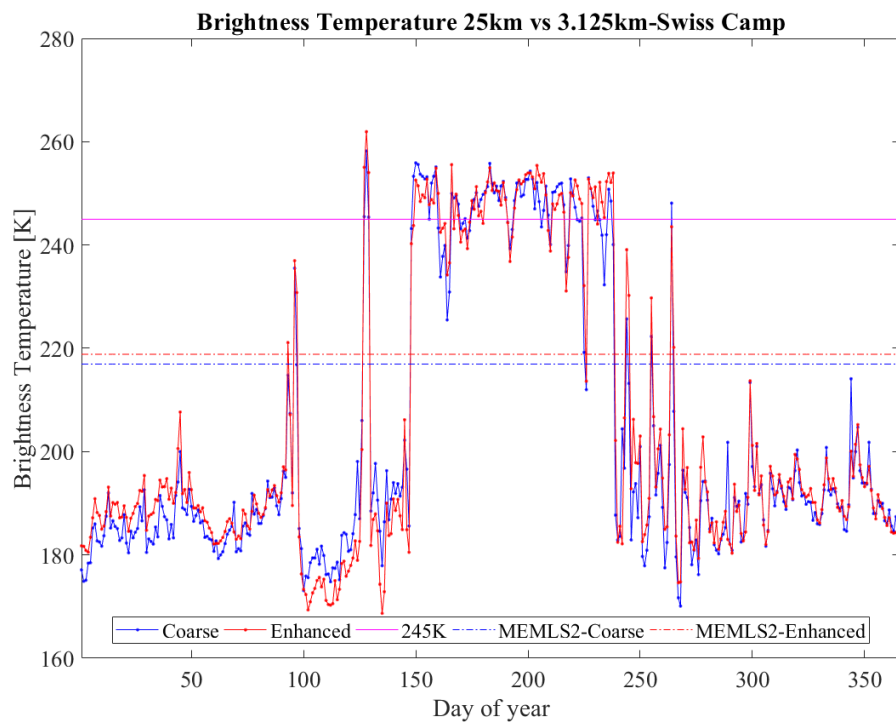


Figure 15: Time series of brightness temperature (37 GHz, horizontal polarization) over Greenland ice sheet at 25km and 3.125km spatial resolution.

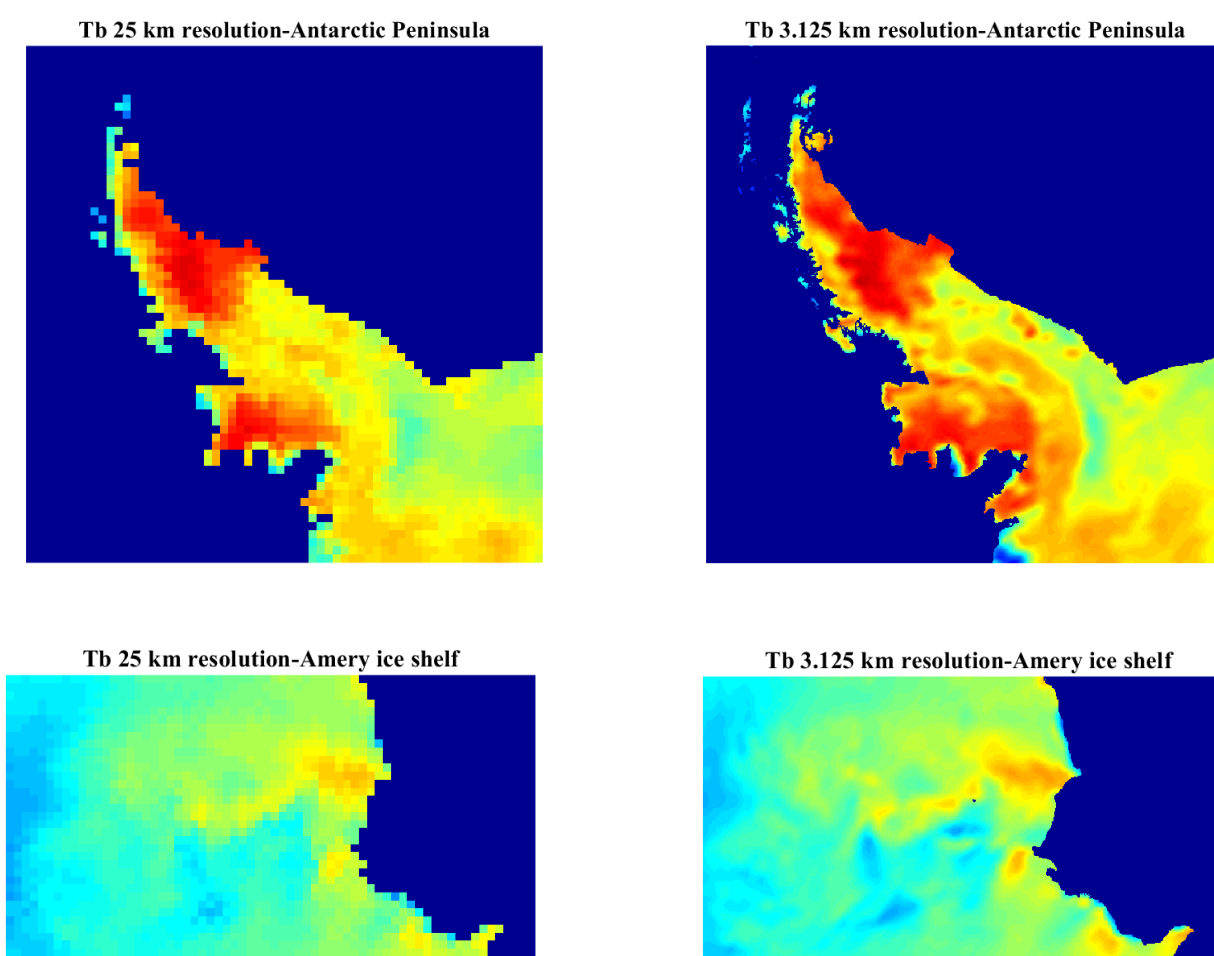


Figure 16: Passive microwave brightness temperature image over Antarctica ice sheet at 25km and 3.125km spatial resolution. At top a detail over Antarctic Peninsula, at bottom the Amery ice shelf.

4.2 Inter-comparison between different sensors

The long temporal coverage that characterizes passive microwave remote sensing data is guaranteed by different sensors placed on different satellites, each covering a certain temporal window. Thus, in order to create a continuous time series from 1979 to 2018 it is necessary to merge data from different sensors that present biases in the measurement of brightness temperature due to differences in characteristics of sensors themselves, such as IFOV, swath width, view angle, altitude and Local-Time-Of-Day. Several relations have been proposed to perform cross calibration of EASE Grid data. Jezek et al. (1991) compared SMMR and SSM/I over the Antarctic ice sheet for K and Ka bands (19GHz and 37GHz) for both horizontal and

vertical polarizations while Steffen et al. (1993) over Greenland for 18GHz and 19GHz. Abdalati et al. (1995) derived relations between SSM/I observations for platforms F08 and F11 over Antarctica and Greenland for 19GHz, 22GHz and 37GHz. Dai et al. (2015) intercalibrated SMMR, SSM/I (F08 and F13) and SSMI/S (F17) over snow covered pixels in China and (2010) SMMR, SSM/I and AMSR-E over the whole earth surfaces selecting hot and cold pixels. Cavalieri et al. (2012) performed inter-sensor calibration comparing SSM/I-F13 and SSMI/S-F17 data for Global sea ice. Stroeve et al. (1998) found the relations between brightness temperature from different sensors to be sensitive to the sampled region for the study. The purpose of this part of the work is to compare enhanced spatial resolution EASE-2.0 brightness temperature data from NASA MEaSUREs project for both Antarctica and Greenland, check the goodness of intercalibration and find relations to be applied in constructing multi-platform time series.

4.2.1 Approach

The general approach to deal with intercalibration between two sensors is to perform a linear regression in order to find slope (m) and intercept (q) of the straight line that best fits the scatter plots of brightness temperature data obtained from two different satellites (Equation 27).

$$y = mx + q, \quad (27)$$

In computing m and q one of the two variables (x) is considered as the independent variable and the other one (y) as the variable dependent on x . Linear regression analysis can be performed both temporally (pixel by pixel, over the whole overlap period) and spatially (day by day, over the whole map). In this work the latter approach has been followed, accordingly with the study of Jezek et al. (1993) in which studied SMMR and SSM/I-F08 data over Antarctic ice sheet.

Since correlation coefficients of each regression exceeded 0.99, they obtained slope and intercept values for each day of overlap and then averaged them to establish a general relation for the whole Antarctic ice sheet. In this work two approaches have been used to obtain m and q .

The first method consists in computing the weighted average between the daily slope and intercept values. Considering n days, for every i -th day m_i , q_i and R_i^2 have been computed and then averaged according to Equations 2 and Equation 3.

$$m = \frac{\sum_{i=1}^n m_i R_i^2}{\sum_{i=1}^n R_i^2}, \quad (28)$$

$$q = \frac{\sum_{i=1}^n q_i R_i^2}{\sum_{i=1}^n R_i^2}, \quad (29)$$

This choice has been done to assign higher significance to results obtained from pairs of data with higher correlation, assumed as the less noise-affected. The second method consists in considering as variables x and y for the linear regression not only all the brightness temperature values in common between maps from two satellites for one day but rather all common values for all common days and then evaluate m and q with a unique linear regression.

Once m and q have been computed a linear relation between two different sensors is available to be applied. In order to test the improvements obtained from the calibrations, histograms have been plotted and compared qualitatively and quantitatively by computing the distance between the two histograms before and after the calibration.

$$D_i = |h_i(T_b^A) - h_i(T_b^B)|, \quad (30)$$

where D_i is the difference between the two histograms A and B for the i -th value of brightness temperature. To evaluate the global difference of the two compared histograms the area under the distance curve as

$$D = \sum_i D_i, \quad (31)$$

$$d = \frac{D_{original} - D_{corrected}}{D_{original}}, \quad (32)$$

With D it is possible to evaluate the distance reduction percentage (d) for the ranges of brightness temperature after the application of the proposed relations, used as indicator of improvement.

4.2.2 Method and results

First of all, in order to focus the study over Greenland and Antarctica only, a Land-Ocean-Coastline-Ice (LOCI) mask (Figure 17) provided by Boston University has been applied keeping the only pixels identified as Ice (Index=101).

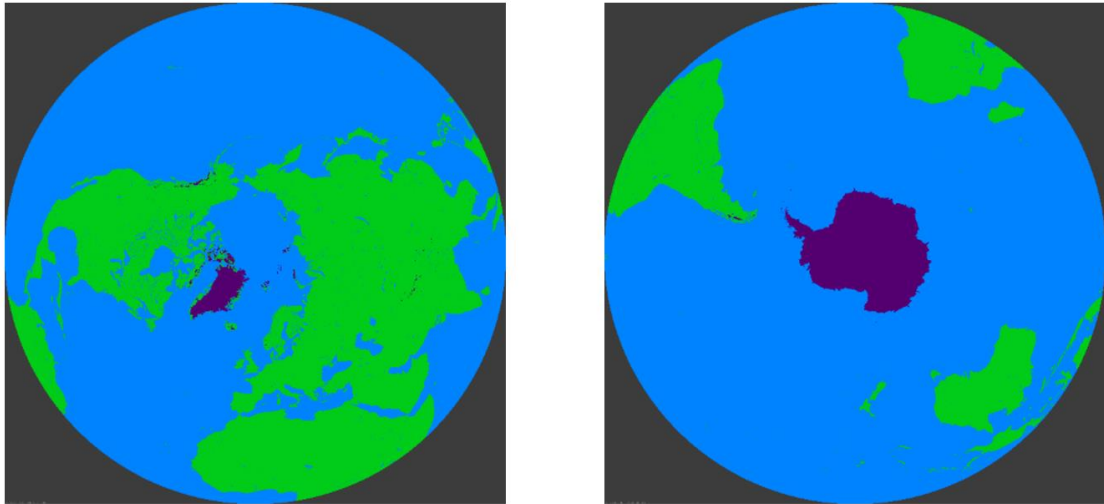


Figure 17: Land-Ocean-Coastline-Ice (LOCI) mask adopted. To the ice areas is assigned the value 101.

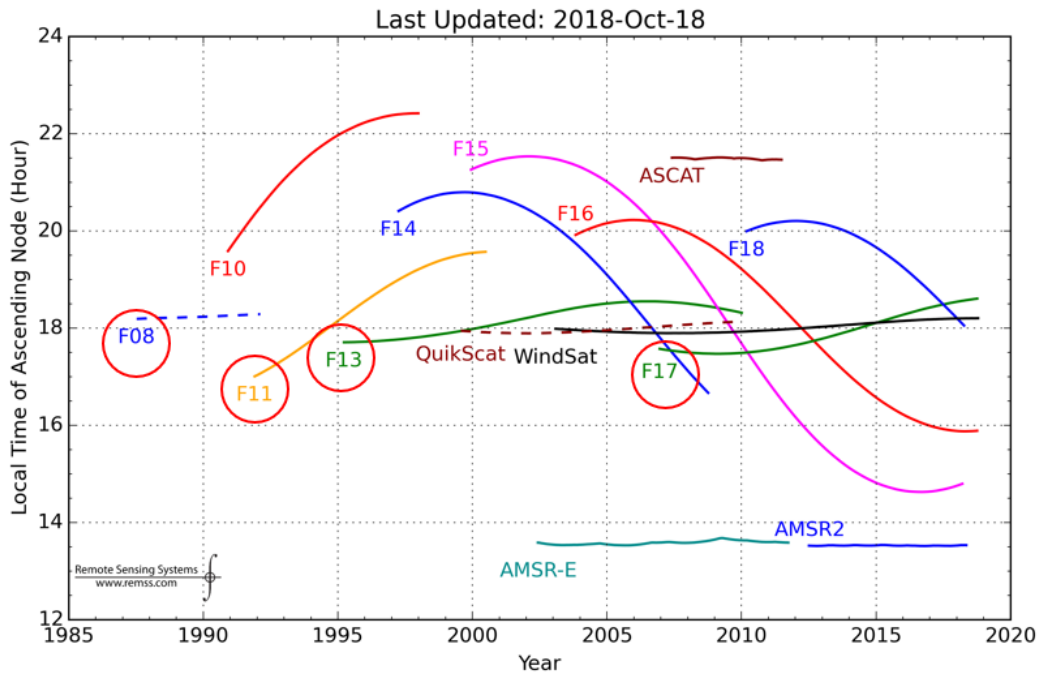


Figure 18: Representation of the stability over the working period of the spaceborne passive microwave satellites. The red circles identify the selected instruments.

The platforms selected for this work are SMMR-Nimbus 7, SSM/I-F08, SSMI/-F11, SSM/I-F13, SSMI/S-F17 because of the higher stability over the working period for what concerns the local time of ascending node (Figure 18). The channel that has been analyzed is 37 GHz channel, horizontal polarization due to its high sensitivity to liquid water content.

The overlap periods selected for this study are:

- (1) 07/09/1987-08/20/1987 for a total of 22 common days (one every two days) for SMMR and SSM/I-F08;
- (2) 12/03/1991-12/18/1991 for a total of 16 common days for SSM/I-F08 and SSM/I-F11 as it is the most consistent overlap period [Abdalati et al. (1995) took 12/08/1991-12/18/1991];
- (3) 05/03/1995-09/30/1995 for a total of 76 common days (one every two days except the missing days to reduce the number of data in the computation) for SSM/I-F11 and SSM/I-F13;
- (4) 03/01/2008-12/10/2008 for a total of 71 common days (one every four days except the missing days to reduce the number of data in the computation) for SSM/I-F13 and SSMI/S-F17;

The short overlap periods for the first two couples of satellites is a limitation for this type of works. In fact, the overlap of the first couple is located temporally between July and August. This window coincides to summer for the northern hemisphere and winter for the southern hemisphere. Hence, there is a different climatic condition resulting in strong differences in brightness temperature values in Greenland and Antarctica. If in these months Antarctic winter lead to low values of brightness temperature, Greenland is characterized by presence of melting area, recognizable with higher Tb values. Thus, the comparison between the first two couple of satellites will be according to low and high values for Greenland and low values only for Antarctica, and vice versa for the second overlap period. For the last two couples the selected overlap period covers a larger window, leading to a more equal type of calibration for both Greenland and Antarctica. The reduction of number of days for the last two couples of satellites has been done to reduce the computational effort.

Firstly, following Jezek et al. (1993), the absolute value of the difference between brightness temperature maps of the same day of overlap period have been computed as first comparison and qualitative evaluation of the magnitude of the bias between satellites. It appears that the greatest difference is between the first two compared products. In fact, 1987 is the overlap year between two different sensor's generations: SMMR and SSM/I. The other couples of products compared in this work come from different satellites but sensor type is the same. As an example, here are plotted differences of Tb for the same day of the year 07/13/1987 and 07/13/1995 for the couples SMMR\SSM/I-F08 and SSM/I-F11\ SSM/I-F13 for both Greenland and Antarctica.

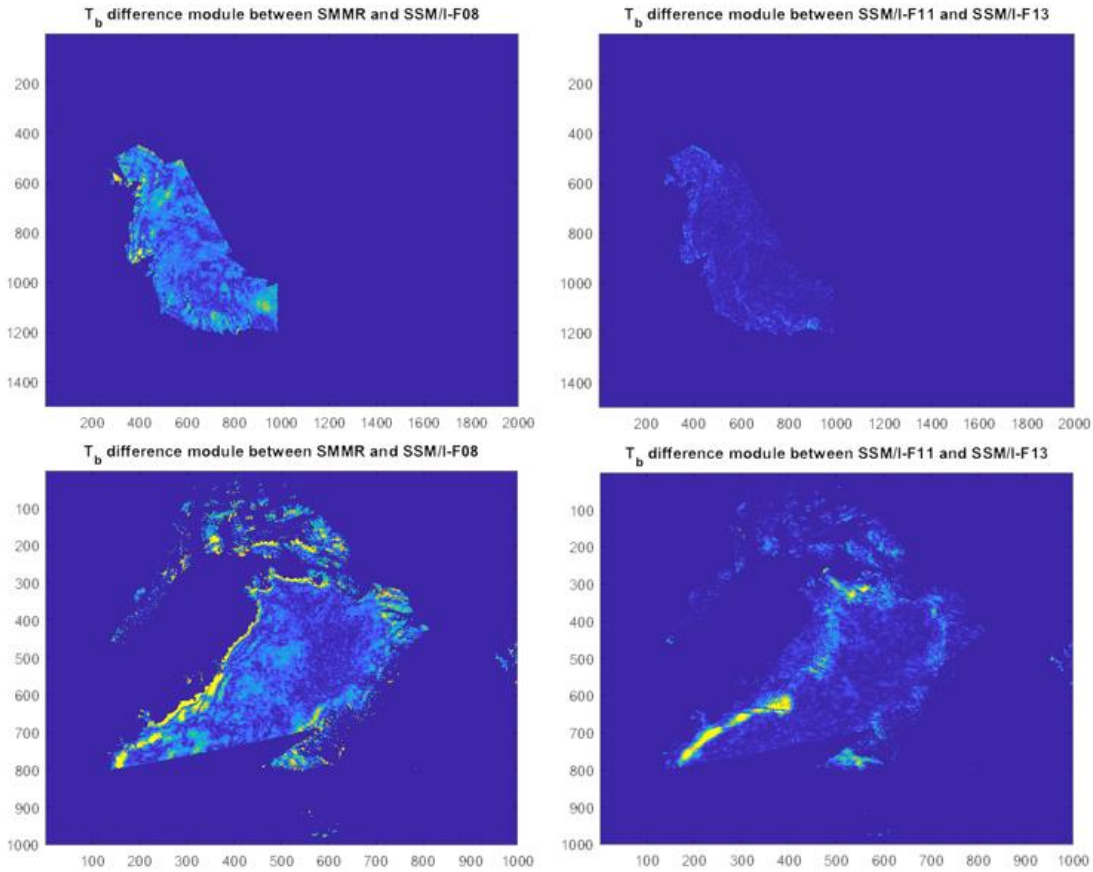


Figure 19: Absolute value of the difference between brightness temperature sensed by SMMR and SSM/I-F08 during the same day of acquisition.

Accordingly, in Antarctica it is possible to recognize a generally higher difference in brightness temperature between SMMR and SSM/I, homogeneously distributed all over the common area sensed by the two sensors of the day considered. Spatial patterns are evident from the presented difference map and have been found also by Jezek et al. (1993) regarding 25 km resolution study.

Maximum, minimum and average values of the difference between pairs of data have been computed and reported in the Table 2. Maximum and minimum differences take large absolute values for every couple of satellite, probably because of the noise of the signal, with a peak for SMMR and SSM/I-F08 evening pass over Greenland possibly for the larger difference in overpass time and the presence of melting in Northern Hemisphere. The average difference is close to 0 K for what concerns SSM/I and SSMI/S products, with the exception of F08-F11 presenting an average difference slightly larger than 1 K, also found in Abdalati et al. (1995) for 25 km resolution data, but ranges from -3.3914 K to -4.2847 K by comparing SMMR and SSM/I-F08.

Antarctica			
Platforms	Max	Min	Average
SMMR-F08 Evening	85.89	-101.62	-4.2847
SMMR-F08 Morning	85.35	-90.26	-3.3914
F08-F11 Evening	63.78	-53.56	1.158
F08-F11 Morning	72.86	-66.56	1.0713
F11-F13 Evening	39.18	-66.13	-0.2112
F11-F13 Morning	50.92	-49.77	-0.1253
F13-F17 Evening	42.96	-54.98	0.0791
F11-F17 Morning	46.6	-44.24	0.286

Greenland			
Platforms	Max	Min	Average
SMMR-F08 Evening	442.33	-131.66	-3.8976
SMMR-F08 Morning	48.93	-60.62	-3.9818
F08-F11 Evening	60.68	-36.2	0.5596
F08-F11 Morning	38.88	-41.55	0.384
F11-F13 Evening	69.97	-59.34	-0.4874
F11-F13 Morning	65.95	-55.31	-0.0824
F13-F17 Evening	86.34	-69.91	0.1588
F11-F17 Morning	74.68	-61.94	0.5176

Table 2: Maximum, minimum and average difference between brightness temperature from overlapping platforms for Antarctica and Greenland.

Linear regression has been performed as described in the previous section through the MATLAB Curve Fitting App. From the toolbox, a code has been generated and implemented as MATLAB function into the `for` loop running over the overlap days. The vectors imported in this code have been created by means of another MATLAB code that reshapes a daily brightness temperature map as column vectors, compares pixels removing from both maps all the pixels presenting NaN value. An example of the code used is presented below, for the case SSM/I-F13 and SSMI/S-F17. Following the calculation of slope and intercept, the linear relations have been applied to the data in order to perform the calibration. In order to check the goodness of the calibration, histograms of brightness temperature have been computed and plotted. Qualitatively,

the purpose is to make the histograms of the pair of data fit. To perform a quantitative evaluation of the improvement, the percentage reduction of the integral of the distance function (d) has been computed. In the following code d is computed only once; it is necessary to run the code again (the second part only) changing the coefficients from *method1* to *method2* to obtain d for the other method.

```

%% LINEAR REGRESSION ALGORITHM

%% Computation of slope and intercepts with methods 1 and 2
clear all
% Choose Greenland or Antarctica folder
addpath('E:\XCALI\greenlandF13-F17')
dirListf13f17=dir(fullfile('E:\XCALI\greenlandF13-F17\*.mat'));
fileListf13f17=char({dirListf13f17.name});
binranges=[100:1:300];

%Give a starting value for the overall vector- NaN will not be read by the
%linear regression tool
Tb2008F13E37Hlong=NaN;
Tb2008F13M37Hlong=NaN;
Tb2008F17E37Hlong=NaN;
Tb2008F17M37Hlong=NaN;
for i=1:size(fileListf13f17,1)
    if mod(i,2)~=0
        try
            filef13f17=strtrim(fullfile(fileListf13f17(i,:),:));
            load(filef13f17);
            % Method1
            % Fitting coefficients vector computation and compilation
            [fitresult, gof]=Fit(Tb2008F13M37Hvector,Tb2008F17M37Hvector);
            mq=coeffvalues(fitresult);
            mF13F17M(i)=mq(1);
            qF13F17M(i)=mq(2);
            rsquareF13F17M(i)=gof.rsquare;
            [fitresult, gof]=Fit(Tb2008F13E37Hvector,Tb2008F17E37Hvector);
            mq=coeffvalues(fitresult);
            mF13F17E(i)=mq(1);
            qF13F17E(i)=mq(2);
            rsquareF13F17E(i)=gof.rsquare;
            [fitresult, gof]=Fit(Tb2008F17M37Hvector,Tb2008F13M37Hvector);
            mq=coeffvalues(fitresult);
            mF17F13M(i)=mq(1);
            qF17F13M(i)=mq(2);
            rsquareF17F13M(i)=gof.rsquare;
            [fitresult, gof]=Fit(Tb2008F17E37Hvector,Tb2008F13E37Hvector);
            mq=coeffvalues(fitresult);
            mF17F13E(i)=mq(1);
            qF17F13E(i)=mq(2);
            rsquareF17F13E(i)=gof.rsquare;

            % Method2
            % create vectors for scatterplots for method 2
            Tb2008F13E37Hlong=[Tb2008F13E37Hlong; Tb2008F13E37Hvector];
            Tb2008F13M37Hlong=[Tb2008F13M37Hlong; Tb2008F13M37Hvector];
            Tb2008F17E37Hlong=[Tb2008F17E37Hlong; Tb2008F17E37Hvector];

```

```

        Tb2008F17M37Hlong=[Tb2008F17M37Hlong; Tb2008F17M37Hvector];
        catch ME
        disp(i)
        end
    end
end

% Method 1 - Compute weighted average of slope and intercept
mF13F17Mmethod1=sum(mF13F17M.*rsquareF13F17M)./sum(rsquareF13F17M);
qF13F17Mmethod1=sum(qF13F17M.*rsquareF13F17M)./sum(rsquareF13F17M);
mF13F17Emethod1=sum(mF13F17E.*rsquareF13F17E)./sum(rsquareF13F17E);
qF13F17Emethod1=sum(qF13F17E.*rsquareF13F17E)./sum(rsquareF13F17E);
mF17F13Mmethod1=sum(mF17F13M.*rsquareF17F13M)./sum(rsquareF17F13M);
qF17F13Mmethod1=sum(qF17F13M.*rsquareF17F13M)./sum(rsquareF17F13M);
mF17F13Emethod1=sum(mF17F13E.*rsquareF17F13E)./sum(rsquareF17F13E);
qF17F13Emethod1=sum(qF17F13E.*rsquareF17F13E)./sum(rsquareF17F13E);

% Method 2 - Remove one-NaN-days
nanF17E=find(isnan(Tb2008F17E37Hlong));
nanF13E=find(isnan(Tb2008F13E37Hlong));
Tb2008F17E37Hlong(nanF13E)=NaN;
Tb2008F13E37Hlong(nanF17E)=NaN;
nanF17M=find(isnan(Tb2008F17M37Hlong));
nanF13M=find(isnan(Tb2008F13M37Hlong));
Tb2008F17M37Hlong(nanF13M)=NaN;
Tb2008F13M37Hlong(nanF17M)=NaN;

% Method 2 - Second fitting method
[fitresult, gof]=Fit(Tb2008F13M37Hlong,Tb2008F17M37Hlong);
mq=coeffvalues(fitresult);
mF13F17Mmethod2=mq(1);
qF13F17Mmethod2=mq(2);
rsquareF13F17Mmethod2=gof.rsquare;
[fitresult, gof]=Fit(Tb2008F13E37Hlong,Tb2008F17E37Hlong);
mq=coeffvalues(fitresult);
mF13F17Emethod2=mq(1);
qF13F17Emethod2=mq(2);
rsquareF13F17Emethod2=gof.rsquare;

[fitresult, gof]=Fit(Tb2008F17M37Hlong,Tb2008F13M37Hlong);
mq=coeffvalues(fitresult);
mF17F13Mmethod2=mq(1);
qF17F13Mmethod2=mq(2);
rsquareF17F13Mmethod2=gof.rsquare;
[fitresult, gof]=Fit(Tb2008F17E37Hlong,Tb2008F13E37Hlong);
mq=coeffvalues(fitresult);
mF17F13Emethod2=mq(1);
qF17F13Emethod2=mq(2);
rsquareF17F13Emethod2=gof.rsquare;

%% Histograms

% To apply relations found apply method1 or method2 at the linear relations
% (just change the number)
bincountsF13E=histc(Tb2008F13E37Hlong,binranges);
bincountsF17E=histc(Tb2008F17E37Hlong,binranges);
TbEF17c=mF13F17Emethod2.*Tb2008F13E37Hlong+qF13F17Emethod2;
TbEF13c=mF17F13Emethod2.*Tb2008F17E37Hlong+qF17F13Emethod2;

```

```

bincountsF13Ec=histc (TbEF13c,binranges) ;
bincountsF17Ec=histc (TbEF17c,binranges) ;
bincountsF13M=histc (Tb2008F13M37Hlong,binranges) ;
bincountsF17M=histc (Tb2008F17M37Hlong,binranges) ;
TbMF17c=mF13F17Mmethod2.*Tb2008F13M37Hlong+qF13F17Mmethod2;
TbMF13c=mF17F13Mmethod2.*Tb2008F17M37Hlong+qF17F13Mmethod2;
bincountsF13Mc=histc (TbMF13c,binranges) ;
bincountsF17Mc=histc (TbMF17c,binranges) ;

% Distance function
DistF17F13E=abs (bincountsF13E-bincountsF17E) ;
DistF17F17CE=abs (bincountsF17E-bincountsF17Ec) ;
DistF13F13CE=abs (bincountsF13E-bincountsF13Ec) ;
DistF17F13M=abs (bincountsF13M-bincountsF17M) ;
DistF17F17CM=abs (bincountsF17M-bincountsF17Mc) ;
DistF13F13CM=abs (bincountsF13M-bincountsF13Mc) ;

% Global distance reduction
sumF17F13E=sum (DistF17F13E) ;
sumF17F17CE=sum (DistF17F17CE) ;
sumF13F13CE=sum (DistF13F13CE) ;
sumF17F13M=sum (DistF17F13M) ;
sumF17F17CM=sum (DistF17F17CM) ;
sumF13F13CM=sum (DistF13F13CM) ;

dF17F17CE= (sumF17F13E-sumF17F17CE) ./sumF17F13E;
dF13F13CE= (sumF17F13E-sumF13F13CE) ./sumF17F13E;
dF17F17CM= (sumF17F13M-sumF17F17CM) ./sumF17F13M;
dF13F13CM= (sumF17F13M-sumF13F13CM) ./sumF17F13M;

```

Code 1

For SMMR-SSM/I linear regression, slopes and intercepts have been found different from unit for both Greenland and Antarctica. Moving to SSM/I and SSMI/S data slopes and intercepts assume values closer to unit. Coefficients of determination R² for SMMR-F08 couple resulted larger for Antarctica than for Greenland but smaller with respect to the results obtained by Jezek et al. (1993) for 25 km resolution data. Since swath-to-grid algorithms are affected by higher noise at higher spatial resolution (Brodzik et al., 2018), the presence of lower values of coefficients of determination can be a consequence of this noisy characteristic of the signal. However, for SSM/I and SSMI/S comparison, R² reaches generally higher values, overcoming 0.99 for Antarctica F11-F13 comparison. According with Abdalati et al. (1995), larger coefficients of determination have been found in Greenland, confirming the higher stability of sensors in winter seasons due to the smaller diurnal temperature cycle and the absence of melting events. For SMMR-F08, histograms of brightness temperature of both Antarctica and Greenland appear to not perfectly fit (Figures 21 and 22) showing an evident distance. On the other hand,

SSM/I and SSMI/S data present good overlap of histograms for every couple of satellites, in accordance with the small values of average difference found.

After the application of the linear relations found by regression, the corrected brightness temperature histograms have been compared with the original ones. Graphically the histograms of one of the two corrected brightness temperatures appear to better fit the other one in the case of the first two satellites (SMMR-SMMRC figure 21 and 22). Moreover, the computed values of distance reduction percentage d are positive for both methods 1 and 2, indicating an improvement of consistency. Differently, corrections of the other couples of platforms do not lead to significant improvements since original data were already well calibrated and presented average difference close to 0. Furthermore, in some cases negative values of d have been found indicating that the application of linear relation found in the way presented make the consistency worse. It is evident that the overlap between SMMR and SSM/I-F08 of 1987 shows higher differences and higher benefit coming from the correction we adopted. In the Figure 20 histogram of difference between TbSMMR and TbF08 are presented. It is possible to see that histograms follow a Gauss distribution with peak shifted closer to 0 after the correction (method 1). In appendix the results of the comparison of the other couples of satellites is reported.

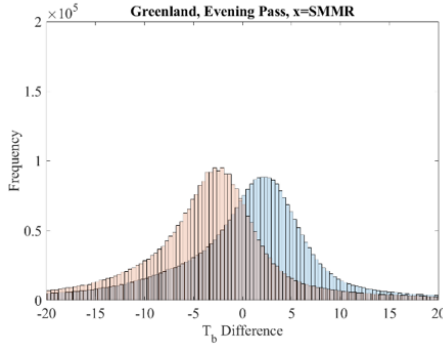
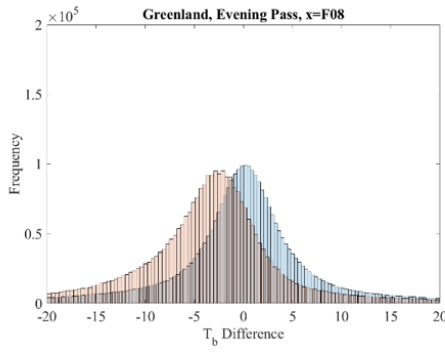
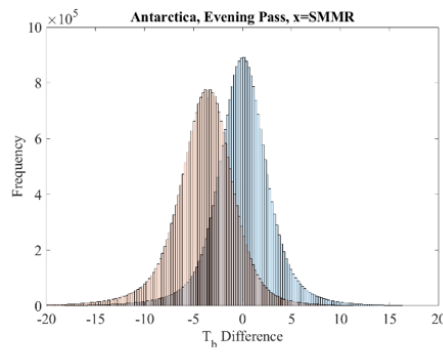
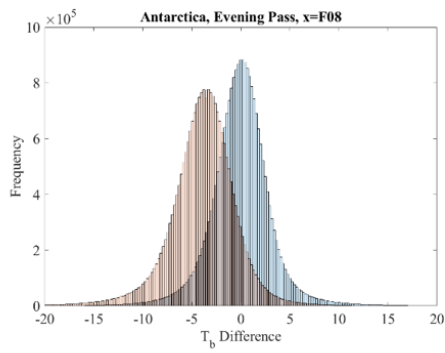
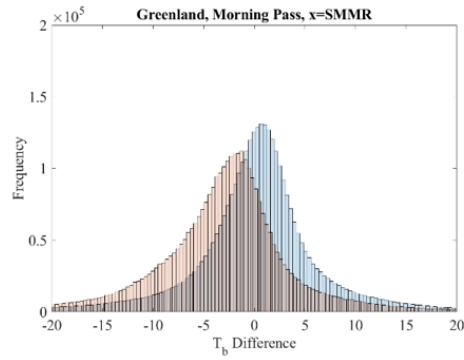
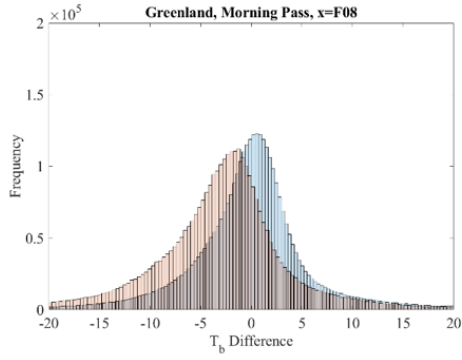
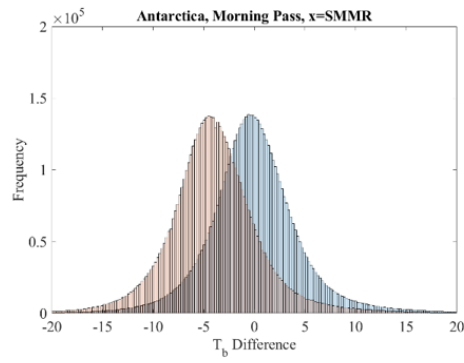
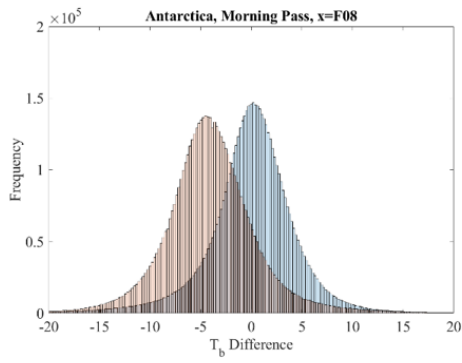
4.2.3 Conclusions

The comparison between the brightness temperature EASE 2.0 gridded data obtained from pairs of satellites in the overlapping periods showed a greater difference in the oldest pair, with values ranging from -3.3914 K to -4.2847 K. In the other pairs, formed by sensors of the same type, differences were found to be almost zero.

By applying the linear relationships calculated by means of linear regression for the first pair of sensors it is possible to obtain an improvement in the consistency, reducing on average the bias between the data. This improvement is confirmed by the largest values of reduction of distance percentage d found for the couple SMMR and SSM/I-F08 and by the position centered mostly around zero of the histograms of the difference between the data after the calibration.

In order to have the maximum improvement of the consistency of the time series it is necessary to choose a reference data set and correct all the other data to make them correspond to the fixed ones. We suggest considering as fixed reference the SSM/I-SSMI/S 1987-2018 time series since it is temporally longer than the SMMR coverage, it already presents good consistency

(as resulted from this analysis) and 1979-1987 data are collected every other day. Hence, a correction of SMMR leaves unmodified the longest and most consistent part of the time series. Coefficients can be found in the second part of the following tables (one for Greenland and one for Antarctica), referred as $X=SMMR$.



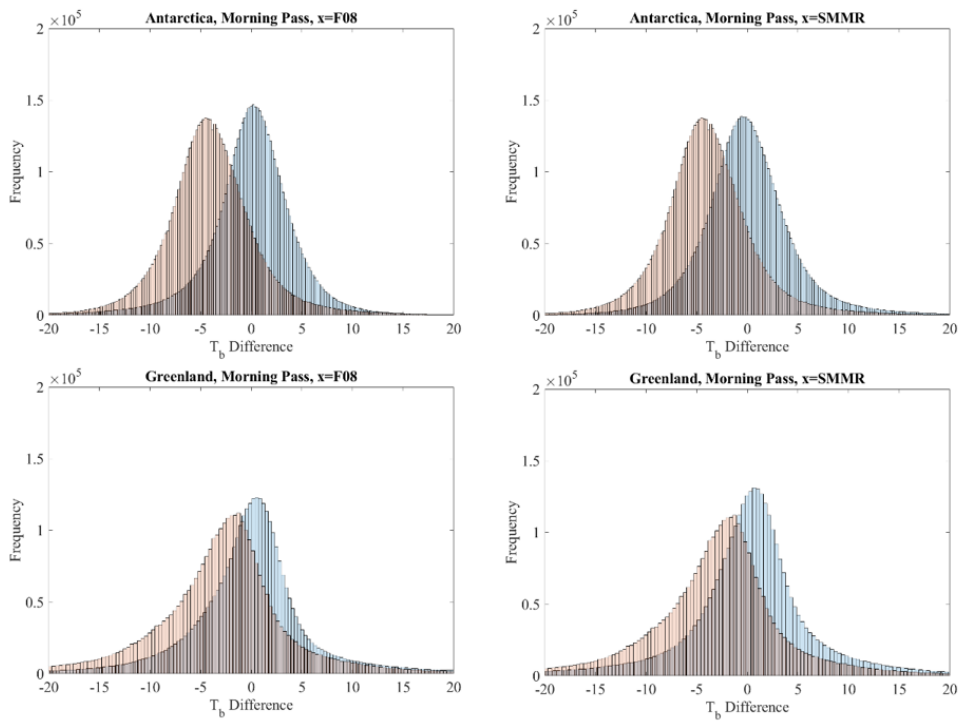


Figure 20: Histograms of difference between SMMR and SSM/I brightness temperature before (red) and after (blue) the application of the linear relations found.

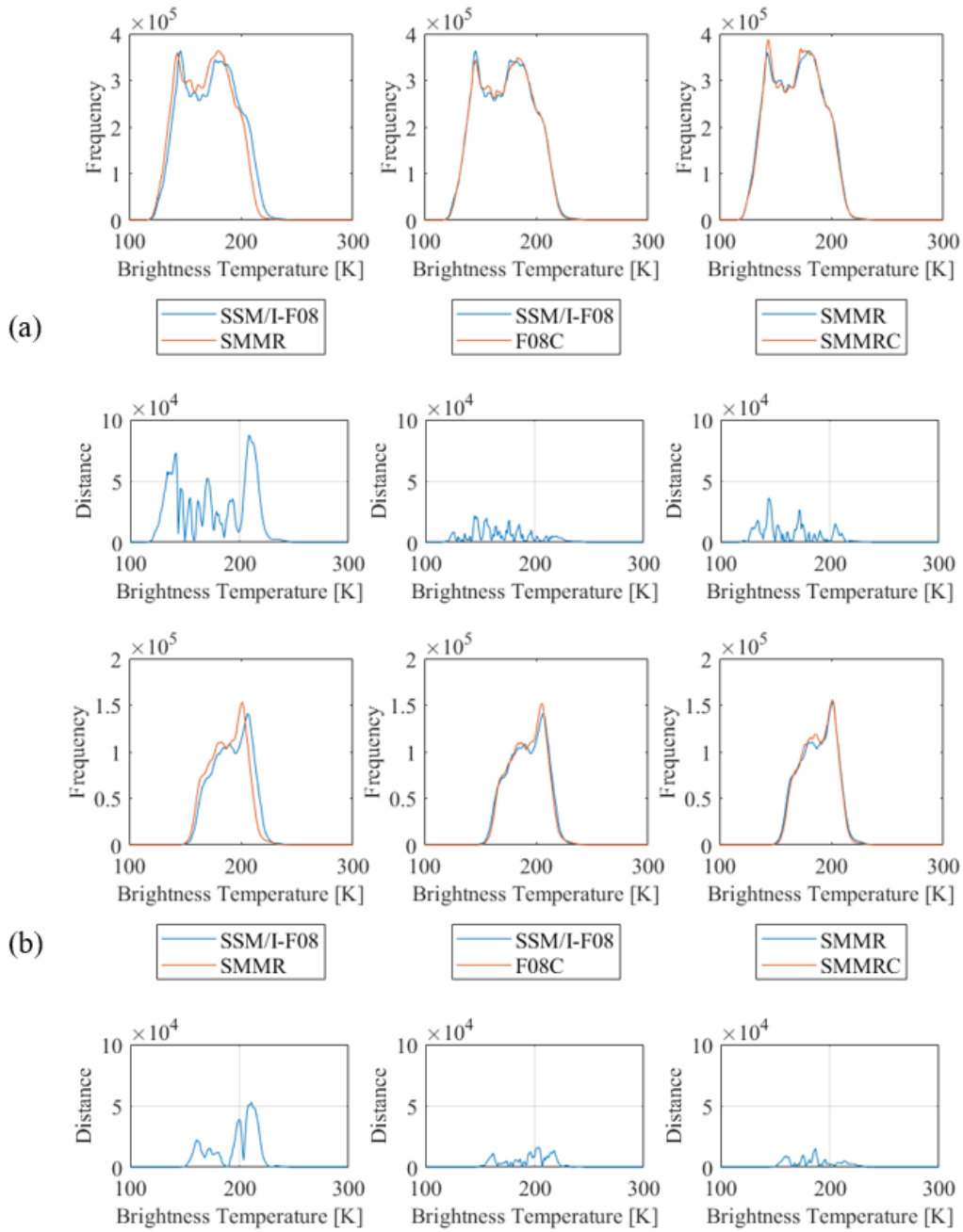


Figure 21: Brightness temperature histograms before and after the application of the intercalibration relations, Antarctica. Relations are applied for both evening (a) and morning (b) passes, reporting the histograms of the data (top) and the distance between the histograms (bottom) for original data (left), applying the correction to SMMR data (center) and to the SSM/I data (right).

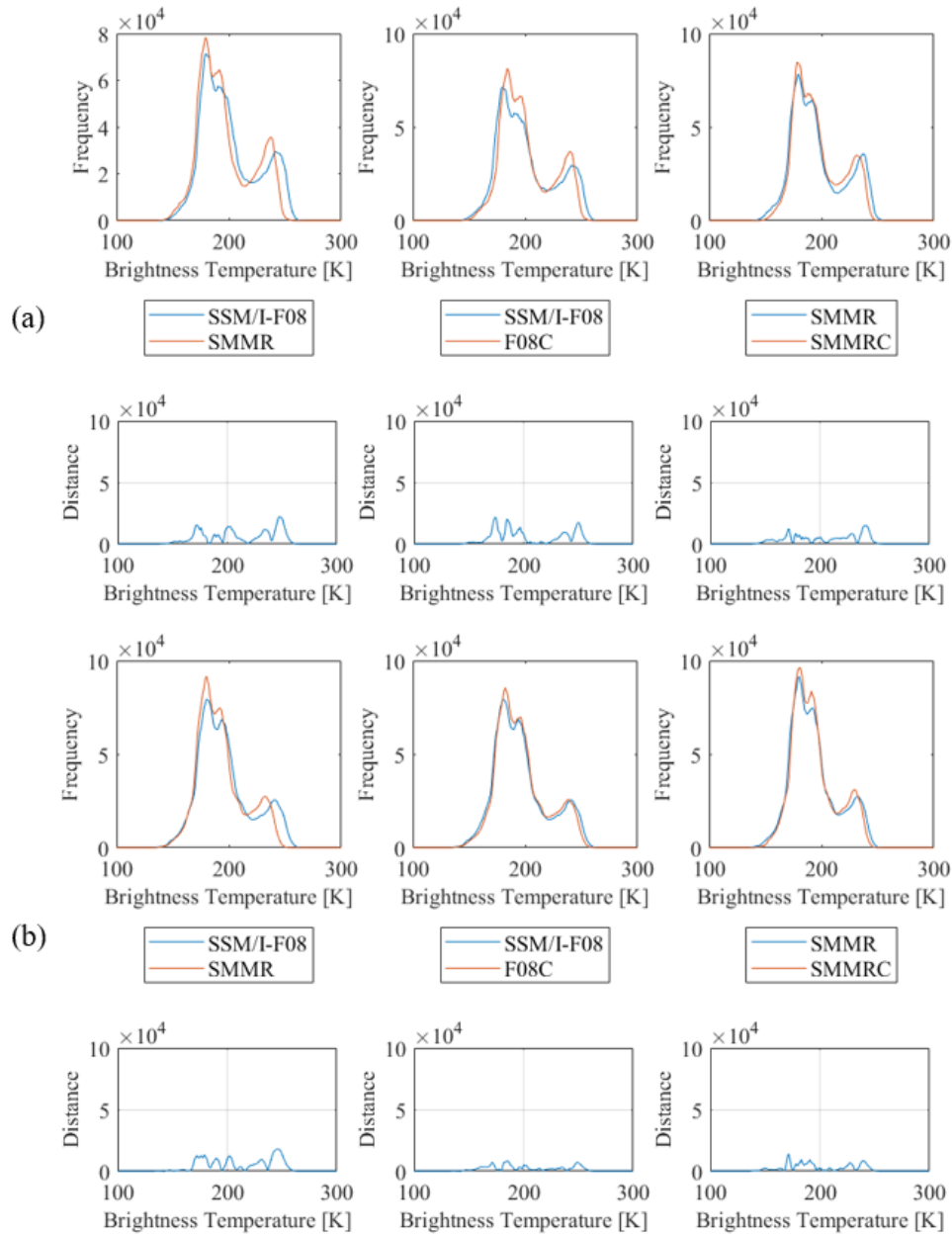


Figure 22: Brightness temperature histograms before and after the application of the intercalibration relations, Greenland. Relations are applied for both evening (a) and morning (b) passes, reporting the histograms of the data (top) and the distance between the histograms (bottom) for original data (left), applying the correction to SMMR data (center) and to the SSM/I data (right).

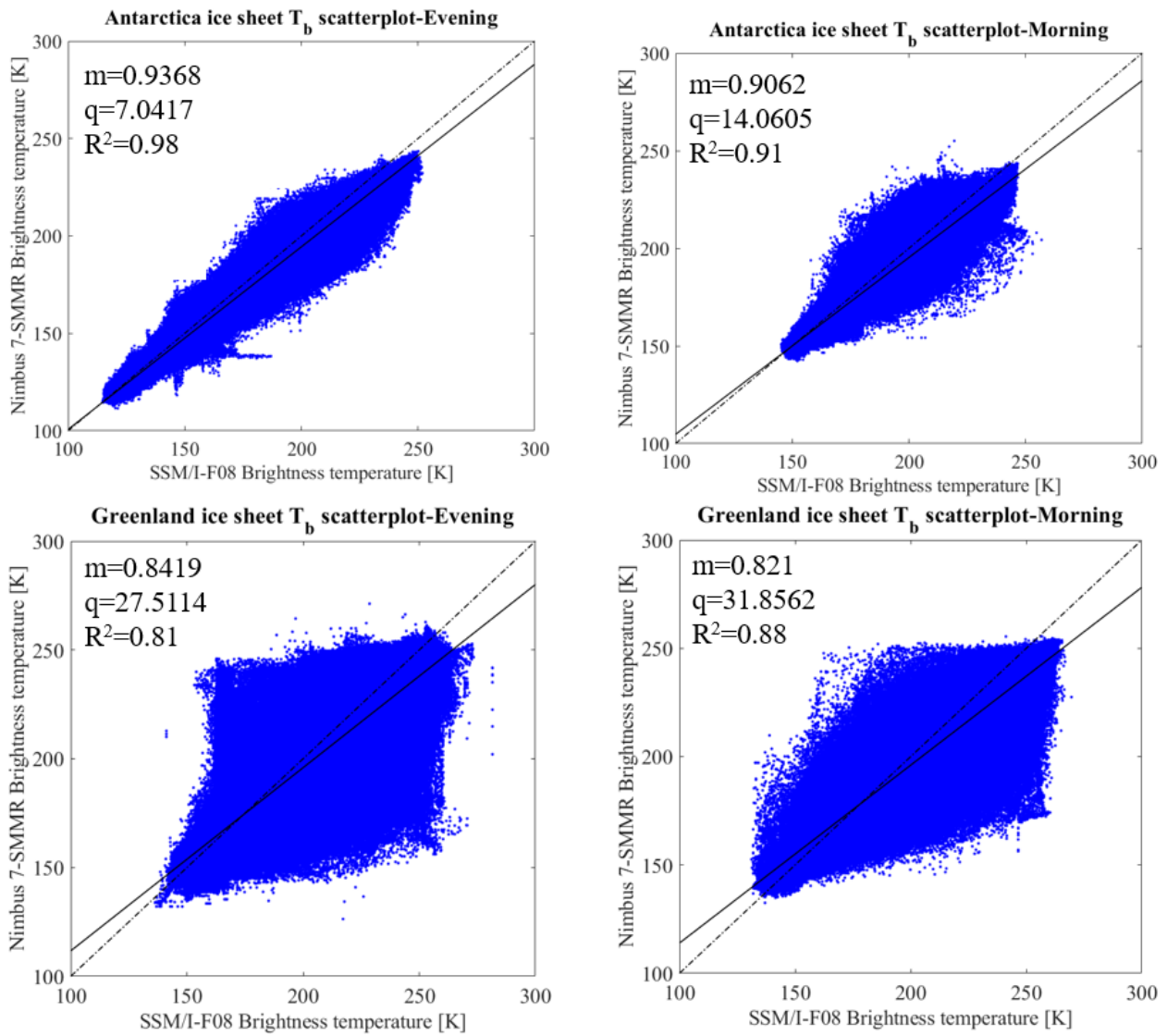


Figure 23: Scatter plots of SMMR and SSM/I-F08 brightness temperature data for overlap period over Antarctica (at the top) and Greenland (at the bottom) for evening (left) and morning (right) passes. Black lines show the linear fitting where dashed black line show the 1:1 line.

Antarctica							
X=F08	m_1	m_2	q_1	q_2	R^2_2	d_1	d_2
Morning	0.9108	0.9062	13.2273	14.0605	0.9115	0.7414	0.7686
Evening	0.9368	0.9368	7.0417	7.0492	0.9796	0.3829	0.7728
X=SMMR	m_1	m_2	q_1	q_2	R^2_2	d_1	d_2
Morning	0.9991	1.0059	4.0517	2.8712	0.9115	0.6225	0.6633
Evening	1.0455	1.0457	-3.7954	-3.8374	0.9796	0.8138	0.8168
Greenland							
X=F08	m_1	m_2	q_1	q_2	R^2_2	d_1	d_2
Morning	0.818	0.821	32.3868	31.8562	0.8803	0.6865	0.4616
Evening	0.8494	0.8419	26.0269	27.5114	0.8127	0.1204	0.3316
X=SMMR	m_1	m_2	q_1	q_2	R^2_2	d_1	d_2
Morning	1.0753	1.0722	-11.1399	-10.5807	0.8803	0.557	0.5157
Evening	0.9635	0.9653	11.4237	11.1226	0.8127	0.0937	0.1227

Table 3: Linear regression coefficients (m and q), coefficients of determination (R²) and difference function (d) for Greenland and Antarctica ice sheets. Pedix 1 and 2 refers to the method adopted.

4.3 Data availability and organization

Once the calibration has been performed, a more consistent time series is available to be adopted. However, the different sensors collect data with different temporal resolution. In fact, if SSM/I and SSMI/S sensors collect data at a daily timescale, the SMMR sensor records data every other day. Moreover, there are some missing days of records due to satellite malfunctioning, leading to temporal gaps in the timeseries; the missing days are reported in the following table (<https://nsidc.org/data/pm/smmr-ssmi-data-availability>).

EASE-Grid Projection	
1987	1987-08-25 to 1987-08-26, 1987-10-06 to 1987-10-07, 1987-12-03 to 1987-12-31
1988	1988-01-01 to 1988-01-12, 1988-05-06 to 1988-05-09, 1988-09-23, 1988-12-25 to 1988-12-27
1989	1989-06-07, 1989-07-23 to 1989-07-24, 1989-10-23
1990	1990-08-13, 1990-08-25 to 1990-08-26, 1990-10-21 to 1990-10-22, 1990-10-26 to 1990-10-28, 1990-12-22 to 1990-12-26
1991	1991-12-27 (F8 only)
1992	1992-06-18
1993	1993-01-04
1994	1994-07-20, 1994-11-20 to 1994-11-21
1995	1995-05-21*
1996	1996-12-01
1998	1998-03-11
2000	2000-12-01
2001	No missing dates
2002	No missing dates
2003	No missing dates
2004	No missing dates

2005	No missing dates
2006	No missing dates
2007	2007-01-22 to 2007-02-01, 2007-03-08 to 2007-03-12, 2007-07-10 to 2007-07-17
2008	2008-03-19 to 2008-03-25, 2008-10-30
2009	No missing dates
2010	2010-06-28
2011	No missing dates
2012	2012-03-31
2013	2013-11-26 to 2013-11-27
2014	2014-01-07, 2014-11-07, 2014-12-19
2015	2015-04-15, 2015-05-19, 2015-06-22, 2015-06-26, 2015-06-30, 2015-07-04, 2015-08-06, 2015-08-18 to 2015-08-19, 2015-08-28, 2015-09-15, 2015-10-27, 2015-11-07
2016	2016-04-05, 2016-05-04 ⁺ , 2016-06-19, 2016-09-09, 2016-10-16, 2016-12-28
2017	2017-11-02
2018	2018-01-20, 2018-06-26, 2018-07-05, 2018-09-17, 2018-10-02

Table 4: List of missing brightness temperature data for every year.

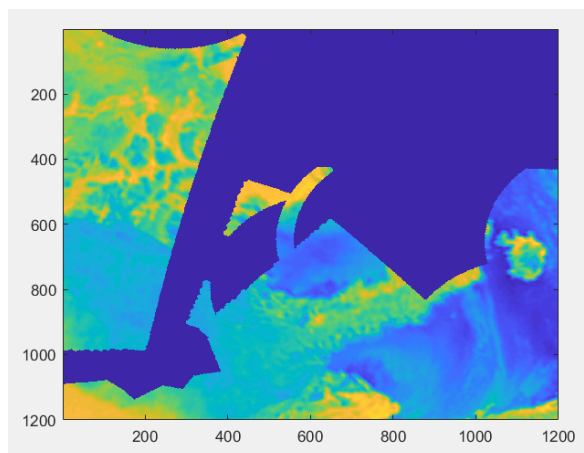


Figure 24: Example of spatially missing brightness temperature data of Northern Hemisphere around Greenland ice sheet.

In addition, a lot of NaN pixels are present, as shown in figure. This difference in data record between the different sensors and the presence of spatial and temporal missing values represent a limitation in the quantification of melting days for the period 1979-1987. In literature, different approaches have been adopted to fill the voids and create a complete dataset. Zwally and Fiegles (1994) double counted the day before the missing date. Torinesi et al. (2002) completed the voids by linear interpolation of the data. In this work we adopt this second methodology by applying an interpolation algorithm to the portion of interest of the global maps. Moreover, in order to be able to account for possible interpolation errors, the algorithm developed creates a cell array map containing the vectors indicating the days of the year corresponding to the interpolated values for every pixel. In this way every user of the interpolated product can identify real measurements and distinguish the estimated ones. In addition, since some melt detection algorithms discussed in Chapter 3 and selected for this work are based on the winter mean brightness temperature (dry snow conditions), this algorithm generate maps of winter average to be used afterwards to compute the threshold maps. The choice of cell arrays to contain the data has been done after considerations related to the use of CPU and memory in MATLAB of the developed algorithms in the processes of heavy map files. Since the limitation in this case is in the amount of memory used to load the files, we selected the cell array since it is the less memory consuming. To perform the interpolation, it has been necessary to merge consecutive years to avoid unstable value interpolated at the beginning and the end of the time series due to missing boundary values. In practice, to create the timeseries of the maps of the i -th year, the first 30 days of the $(i-1)$ -th and the last 30 days of $(i+1)$ -th year have been used to have for every year at least an initial and final value outside the range of the i -th year.

The final result is a *.mat* file for each year containing two cell arrays representing the interpolated brightness temperature (morning and evening passes) with size $365*2$ (or $366*2$) containing on the left cell the number of the day and on the right cell the interpolated map matrix, two cell arrays with size $1200*1200$ for Greenland ($2000*1500$ for Antarctica) containing in each cell a vector containing the days in which the value of brightness temperature has been computed by interpolation and two $1200*1200$ for Greenland ($2000*1500$ for Antarctica) containing the winter average of brightness temperature, considered as the average of the Tb of January and February for Greenland (July and August for Antarctica).

Greenland2012.mat (MAT-file)	
Name	Value
InterpolatedTbNE	1200x1200 cell
InterpolatedTbNM	1200x1200 cell
TbNE	366x2 cell
TbNM	366x2 cell
WinterMeanTbNE	1200x1200 double
WinterMeanTbNM	1200x1200 double

Figure 25: Outputs of the interpolation algorithm.

```

%% Interpolation Monoplatform
%% 1994-F11

clear all

% Add folder path of year of interest and +1 -1 and Mask
addpath('/home/pcolosio/outputs/InterpTb');
addpath('/data/mtedesco/Marco_37H/matfiles_37H');

%Create file list (NorthMorning, NorthEvening)
%Files in the same folder on the server

dirListNE=dir(fullfile('/data/mtedesco/Marco_37H/matfiles_37H/NSIDC-0630-
EASE2_N3.125km-F11_SSMI-1994*E-SIR-CSU-v1.3.mat'));
fileListNE=char({dirListNE.name});
dirListNM=dir(fullfile('/data/mtedesco/Marco_37H/matfiles_37H/NSIDC-0630-
EASE2_N3.125km-F11_SSMI-1994*M-SIR-CSU-v1.3.mat'));
fileListNM=char({dirListNM.name});

dirListNE_1=dir(fullfile('/data/mtedesco/Marco_37H/matfiles_37H/NSIDC-0630-
EASE2_N3.125km-F11_SSMI-1993*E-SIR-CSU-v1.3.mat'));
fileListNE_1=char({dirListNE_1.name});
dirListNE1=dir(fullfile('/data/mtedesco/Marco_37H/matfiles_37H/NSIDC-0630-
EASE2_N3.125km-F11_SSMI-1995*E-SIR-CSU-v1.3.mat'));
fileListNE1=char({dirListNE1.name});

dirListNM_1=dir(fullfile('/data/mtedesco/Marco_37H/matfiles_37H/NSIDC-0630-
EASE2_N3.125km-F11_SSMI-1993*M-SIR-CSU-v1.3.mat'));
fileListNM_1=char({dirListNM_1.name});
dirListNM1=dir(fullfile('/data/mtedesco/Marco_37H/matfiles_37H/NSIDC-0630-
EASE2_N3.125km-F11_SSMI-1995*M-SIR-CSU-v1.3.mat'));
fileListNM1=char({dirListNM1.name});

%Open binary Mask File (5760*5760) /home/pcolosio/Mask/EASE2_N3.125km.LO-
CImask_land50_coast0km.5760x5760.bin
%Mask for North

fidMaskN=fopen('/home/pcolosio/Mask/EASE2_N3.125km.LO-
CImask_land50_coast0km.5760x5760.bin','r');
MaskN=fread(fidMaskN,[5760 5760] , 'uint8');
fclose(fidMaskN);

%Creation of Cell Arrays containing Tb map every day

```

```

for n=1:size(fileListNE,1)
    try
        fileNM=strtrim(fileListNM(n,:));
        load(fileNM);
        TbNM(n,:)={n,TB(1901:3100,2601:3800)};
    catch
        nan=NaN(1200,1200);
        TbNM(n,:)={n,nan};
    end
    try
        fileNE=strtrim(fileListNE(n,:));
        load(fileNE);
        TbNE(n,:)={n,TB(1901:3100,2601:3800)};
    catch
        nan=NaN(1200,1200);
        TbNE(n,:)={n,nan};
    end
end

%Creation of cell arrays of year +1/-1

for p=1:20
    try
        fileNE1=strtrim(fileListNE1(p,:));
        load(fileNE1);
        TbNE1(p,:)={p,TB(1901:3100,2601:3800)};
    catch
        nan=NaN(1200,1200);
        TbNE1(p,:)={p,nan};
    end

    try
        fileNM1=strtrim(fileListNM1(p,:));
        load(fileNM1);
        TbNM1(p,:)={p,TB(1901:3100,2601:3800)};
    catch
        nan=NaN(1200,1200);
        TbNM1(p,:)={p,nan};
    end

    try
        fileNE_1=strtrim(fileListNE_1(size(fileListNE_1,1)-21+p,:));
        load(fileNE_1);
        TbNE_1(p,:)={p,TB(1901:3100,2601:3800)};
    catch
        nan=NaN(1200,1200);
        TbNE_1(p,:)={p,nan};
    end

    try
        fileNM_1=strtrim(fileListNM_1(size(fileListNM_1,1)-21+p,:));
        load(fileNM_1);
        TbNM_1(p,:)={p,TB(1901:3100,2601:3800)};
    catch
        nan=NaN(1200,1200);
        TbNM_1(p,:)={p,nan};
    end
end

```

```

end
clear TB

%Interpolation of time series on each pixel of interest
%Indexes h and k are according to the dimensions of arrays contained in
%cell arrays (width and length of map)

for h=1:1200
    for k=1:1200
        if MaskN(1900+h,2600+k)==101

            %create year series

            for l=1:size(fileListNE,1)

                seriesNE(l)=TbNE{l,2}(h,k);
                seriesNM(l)=TbNM{l,2}(h,k);

            end

            %Create the series extentions

            for p=1:20

                elongationseriesNE1(p)=TbNE1{p,2}(h,k);
                elongationseriesNM1(p)=TbNM1{p,2}(h,k);
                elongationseriesNE_1(p)=TbNE_1{p,2}(h,k);
                elongationseriesNM_1(p)=TbNM_1{p,2}(h,k);

            end

            dayNE=[1:1:(size(fileListNE,1)+40)];
            dayNM=[1:1:(size(fileListNM,1)+40)];

            %Create the extended series

            extNE=horzcat(elongationseriesNE_1,seriesNE,elongationseriesNE1);
            extNM=horzcat(elongationseriesNM_1,seriesNM,elongationseriesNM1);

            %find zeros and nan and put an empty value
            zerosNE=find(extNE==0);
            nanNE=find(isnan(extNE));
            zerosNM=find(extNM==0);
            nanNM=find(isnan(extNM));

            extNE(zerosNE)=[];
            dayNE(zerosNE)=[];
            extNE(nanNE)=[];
            dayNE(nanNE)=[];
            extNM(zerosNM)=[];
            dayNM(zerosNM)=[];
            extNM(nanNM)=[];
            dayNM(nanNM)=[];

            %Interpolation

            %interpolation
            TbrightnessNE=interp1(dayNE,extNE,[1:1:(size(fileListNE,1)+40)],'pchip');

```

```

TbrightnessNM=interp1(dayNM,extNM,[1:1:(size(fileListNE,1)+40)],'pchip');

    %fill cell array with interpolated values
    for m=1:size(fileListNE,1)

        TbNE{m,2}(h,k)=(TbrightnessNE(m+20));
        TbNM{m,2}(h,k)=(TbrightnessNM(m+20));

    end

    %winter mean computation
    for j=1:60
        janfebTbNE(j)=TbNE{j,2}(h,k);
        janfebTbNM(j)=TbNM{j,2}(h,k);
    end
    WinterMeanTbNE(h,k)=mean(janfebTbNE);
    WinterMeanTbNM(h,k)=mean(janfebTbNM);

    %cell array of nanvectors containing the positions of
    %interpolated values
    InterpolatedTbNE{h,k}=nanNE;
    InterpolatedTbNM{h,k}=nanNM;

else
    WinterMeanTbNE(h,k)=0;
    WinterMeanTbNM(h,k)=0;
    InterpolatedTbNE{h,k}=0;
    InterpolatedTbNM{h,k}=0;

end
end
end

%Save the cube
%Add path of the folder where to save the interpolated data

save(['/home/pcolosio/outputs/InterpTb/Green-
land1994.mat'],'TbNE','TbNM','InterpolatedTbNE','InterpolatedTbNM','Winter-
MeanTbNE','WinterMeanTbNM','-v7.3');

```

Code 2

References of section 2

- Abdalati, W., Steffen, K., Otto, C., & Jezek, K. C. (1995). Comparison of brightness temperatures from SSMI instruments on the DMSP F8 and FII satellites for Antarctica and the Greenland ice sheet. *International Journal of Remote Sensing*, 16(7), 1223-1229.
- Abdalati, W., & Steffen, K. (1995). Passive microwave-derived snow melt regions on the Greenland ice sheet. *Geophysical Research Letters*, 22(7), 787-790.
- Ashcraft, I. S., & Long, D. G. (2006). Comparison of methods for melt detection over Greenland using active and passive microwave measurements. *International Journal of Remote Sensing*, 27(12), 2469-2488.
- Armstrong, R., K. Knowles, M. Brodzik and M. A. Hardman. 1994, updated current year. DMSP SSM/I-SSMIS Pathfinder Daily EASE-Grid Brightness Temperatures. Version 2. Boulder, Colorado USA: NASA DAAC at the National Snow and Ice Data Center.
- Backus, G.E. and J. F. Gilbert. 1967. Numerical applications of a formalism for geophysical inverse problems, *Geophys. J. R. Astron. Soc.*, vol. 13, pp. 247–276.
- Backus, G.E. and J. F. Gilbert. 1968. Resolving power of gross Earth data, *Geophys. J. R. Astron. Soc.*, vol. 16, pp. 169–205.
- Brodzik, M. J. and K. W. Knowles. 2002. “EASE-Grid: a versatile set of equal-area projections and grids” in M. Goodchild (Ed.) *Discrete Global Grids*. National Center for Geographic Information & Analysis, Santa Barbara, CA: USA.
- Brodzik, M. J., B. Billingsley, T. Haran, B. Raup and M. H. Savoie. 2012. EASE-Grid 2.0: Incremental but Significant Improvements for Earth-Gridded Data Sets. *ISPRS Int. J. Geo-Inf.*, 1:32–45. doi: 10.3390/ijgi101003.
- Brodzik, M. J., Long, D. G., Hardman, M. A., Paget, A., & Armstrong, R. L. MEaSURES Calibrated Enhanced-Resolution Passive Microwave Daily EASE-Grid 2.0 Brightness Temperature ESDR, Version 1; National Snow and Ice Data Center: Boulder, CO, USA, 2016. Updated 2018. Digital Media. Available online: <http://nsidc.org/data/nsidc-0630> (accessed on 7 November 2018).
- Brun, E., David, P., Sudul, M., & Brunot, G. (1992). A numerical model to simulate snow-cover stratigraphy for operational avalanche forecasting. *Journal of Glaciology*, 38(128), 13-22.

Caccin, B., C. Roberti, P. Russo and A. Smaldone. 1992. The Backus–Gilbert inversion method and the processing of sampled data, *IEEE Trans. Signal Processing*, vol. 40, pp. 2823–2825.

Cavalieri, D. J., Parkinson, C. L., DiGirolamo, N., & Ivanoff, A. (2012). Intersensor calibration between F13 SSMI and F17 SSMIS for global sea ice data records. *IEEE Geoscience and remote sensing letters*, 9(2), 233-236.

Dai, L., & Che, T. (2010, November). Cross-platform calibration of SMMR, SSM/I and AMSR-E passive microwave brightness temperature. In *Sixth International Symposium on Digital Earth: Data Processing and Applications* (Vol. 7841, p. 784103). International Society for Optics and Photonics.

Dai, L., Che, T., & Ding, Y. (2015). Inter-calibrating SMMR, SSM/I and SSMIS data to improve the consistency of snow-depth products in China. *Remote Sensing*, 7(6), 7212-7230.

Dee, D. P., Uppala, S. M., Simmons, A. J., Berrisford, P., Poli, P., Kobayashi, S., ... & Bechtold, P. (2011). The ERA-Interim reanalysis: Configuration and performance of the data assimilation system. *Quarterly Journal of the royal meteorological society*, 137(656), 553-597.

Farrar, M. R., & Smith, E. A. (1992). Spatial resolution enhancement of terrestrial features using deconvolved SSM/I microwave brightness temperatures. *IEEE Transactions on Geoscience and Remote Sensing*, 30(2), 349-355.

Jezeq, K. C., Merry, C. J., & Cavalieri, D. J. (1993). Comparison of SMMR and SSM/I passive microwave data collected over Antarctica. *Annals of Glaciology*, 17, 131-136.

Joshi, M., Merry, C. J., Jezeq, K. C., & Bolzan, J. F. (2001). An edge detection technique to estimate melt duration, season and melt extent on the Greenland ice sheet using passive microwave data. *Geophysical Research Letters*, 28(18), 3497-3500.

Knowles, K. E., Njoku, G., Armstrong, R., & Brodzik, M. (2000). *Nimbus-7 SMMR Pathfinder Daily EASE-Grid Brightness Temperatures, version 1*. NASA National Snow Ice Data Center Distributed Active Archive Center: Boulder, CO, USA.

Knowles, K., M. Savoie, R. Armstrong and M. Brodzik. 2006. *AMSR-E/Aqua Daily EASE-Grid Brightness Temperatures*. Boulder, Colorado USA: NASA DAAC at the National Snow and Ice Data Center.

Liu, H., Wang, L., & Jezeq, K. C. (2005). Wavelet-transform based edge detection approach to derivation of snowmelt onset, end and duration from satellite passive microwave measurements. *International Journal of Remote Sensing*, 26(21), 4639-4660.

Long, D. G., & Daum, D. L. (1998). Spatial resolution enhancement of SSM/I data. *IEEE Transactions on Geoscience and Remote Sensing*, 36(2), 407-417.

Macelloni, G., Paloscia, S., Pampaloni, P., & Tedesco, M. (2001). Microwave emission from dry snow: A comparison of experimental and model results. *IEEE Transactions on Geoscience and Remote Sensing*, 39(12), 2649-2656.

Macelloni, G., Paloscia, S., Pampaloni, P., Brogioni, M., Ranzi, R., & Crepaz, A. (2005). Monitoring of melting refreezing cycles of snow with microwave radiometers: The Microwave Alpine Snow Melting Experiment (MASMEx 2002-2003). *IEEE Transactions on Geoscience and Remote Sensing*, 43(11), 2431-2442.

Matzler, C., & Wegmuller, U. (1987). Dielectric properties of freshwater ice at microwave frequencies. *Journal of Physics D: Applied Physics*, 20(12), 1623.

Pampaloni, P., Macelloni, G., Paloscia, S., Poggi, P., Zecchetto, S., Ranzi, R., & Crepaz, A. (2004, September). Microwave remote sensing and hydrological modelling of snow melting cycle. In *IGARSS 2004. 2004 IEEE International Geoscience and Remote Sensing Symposium* (Vol. 3, pp. 1645-1648). IEEE.

Pampaloni, P., Macelloni, G., Paloscia, S., Tedesco, M., Ranzi, R., Tomirotti, M., ... & Crepaz, A. (2003, July). The Microwave Alpine Snow Melting Experiment (MASMEx 2002): A contribution to the ENVISNOW project. In *IGARSS 2003. 2003 IEEE International Geoscience and Remote Sensing Symposium. Proceedings (IEEE Cat. No. 03CH37477)* (Vol. 2, pp. 848-850). IEEE.

Poe, G. A. (1990). Optimum interpolation of imaging microwave radiometer data. *IEEE Transactions on geoscience and remote sensing*, 28(5), 800-810.

Ramage, J. M., & Isacks, B. L. (2002). Determination of melt-onset and refreeze timing on southeast Alaskan icefields using SSM/I diurnal amplitude variations. *Annals of Glaciology*, 34, 391-398.

Robinson, W. D., Kummerow, C., & Olson, W. S. (1992). A technique for enhancing and matching the resolution of microwave measurements from the SSM/I instrument. *IEEE transactions on Geoscience and Remote Sensing*, 30(3), 419-429.

Sihvola, A. H. (1999). Electromagnetic mixing formulas and applications (No. 47). Iet.

Steiner, N., & Tedesco, M. (2014). A Wavelet Melt Detection Algorithm Applied to Enhanced Resolution Scatterometer Data over Antarctica (2000-2009).

Stogryn, A. (1978). Estimates of brightness temperatures from scanning radiometer data. *IEEE Transactions on Antennas and Propagation*, 26(5), 720-726.

Stroeve, J., Maslanik, J., & Xiaoming, L. (1998). An intercomparison of DMSP F11-and F13-derived sea ice products. *Remote Sensing of Environment*, 64(2), 132-152.

Tedesco, M., Abdalati, W., & Zwally, H. J. (2007). Persistent surface snowmelt over Antarctica (1987–2006) from 19.35 GHz brightness temperatures. *Geophysical Research Letters*, 34(18).

Tedesco, M. (2007). Snowmelt detection over the Greenland ice sheet from SSM/I brightness temperature daily variations. *Geophysical Research Letters*, 34(2).

Tedesco, M. (2009). Assessment and development of snowmelt retrieval algorithms over Antarctica from K-band spaceborne brightness temperature (1979–2008). *Remote Sensing of Environment*, 113(5), 979-997.

Tedesco, M., Brodzik, M., Armstrong, R., Savoie, M., & Ramage, J. (2009). Pan arctic terrestrial snowmelt trends (1979–2008) from spaceborne passive microwave data and correlation with the Arctic Oscillation. *Geophysical Research Letters*, 36(21).

Tedesco, M. (2014). *Remote sensing of the cryosphere*. John Wiley & Sons.

Torinesi, O., Fily, M., & Genthon, C. (2003). Variability and trends of the summer melt period of Antarctic ice margins since 1980 from microwave sensors. *Journal of Climate*, 16(7), 1047-1060.

Ulaby, F. T., Moore, R. K., & Fung, A. K. (1986). *Microwave remote sensing: Active and passive*. Volume 3-From theory to applications.

Wiesmann, A., & Mätzler, C. (1999). Microwave emission model of layered snowpacks. *Remote Sensing of Environment*, 70(3), 307-316.

Section 3

5 Snowmelt over Greenland and Antarctica

In this chapter we apply a selection of the algorithms described in Chapter 3 to detect and map melting over Greenland and Antarctica ice sheets.

Firstly, we evaluate the different algorithms applied to the enhanced resolution dataset, evaluating qualitatively and quantitatively the behavior and the performances, performing a validation using in situ data and outputs of a regional climate model.

Secondly, after the computation of melting maps on a daily scale for the whole 37 years time series, we evaluate trends for significant melting indicators previously proposed in literature and melting season.

Finally, we discuss the effects detected by PMW sensors of the extreme melting event during the year 2012.

5.1 Assessment of snowmelt retrieval algorithms

5.1.1 Data used for validation

Greenland and Antarctica air/surface temperature data

We use data recorded by stations of the Greenland Climate Network (GC-Net; Steffen et al., 1996) to assess the performance of the enhanced resolution product in detecting the presence of liquid water over the Greenland ice sheet. The 18 AWSs provide continuous measurements of air temperature, wind speed, wind direction, humidity, pressure and other parameters. In the absence of direct observations of melting, we use air temperature (3 m) to extrapolate those instances when liquid water is present, following the procedure adopted by Tedesco (2009). We focus on four stations: (1) Summit (72° 34' 47" N, 38° 30' 16" W, Elevation 3254 m a.s.l.), located in the dry snow zone, when melting generally does not occur, (2) Swiss Camp (69° 34' 06" N, 49° 18' 57" W, Elevation 1149 m a.s.l.) and (3) JAR1 (69° 29' 54" N, 49° 40' 54" W, Elevation 962 m a.s.l.), located in the ablation region, and (4) Humboldt (78° 31' 36" N, 56° 49'

50° W, Elevation 1995 m a.s.l.), located at higher elevation where melting may occur or not. More information about the GC-Net dataset can be found at <http://cires1.colorado.edu/steffen/gcnet/>.

To assess the performance of meltwater detection algorithms over the Antarctica ice sheet we use surface/air temperature data collected by AWS in the framework of Antarctica Automatic Weather Stations Program (AAWSP). Differently to air/surface data from GC-Net (hourly collected), here we adopt a hourly average of the data collected every 10 minutes. We focus on two locations, adopted also in Tedesco (2009), where melting generally occurs: (1) Larsen Ice Shelf (67.97 S, 60.55 W, 17 m a.s.l.) and Uranus Glacier (71.43 S, 68.93 W, Elevation 780 m a.s.l.) stations.

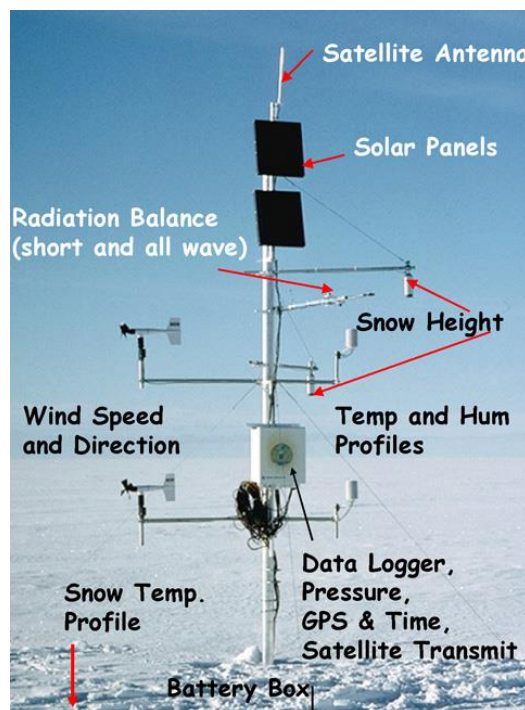


Figure 26: Automatic weather station of Greenland Climate Network.

Modèle Atmosphérique Regional (MAR) data

In addition to satellite and in situ measurements, we use outputs from Modèle Atmosphérique Régional (MAR) to compare the results obtained from the enhanced resolution PMW dataset at 3.125 km here presented with the coarser resolution dataset over Greenland. MAR is a modular atmospheric model that uses the sigma-vertical coordinate to simulate airflow over complex terrain and the Soil Ice Snow Vegetation Atmosphere Transfer scheme (SISVAT)

[e.g., De Ridder and Gallée, 1998] as the surface model. MAR outputs have been assessed over Greenland [e.g., Fettweis et al., 2005; Alexander et al., 2014]. The snow model in MAR, which is based on the CROCUS model of Brun et al. (1992), calculates albedo for snow and ice as a function of snow grain properties, which in turn depend on energy and mass fluxes within the snowpack. Lateral and lower boundary conditions are prescribed from reanalysis datasets. Sea-surface temperature and sea-ice cover are prescribed using the same reanalysis data. The atmospheric model within MAR interacts with the CROCUS model, which provides the state of the snowpack and associated quantities (e.g., albedo, grain size). In this study we use outputs from MAR version v3.9 characterized by an enhanced computational efficiency and improved snow model parameters (Fettweis et al., 2017). The model is forced at the boundaries using ERA-Interim reanalysis (see Dee et al. (2011) for detailed description) at spatial resolution of 7.5 km. In order, to compare outputs from MAR and the estimates of meltwater extent obtained from PMW data, we average the LWC simulated by MAR along the vertical profile, as done in Fettweis et al., 2007. Note that we only use MAR outputs over Greenland because, despite available also over Antarctica, the spatial resolution of the MAR outputs currently available (35 km) is too coarse to be compared with the results of the enhanced resolution product.

5.1.2 Discussion

In this work we use T-B algorithms only. We applied the fixed threshold of 245 K (denoted as 245K, from this point), the increment of 30 K over the winter brightness temperature (M+30) with two respective sensitivity analysis of 35 K (M+35) and 40 K (M+40) and the thresholds coming from the microwave emission model of layered snowpack considering LWC=0.2% (MEMLS). Here the MATLAB algorithm used to create the binary melting maps is presented.

```
%% Melting Map Greenland 1994

clear all
tic
addpath('/home/pcolosio/outputs/InterpTb');
addpath('/home/pcolosio/outputs/MeltingMaps');
addpath('/home/pcolosio/Mask');

%Load brightness temperature file (the beautiful one you created)
load('/home/pcolosio/outputs/InterpTb/Greenland1994.mat')

%Open binary Mask File (5760*5760)
%Mask for North
```

```

dirListMaskN=dir(fullfile('/home/pcolosio/Mask/EASE2_N3.125km.LO-
CI_mask_land50_coast0km.5760x5760.bin'));
fileListMaskN=char({dirListMaskN.name});
fidMaskN=fopen(fileListMaskN,'r');
MaskN=fread(fidMaskN,[5760 5760] , 'uint8');
fclose(fidMaskN);

%Thresholds

%Mplus30/35/40
TcE=WinterMeanTbNE+30;
TcM=WinterMeanTbNM+30;
TcE2=WinterMeanTbNE+35;
TcM2=WinterMeanTbNM+35;
TcE3=WinterMeanTbNE+40;
TcM3=WinterMeanTbNM+40;

%MEMLS2
TcE4=.48.*WinterMeanTbNE+128;
TcM4=.48.*WinterMeanTbNM+128;

%245K
TcE5=245;%K
TcM5=245;%K

%Fixed 245K

for i=1:size(TbNE,1)

    TbM=TbNM{i,2};

    TbE=TbNE{i,2};

    TbM((MaskN(1901:3100,2601:3800))~=101)=0;
    TbM(TbM<=TcM5)=0;
    indexM=TbM>0;

    TbE((MaskN(1901:3100,2601:3800))~=101)=0;
    TbE(TbE<=TcE5)=0;
    indexE=TbE>0;

    MeltPixM(i,:)={i,indexM};
    MeltPixE(i,:)={i,indexE};

End

save(['/home/pcolosio/outputs/MeltingMaps/GreenlandMelt-
ing2451994.mat'],'MeltPixE','MeltPixM','-v7.3');

%WinterMean plus 30

for i=1:size(TbNE,1)

    TbM=TbNM{i,2};

    TbE=TbNE{i,2};

    TbM((MaskN(1901:3100,2601:3800))~=101)=0;

```

```

TbM(TbM<=TcM)=0;
indexM=TbM>0;

TbE((MaskN(1901:3100,2601:3800))~=101)=0;
TbE(TbE<=TcE)=0;
indexE=TbE>0;

MeltPixM(i,:)={i,indexM};
MeltPixE(i,:)={i,indexE};

end

save(['/home/pcolosio/outputs/MeltingMaps/GreenlandMelting1994.mat'],'Melt-
PixE','MeltPixM','-v7.3');

%WinterMean plus 35

for i=1:size(TbNE,1)

    TbM=TbNM{i,2};

    TbE=TbNE{i,2};

    TbM((MaskN(1901:3100,2601:3800))~=101)=0;
    TbM(TbM<=TcM2)=0;
    indexM=TbM>0;

    TbE((MaskN(1901:3100,2601:3800))~=101)=0;
    TbE(TbE<=TcE2)=0;
    indexE=TbE>0;

    MeltPixM(i,:)={i,indexM};
    MeltPixE(i,:)={i,indexE};

end

save(['/home/pcolosio/outputs/MeltingMaps/GreenlandMelt-
ingTcMplus35K1994.mat'],'MeltPixE','MeltPixM','-v7.3');

%WinterMean plus 40

for i=1:size(TbNE,1)

    TbM=TbNM{i,2};

    TbE=TbNE{i,2};

    TbM((MaskN(1901:3100,2601:3800))~=101)=0;
    TbM(TbM<=TcM3)=0;
    indexM=TbM>0;

    TbE((MaskN(1901:3100,2601:3800))~=101)=0;
    TbE(TbE<=TcE3)=0;
    indexE=TbE>0;

    MeltPixM(i,:)={i,indexM};
    MeltPixE(i,:)={i,indexE};

end

```

```

save(['~/home/pcolosio/outputs/MeltingMaps/GreenlandMeltingTcMplus40K1994.mat'], 'MeltPixE', 'MeltPixM', '-v7.3');

%MEMLS2

for i=1:size(TbNE,1)

    TbM=TbNM{i,2};

    TbE=TbNE{i,2};

    TbM((MaskN(1901:3100,2601:3800))~=101)=0;
    TbM(TbM<=TcM4)=0;
    indexM=TbM>0;

    TbE((MaskN(1901:3100,2601:3800))~=101)=0;
    TbE(TbE<=TcE4)=0;
    indexE=TbE>0;

    MeltPixM(i,:)={i,indexM};
    MeltPixE(i,:)={i,indexE};

end

save(['~/home/pcolosio/outputs/MeltingMaps/GreenlandMeltingTc-
MEMLS1994.mat'], 'MeltPixE', 'MeltPixM', '-v7.3');
toc

```

Code 3

The code creates for each threshold selected a cell array containing 365 (366) binary maps in which pixels where melting is detected are assigned with the value 1, non-melting pixels with value 0.

In this part we first discuss the application of the selected T-B algorithms, providing a qualitative evaluation of the strength and limitations of these approaches. Then, a quantitative evaluation proposed by Tedesco (2009) has been adopted to quantify the performances of the methodology adopted. Then, using both AWS and MAR data, we compare the results and quantify the improvements in melt detection obtained by means of the enhanced resolution product.

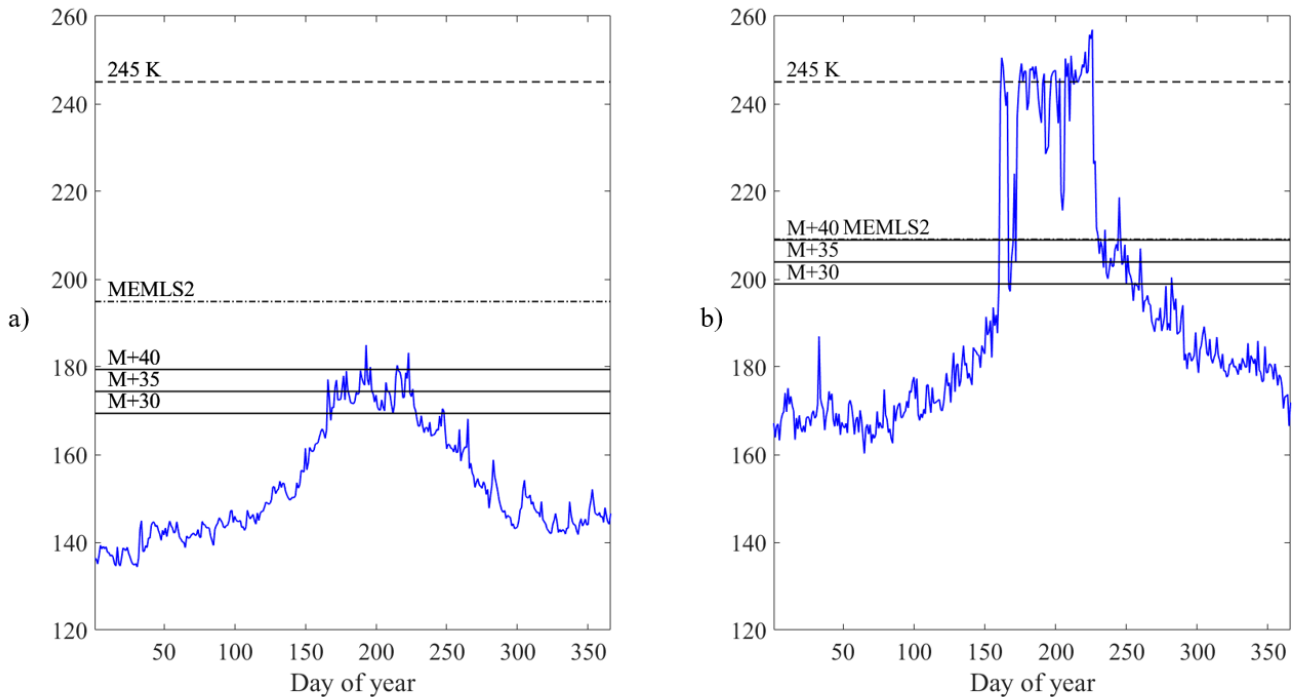


Figure 27: Time series of enhanced Tb at 37 GHz, horizontal polarization, over two pixels of Greenland with a) no melting and b) melting occurring throughout the year 2008. Threshold values obtained with the different detection algorithms are also reported as horizontal lines.

Considerations on the selected algorithms

Figure 27 shows the time series of enhanced Tb at 37 GHz, horizontal polarization, over two locations where melting is not present (Figure 27a) and where it is occurring during summer (Figure 27b). The threshold values obtained with the different detection algorithms are also reported as horizontal lines. Specifically, MEMLS indicates the value obtained using the MEMLS model in the case of 0.2 % LWC, 245k indicates the algorithm using the fixed threshold value of 245 K, and M+30K, M+35K and M+40K indicate the approach considering the winter mean plus, respectively, 30K, 35K and 40K. The values of 35K and 40K were selected to test the sensitivity of the Zwally and Fiegles (1994) approach to the threshold value and to evaluate whether a more conservative approach for this algorithm might reduce the number of false positive instances detected with this algorithm (e.g., when PMW indicates that melting is occurring when it is not). The time series of Tb values shown in Figure 27a clearly indicate that no melting occurs for that pixel. Consistently, both the MEMLS and the 245K algorithms do not suggest the presence of liquid water (e.g., threshold values are higher than the maximum Tb). However, the M+30K (and

similar algorithms) suggest a threshold value that is too low, hence pointing out to the potential presence of melting. We also note that the choice of 30K suggests the presence of melting for most of the summer months, where the choice of 40K suggests melting only for a few days. This points out to an extreme sensitivity of this approach to the choice of the threshold value, especially in those cases (like this one), when the mean winter T_b value is relatively low and the summer T_b peak is mainly driven by the seasonal increase of surface temperature rather than by the presence of melting. Melting clearly occurs in the case of Figure 27b, characterized by the sharp and substantial increase of T_b beginning around mid-May. For this case, all algorithms detect melting, with the M+30K being the most sensitive and the 245K fixed threshold being the most conservative one. However, we note that the M+30K (and in part also the M+35K) detects melting during September where it might not occur. Indeed, melting can be assumed to be over when the sharp drop in the recorded T_b occurs around day 240. After this, the relatively high T_b values are very likely associated with relatively higher surface temperatures. This false detection problem of M+30, M+35 and M+40 appears to follow spatial patterns related to the winter brightness temperature mean. The areas affected the most are in fact the ones characterized by a very low winter T_b value while (generally dry all the year) while in areas with higher winter T_b the overdetection problem is lower, as it can be seen in southern areas. This problem disappears completely in the case of 245 K algorithm and almost completely in case of MEMLS algorithm. This is because M+ ΔT_b algorithms, even considering the snow conditions before the melting season taking the average of the winter brightness temperature, do not take into account these properties in the computation of the increment ΔT_b . In fact, these threshold algorithms consist in a rigid translation of a fixed ΔT of the winter mean surface. On the contrary, MEMLS algorithm is based on the linear regression of the ΔT_b as function of different combinations of dry snow condition (LWC=0) i.e. different winter brightness temperature mean. Accordingly, the transformation of the winter mean surface is not a simple rigid translation but a linear transformation, providing an appropriate threshold value taking into account the conditions of the snow before melting and, at the same time, following a more consistent approach related to the amount of LWC to be detected in the snowpack. It is still necessary to notice that this problem of overdetection is not associated to every dry pixel, as it can be seen in Figure 29 showing the timeseries of T_b and T_{air} at Summit, location generally not affected by melting. For what concerns 245 K algorithm, it appears to be the most conservative, detecting melting only when T_b reaches the highest values. This is consistent with the idea that above the value of 245 K there is no further increment in brightness temperature due to an increment of LWC. Beside the timeseries, Figure

10 shows the melt detection maps obtained using the different approaches for the day July 13th, 2008. Also, in this case the M+30K and M+35K algorithms suggest melting up to high elevations, within the dry snow zone. The analysis of in-situ data and reanalysis surface temperature (not shown here) indicates that this was not the case, pointing again to the potential overestimation of melting for these two approaches. The M+40K and MEMLS show similar results where the approach using the fixed threshold of 245K shows, as expected, the most conservative estimates.

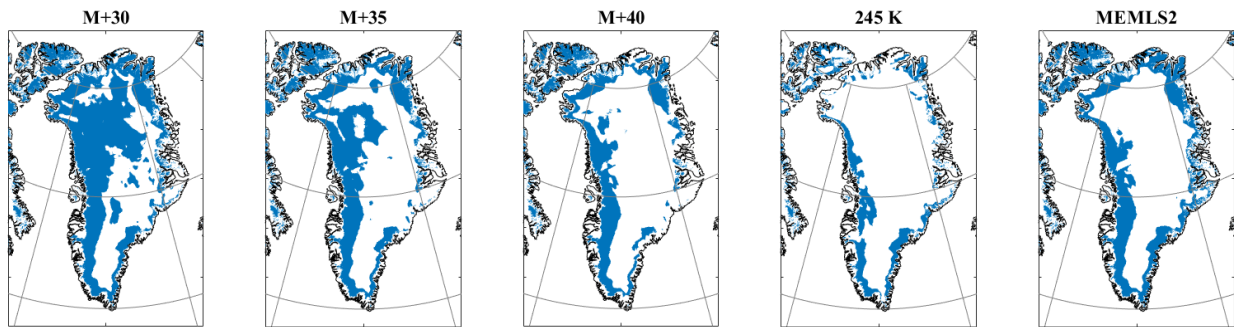


Figure 28: Melting maps obtained by using M+30, M+35, M+40, 245K and MEMLS2 algorithms over Greenland Ice sheet on July 13th, 2008.

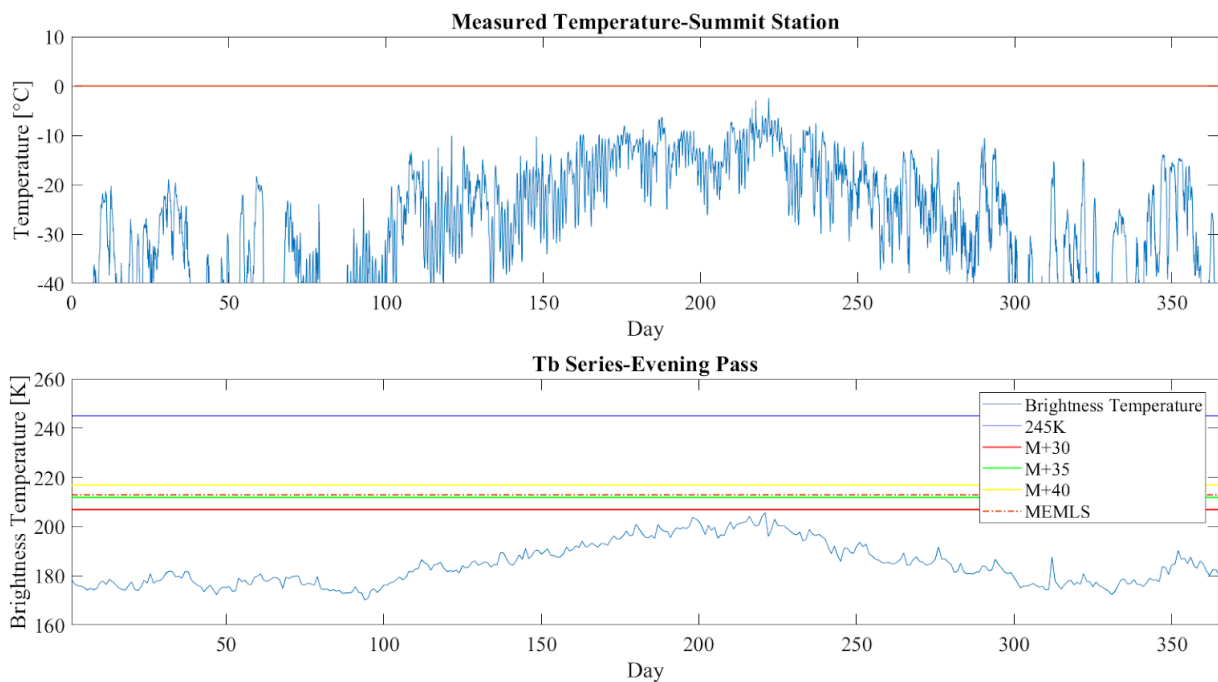


Figure 29: Timeseries of brightness temperature and air temperature at Summit, year 2001.

Assessment of selected algorithms and comparison with 25 km resolution data

In order to assess the skills of different threshold algorithms to detect melting, we compared the results obtained from the PMW data analysis with data from automatic weather station (GC Net data for Greenland and AAWSP data for Antarctica, presented previously). In the case of the AWS data, the presence of LWC within the snowpack is usually estimated from the analysis of the surface air temperature, assuming the occurrence of melting in days when $T_{\text{air}} > 0$. However, melting also occurs through radiative forcing (e.g., solar radiation) when surface temperature is still below 0°C . Moreover, the stations measure air temperature which can be different from the one within the snowpack. Therefore, we follow previous approaches in which different threshold values on the air temperature recorded by AWS are considered (Tedesco, 2009). Specifically, we consider threshold values on air temperature (T_h) ranging between 0°C and -2°C to check the possibility of melting events. The performances of the different threshold values have been evaluated by considering both cases of algorithm detecting melting when it is not occurring (commission error) and algorithm not detecting melting when it is occurring (omission error). From the surface/air temperature analysis, considering the three different thresholds (0°C , -1°C , -2°C), the number of days with surface/air temperature exceeding the thresholds are: (116,127,138) for JAR1-2004, (6,14,20) for Humboldt-2005, (75,86,94) for Swiss Camp-2013, (8,17,31) for Uranus Glacier-96/97, (14,39,67) for Larsen Ice Shelf-98/99. In the following table commission and omission errors are reported normalized with respect to the number of melting days suggested by air/surface temperature. First of all, the melt detection algorithms present better results over Greenland. For the three cases considered over Greenland, 245K threshold seems the most conservative, presenting the lowest commission error and the highest omission error. The overdetection problem is clearly visible in case of M+30, M+35 and M+40 thresholds. This problem is avoided applying MEMLS threshold, as we conjectured before. For JAR1 and Swiss Camp stations, M+30 does not present the problem of large overdetection. However, MEMLS threshold presents slightly better results considering $T_{\text{air}} = -2^{\circ}\text{C}$. In any case, 245K is the most conservative method. The missing melting days are generally in the middle of the melting season when in some days the brightness temperature drops to values below the threshold. For what concerns the cases selected for Antarctica, the comparison with surface/air temperature provides higher errors. This can be a consequence of the different data available for Antarctica, taken every ten minutes and averaged daily. Considering Uranus Glacier station, it is clear that 245K fixed threshold is not able to detect melting being too high. High overdetection

errors are suggested by considering $T_{\text{air}}=0^{\circ}\text{C}$ for both Larsen and Uranus cases. These errors strongly decrease considering $T_{\text{air}}=-1^{\circ}\text{C}$ and $T_{\text{air}}=-2^{\circ}\text{C}$. This is a consequence of the different climatic conditions in Antarctica, where strong cold winds blow resulting in lower surface/air temperature. In both cases selected for Antarctica, considering the lowest T_{air} threshold, it appears that the results obtained with M+30 are in both cases similar to the ones obtained with MEMLS. Looking at the timeseries (Figure 30b), for example, at Larsen Ice Shelf for the years 98/99 it is possible to see that the largest part of the errors are in correspondence of a drop of T_b , suggesting that the sensor could not detect the liquid water content during the melting day detected by the surface/air temperature analysis. The drop registered the day after suggests a strong change of snow properties (such as increment of grain size) following a melting/thawing event, for examples around days 81 and 137. This drop ranges between 30 K and 40 K, the same order of magnitude reported in Ulaby et al. (1996) of the difference in T_b of dry and refrozen snow at 37 GHz for horizontal polarization.

	Station	JAR 1	Swiss Camp	Humboldt	Larsen Ice Shelf	Uranus Glacier
	Year	2004	2013	2005	98/99	96/97
	$T_{\text{air}}=0$	0.07 (0.24)	0.16 (0.11)	6 (0)	1.64 (0.43)	2.5 (0.13)
M+30	$T_{\text{air}}=-1$	0.03 (0.28)	0.09 (0.17)	2.14 (0.14)	0.31 (0.51)	0.82 (0.24)
	$T_{\text{air}}=-2$	0.02 (0.33)	0.05 (0.21)	1.25 (0.15)	0.01 (0.55)	0.19 (0.32)
	$T_{\text{air}}=0$	0.07 (0.25)	0.12 (0.15)	2.67 (0)	1.36 (0.5)	1.25 (0.25)
M+35	$T_{\text{air}}=-1$	0.03 (0.28)	0.06 (0.21)	0.79 (0.21)	0.31 (0.64)	0.29 (0.35)
	$T_{\text{air}}=-2$	0.02 (0.33)	0.03 (0.26)	0.45 (0.35)	0.01 (0.63)	0 (0.48)
	$T_{\text{air}}=0$	0.07 (0.29)	0.12 (0.19)	1 (0)	0.86 (0.64)	0.38 (0.5)
M+40	$T_{\text{air}}=-1$	0.03 (0.32)	0.06 (0.24)	0.14 (0.29)	0.18 (0.59)	0.06 (0.65)
	$T_{\text{air}}=-2$	0.02 (0.37)	0.03 (0.29)	0.05 (0.45)	0 (0.75)	0 (0.77)
	$T_{\text{air}}=0$	0.09 (0.19)	0.16 (0.11)	0.67 (0.17)	2.5 (0.36)	2.5 (0.13)
MEMLS	$T_{\text{air}}=-1$	0.06 (0.23)	0.09 (0.17)	0 (0.36)	0.49 (0.36)	0.82 (0.24)
	$T_{\text{air}}=-2$	0.01 (0.28)	0.05 (0.21)	0 (0.55)	0.06 (0.4)	0.19 (0.32)
	$T_{\text{air}}=0$	0.04 (0.41)	0.08 (0.4)	0.17 (0.67)	0.57 (0.64)	0 (1)
245	$T_{\text{air}}=-1$	0.02 (0.44)	0.03 (0.42)	0 (0.79)	0.13 (0.79)	0 (1)
	$T_{\text{air}}=-2$	0.02 (0.49)	0.02 (0.48)	0 (0.85)	0 (0.81)	0 (1)

Table 5: Commission (omission) errors (normalized with respect to the number of melting days from each method) for the selected automatic weather stations in Greenland and Antarctica.

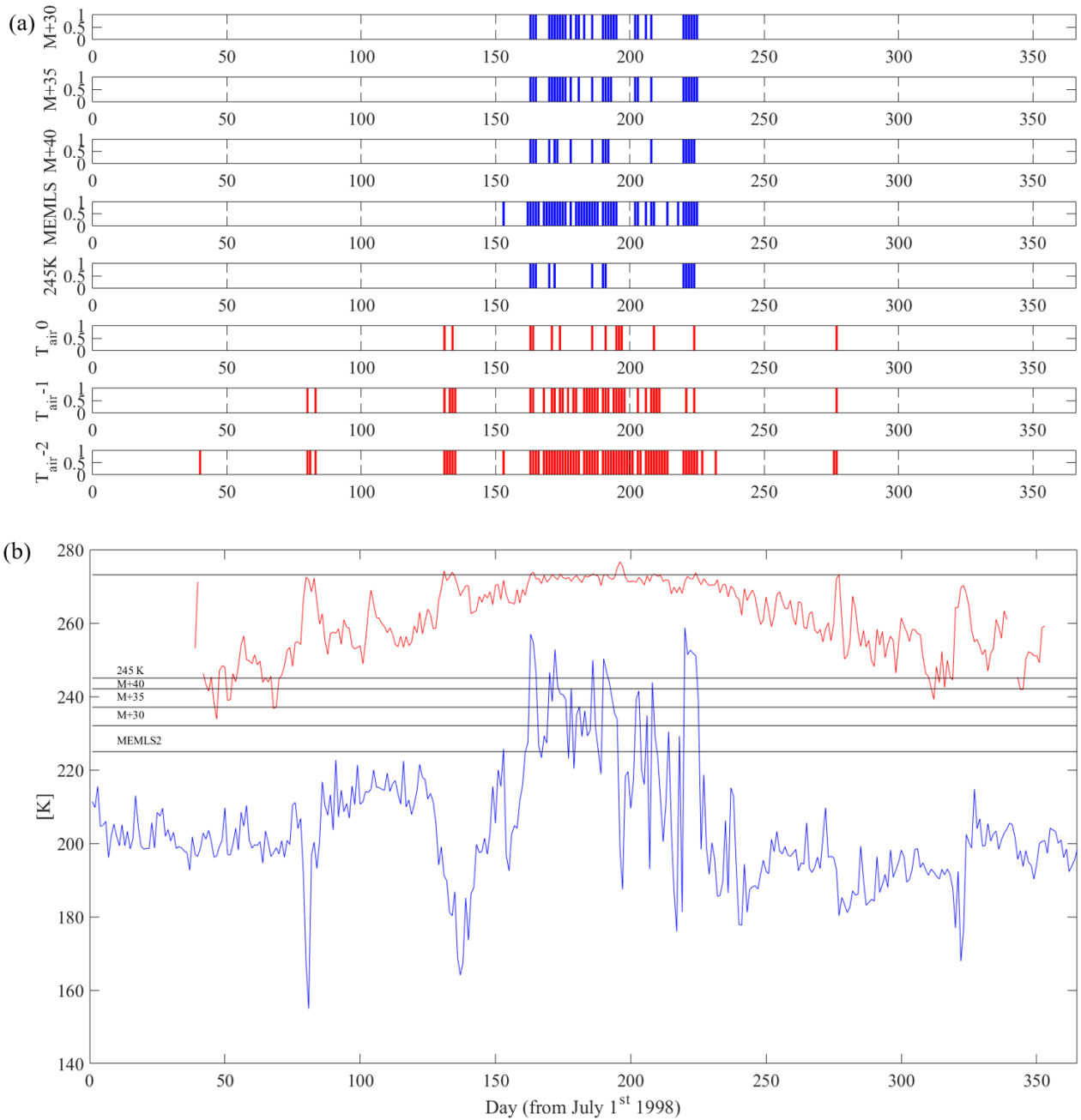


Figure 30: (a) Melting days detected by M+30, M+35, M+40, 245K and MEMLS algorithms (blue) and by surface/air temperature analysis (red). (b) Timeseries of brightness temperature (blue) and daily mean of surface/air temperature (red). The threshold values for Tb are reported as horizontal lines. Both panels (a) and (b) refers to Larsen Ice Shelf for the period July 1st, 1998-June 30th, 1999.

For what concerns the comparison between the performances of 3.125 km and 25 km resolution dataset, a similar analysis has been performed with MAR outputs. In this case, the LWC simulated into the snowpack has been vertically averaged in the first 1 m and 5 cm respectively. The threshold to identify melting days has been set equal to 0.2% for both considered depths. This value comes from the LWC value used to simulate the emission behavior

to generate the threshold called MEMLS. The analysis has been performed considering Swiss Camp site for the year 2001 evaluating the pixels containing the location of the AWS for both enhanced and coarse resolution data.

T_c	Air $T_h=0^\circ\text{C}$		Air $T_h=-1^\circ\text{C}$		Air $T_h=-2^\circ\text{C}$		LWC _{MAR} d=1m		LWC _{MAR} d=5cm	
	Comm.	Omiss.	Comm.	Omiss.	Comm.	Omiss.	Comm.	Omiss.	Comm.	Omiss.
Spatial resolution 3.125 km										
M+30	2 (2.02)	17 (17.17)	1 (0.92)	26 (23.85)	0 (0)	41 (32.8)	7 (7.78)	13 (14.44)	3 (3.09)	16 (16.49)
M+35	2 (2.02)	21 (21.21)	1 (0.92)	30 (27.52)	0 (0)	45 (36)	6 (6.67)	16 (16.78)	2 (2.06)	19 (19.59)
M+40	2 (2.02)	25 (25.25)	1 (0.92)	34 (31.19)	0 (0)	49 (39.2)	5 (5.58)	19 (21.11)	1 (1.03)	22 (22.68)
MEMLS	3 (3.03)	15 (15.15)	1 (0.92)	23 (21.1)	0 (0)	38 (30.4)	9 (10)	12 (13.33)	4 (4.12)	14 (14.43)
245K	2 (2.02)	36 (36.36)	1 (0.92)	45 (41.28)	0 (0)	60 (48)	4 (4.44)	29 (32.22)	1 (1.03)	33 (34.02)
Spatial resolution 25 km										
M+30	4 (4.04)	21 (21.21)	1 (0.92)	28 (25.69)	0 (0)	43 (34.4)	8 (8.89)	16 (17.78)	3 (3.09)	18 (18.56)
M+35	3 (3.03)	24 (24.24)	1 (0.92)	32 (29.36)	0 (0)	47 (37.6)	7 (7.78)	19 (21.11)	2 (2.06)	21 (21.65)
M+40	3 (3.03)	27 (27.27)	1 (0.92)	35 (32.11)	0 (0)	50 (40)	7 (7.78)	22 (24.44)	2 (2.06)	24 (24.74)
MEMLS	8 (8.08)	14 (14.14)	4 (3.67)	20 (18.35)	2 (1.6)	34 (27.2)	15 (16.67)	12 (13.33)	9 (9.28)	13 (13.40)
245K	2 (2.02)	45 (45.45)	1 (0.92)	54 (49.54)	0 (0)	69 (55.2)	3 (3.33)	37 (41.11)	1 (1.03)	42 (43.30)

Table 6: Commission and omission errors (as percentage with respect to the number of melting days from each method) for the comparison between coarse and enhanced resolution PMW data.

The number of melting days detected by the chosen algorithms are 84 for M+30, 80 for M+35, 76 for M+40, 65 for 245 K and 87 for MEMLS. For what concerns ground data and model outputs the melting days are 99 for $T_{air}=0^\circ\text{C}$, 109 for $T_{air}=-1^\circ\text{C}$, 125 for $T_{air}=-2^\circ\text{C}$, 90 in case of average LWC=0.2 in the first 1 m of snow and 97 in case of average LWC=0.2 in the first 5

cm of snow. From the computed commission and omission errors it is clear that the threshold of 245 K is the most conservative. In fact, it provides the lowest commission error but the highest omission, not being able to detect melt events out of the sustained melting season. Moreover, a significant number of melting days not detected by 245 K is in the middle of the melting season since T_b in some days drop to values lower than 245 K even if the snowpack is wet according to MAR outputs. Significant improvements (up to more than 9%) can be observed in this case passing from 25 km resolution to 3.125 km resolution. For what concerns M+30, in the case of SC it presents good results in terms of both low commission and omission errors and showing an improvement in representing the in-situ data. However, even if the behavior of this threshold resulted appropriate in describing melt events in this case, it still presents the over-detection problem earlier presented in cases of low winter brightness temperature. Swiss Camp example is significant because shows that, in case of M+35 and M+40, even if from Figure 27 it can be seen that the over-detection problem seems to be gradually reduced in very cold pixels, in higher T_{winter} pixels the increment in ΔT leads only to an increment of omission errors. Thus, even using a higher brightness temperature increment, these threshold values result not to be suitable to be adopted. Moreover, passing from 25 km to 3.125 km resolution the improvement is not significant. For what concerns MEMLS, it presents the lowest omission errors and low commission errors, confirming the high sensitivity of this threshold to LWC. Passing from coarse to enhanced resolution there is improvement in 4 cases, a decreased performance in 3 cases and any change in 1 case. Checking the timeseries it appears that T_{air} exceeds the threshold values selected detecting melting in winter periods but there is any presence of LWC from MAR outputs and any peak in PMW data. Hence, the omission error of all the algorithms tested with the air temperature approach are overestimated. However, there is a melting event after the main melting season detected through both AWS and MAR data but not by PMW algorithms even if it is possible to see a small peak in the timeseries, not big enough to exceed any threshold. This is a possible consequence that every threshold value applied (except 245 K) considers dry snow conditions before the melting season. Right after the melting season the brightness temperature appears to be slightly lower than January/February average, possibly because of an increment in grain size, leading to a lower emissivity. Hence, even if a $LWC > 0.2\%$ is present in the first 5 cm of snowpack and MEMLS is supposed to detect these types of melting events, MEMLS threshold is too high because it does not take into account the grain size evolution after melting. The presence of LWC, in fact, can affect emission properties of the snowpack also after refreezing or runoff, influencing the evolution of the snow grains. In addition, there is also an early melt event

detected through PMW and AWS but not through MAR. A closer look to the time series shows that in correspondence of 108th day of the year LWC reaches the value of 0.12%. This means that in some cases MEMLS algorithm can detect melting even if the LWC is lower than 0.2%, possibly because the coefficients of the algorithm come from a linear regression of the electromagnetic model outputs.

Looking at the timeseries of LWC in the first meter of snowpack obtained from MAR outputs, it is possible to distinguish between two types of melting events: (1) strictly surface melting, affecting the first few centimeters of the snowpack, and (2) in-depth melting, affecting the snowpack from the surface up to around the first meter.

According to this distinction, the vertical profiles of LWC have been averaged considering the first 5 cm and the first 1m of snowpack. The timeseries of averaged LWC have been compared with brightness temperature timeseries with the 245K and MEMLS thresholds and with the AWS temperature at Swiss Camp.

As shown in Figure (31), the threshold based on MEMLS outputs can detect melting from PMW data in conjunction with the peaks of LWC averaged on the first 5 cm and the exceedance of 273.15 K of surface temperature from AWS, showing a higher sensitivity to strictly surface melting with respect to 245 K. This is consistent with the rationale behind the development of the threshold based on MEMLS outputs. In fact, this threshold has been computed, as explained previously, looking at the presence of 0.2% of LWC.

On the contrary, the fixed threshold of 245 K appears to be highly efficient if compared with the timeseries of LWC averaged on the first meter of snowpack. In fact, 245 K is considered as the threshold above which a further increase of LWC does not lead to a further increase of brightness temperature, as it is possible to see in the central part of the timeseries. It can be concluded that this threshold value can better evaluate in-depth melting.

These results related to the vertical extension of LWC into the snowpack are consistent with the expected electromagnetic emission of the two considered cases. A snowpack in which only a surface layer of few centimeters presents LWC, even if the imaginary part of the electromagnetic permittivity increases (absorption), the real part (scattering) of the layers below is big enough to mitigate the increment of emissivity. Thus, these peaks of brightness temperature are detected by MEMLS but not by 245 K algorithm. Once LWC reaches lower layers (in-depth melting) the values of brightness temperature increase and melt is detected also by means of 245 K threshold. In fact, when liquid water is present also in deeper layers the thickness of dry snow

contributing to the scattering of the emission becomes significantly lower than the thickness of wet snow contributing to absorption.

Following these considerations, we propose with two different methodologies for melt detection over Greenland. The fixed 245 K threshold is efficient for studies related to high liquid water content and in-depth melting in the snowpack, such as hydrological analysis and studies on melting onset date (MOD), melting end date (MED) and melt duration (MD). On the other hand, the threshold from MEMLS can be adopted if the interest of the study is the analysis of strictly surface melting, as generally are early melting events and some exceptional melting events.

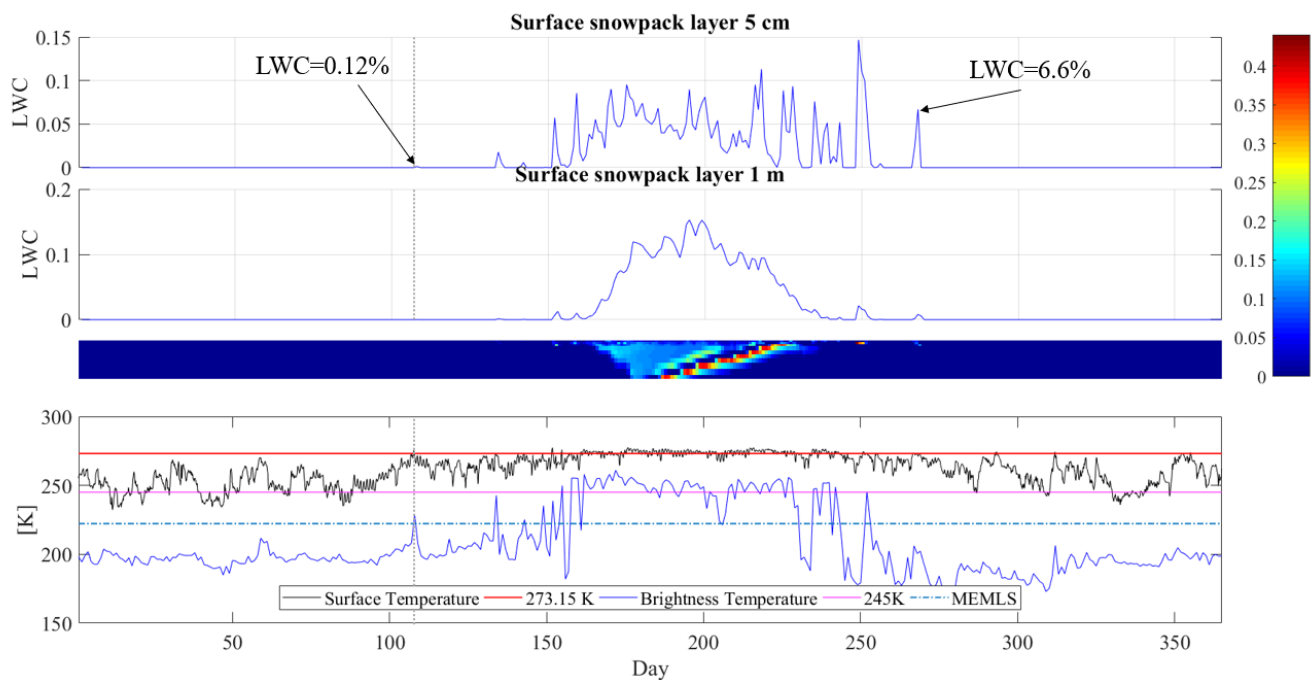


Figure 31: LWC from MAR averaged through the first layer of 5 cm and 1 m of snowpack (plots at the top), time series of the LWC profile from MAR in the first 1m of snowpack (center) and time series of 37 GHz horizontal polarization brightness temperature, air temperature from AWS and thresholds for Swiss Camp site in 2001.

5.2 Long term trend analysis

Here we present a long-term trend analysis of different melting parameters for Greenland and Antarctica cases. Trends have been evaluated along the available time period of 37 years, enough to be considered representative of changing climatic conditions.

For this purpose, some parameters representing the entity of melting have been selected. For both Greenland and Antarctica, in order to evaluate the temporal coverage of melting the melt duration

has been computed, evaluated as the sum of all the days when melting has been detected. This parameter has been computed both globally as mean melt duration (MMD), to evaluate the overall variation over the ice sheets, and at pixel scale, to identify the areas affected the most by the increment of melting days over the year. In addition to the overall mean melt duration, two others synthetic melting parameters have been evaluated following the proposed work of Torinesi et al. (2003), the maximum melting surface (MMS) and the cumulative melting surface or melting index (MI; Tedesco et. al, 2007). The former represents the maximum extent of melting area, i.e. the sum of the pixels in which melting has been detected at least once, while the latter is the sum of the melting pixel days multiplied by the area of the pixel (3.125 km * 3.125 km). Moreover, for what concerns Greenland, a new approach has been proposed following the outputs of MAR model suggesting that the occurrence of persistent melting can be well detected by 245K approach while MEMLS2 approach can identify early (or late) strictly surface melting (minor entity events). In this way melting onset day (MOD) and melting end date (MED) have been computed, respectively, considering the first two following melting days and the last melting day of the year for each pixel, using the outputs of 245K threshold. The number of melting days detected by MEMLS2 algorithm outside the temporal window of the melting season (MS=MOD-MED) has been classified as minor melt events. These parameters have been computed for every available year of the time series in order to understand whether it is possible to see a trend over the 37 years considered and quantify it. To evaluate the statistical significance of the trends computed (both pixel-by-pixel scale and synthetic indexes) the p-value has been evaluated. The p-value is defined as the probability, under the assumption of a null hypothesis H , of obtaining a result equal or higher than the observed. In practice with the evaluation of the p-value we are testing the significance level α of the hypothesis test. By fixing α equal to 0.1 (or 0.05), if $p\text{-value} < \alpha$, the test is 90% (or 95%) statistically significant. In this work we considered 95% statistically significant trends only, for both pixel-by-pixel and overall melting parameters selected.

Here an example of the code adopted for the trend calculation is presented. For the trend computation the function `polyfit` has been used while for the evaluation of the p-value the function `corrcoeff` has been adopted.

```
%% Trend analysis melt duration%%
clear all

% Load melt duration map files
addpath('D:\UNI\Tesi\Tb\MELT DURATION')
```

```
%Cicles for X and Y directions in which linear fitting of the variables is
%computed
```

```
dirList=dir(fullfile('D:\UNI\Tesi\Tb\MELT DURATION\Melt*'));
fileList=char({dirList.name});
```

```
%read mask to compute the total number of pixels
fidMaskN=fopen('D:\UNI\Tesi\Tb\Mask\EASE2_N3.125km.LO-
CI_mask_land50_coast0km.5760x5760.bin','r');
MaskN=fread(fidMaskN,[5760 5760] , 'uint8');
fclose(fidMaskN);
mask=imread('D:\UNI\Tesi\Tb\Mask\GreenlandMask.png');
MaskN(transpose(mask(:, :, 1))==0)=0;
Mask=MaskN(1901:3100,2601:3800);
```

```
trendMD245=zeros(1200,1200);
pvalMD245=zeros(1200,1200);
trendMDM30=zeros(1200,1200);
pvalMDM30=zeros(1200,1200);
trendMDM35=zeros(1200,1200);
pvalMDM35=zeros(1200,1200);
trendMDM40=zeros(1200,1200);
pvalMDM40=zeros(1200,1200);
trendMDMEMLS=zeros(1200,1200);
pvalMDMEMLS=zeros(1200,1200);
```

```
%Create cell array of variables
```

```
for i=1:37
    file=strtrim(fileList(i,:));
    load(file);

    MD_245cell(i,:)={MD_245};
    MD_Mplus30cell(i,:)={MD_mplus30};
    MD_Mplus35cell(i,:)={MD_mplus35};
    MD_Mplus40cell(i,:)={MD_mplus40};
    MD_MEMLScell(i,:)={MD_MEMLS};
end
```

```
for j=1:1200
    for k=1:1200
        if Mask(j,k)==101
            for m=1:37
                md245(m)=MD_245cell{m}(j,k);
                md30(m)=MD_Mplus30cell{m}(j,k);
                md35(m)=MD_Mplus35cell{m}(j,k);
                md40(m)=MD_Mplus40cell{m}(j,k);
                mdMEMLS(m)=MD_MEMLScell{m}(j,k);
                y(m)=m;
            end

            %linear fitting
            p245=polyfit(y,md245,1);
            pM30=polyfit(y,md30,1);
```

```

pM35=polyfit(y,md35,1);
pM40=polyfit(y,md40,1);
pMEMLS=polyfit(y,mdMEMLS,1);
%regression line
t245=y.*p245(1)+p245(2);
tM30=y.*pM30(1)+pM30(2);
tM35=y.*pM35(1)+pM35(2);
tM40=y.*pM40(1)+pM40(2);
tMEMLS=y.*pMEMLS(1)+pMEMLS(2);
%p-value
[r245,pv245]=corrcoef(md245,t245);
[rM30,pvM30]=corrcoef(md30,tM30);
[rM35,pvM35]=corrcoef(md35,tM35);
[rM40,pvM40]=corrcoef(md40,tM40);
[rMEMLS,pvMEMLS]=corrcoef(mdMEMLS,tMEMLS);

trendMD245(j,k)=p245(1);
pvalMD245(j,k)=pv245(1,2);
trendMDM30(j,k)=pM30(1);
pvalMDM30(j,k)=pvM30(1,2);
trendMDM35(j,k)=pM35(1);
pvalMDM35(j,k)=pvM35(1,2);
trendMDM40(j,k)=pM40(1);
pvalMDM40(j,k)=pvM40(1,2);
trendMDMEMLS(j,k)=pMEMLS(1);
pvalMDMEMLS(j,k)=pvMEMLS(1,2);
end
end
end

%save the outputs
save(['D:\UNI\Tesi\Tb\Trend\Trend_pvalue_MD_245_M303540_MEMLS.mat'],'trendMD
245','pvalMD245','trendMDM30','pvalMDM30','trendMDM35','pvalMDM35','trendMDM
40','pvalMDM40','trendMDMEMLS','pvalMDMEM-
LS','MD_245cell','MD_Mplus30cell','MD_Mplus35cell','MD_Mplus40cell','MD_MEM-
LScell','-v7.3');

```

Code 4

The same procedure adopted for each pixel (lines into the two `for` and the `if` statements) has been applied also for the synthetic parameters.

5.2.1 Greenland

In the case of Greenland, a general positive trend has been recorded, indicating an overall increment of the melting season. Melt duration has shown the highest statistical significance, being the most stable and reliable trend among the pixel-by-pixel parameters analyzed. It presents zero or positive trend in all pixels as can be seen in Figure, with higher values moving towards the coastline and maxima in the ablation zone. The spatial correlation with the distance of the ocean suggests that land/ocean processes influence is a major factor in surface melting events.

Moreover, the area where melt duration presented the lowest increment are the area at high altitudes. The pixel-by-pixel trends have been averaged obtaining that on average the melt duration has increased of 0.5466 days every year since 1980, with a standard deviation of 0.5033 days/year for 245K algorithm while in increased of 0.781 days/year with a standard deviation of 0.4594 days/year in case of MEMLS2 algorithm.

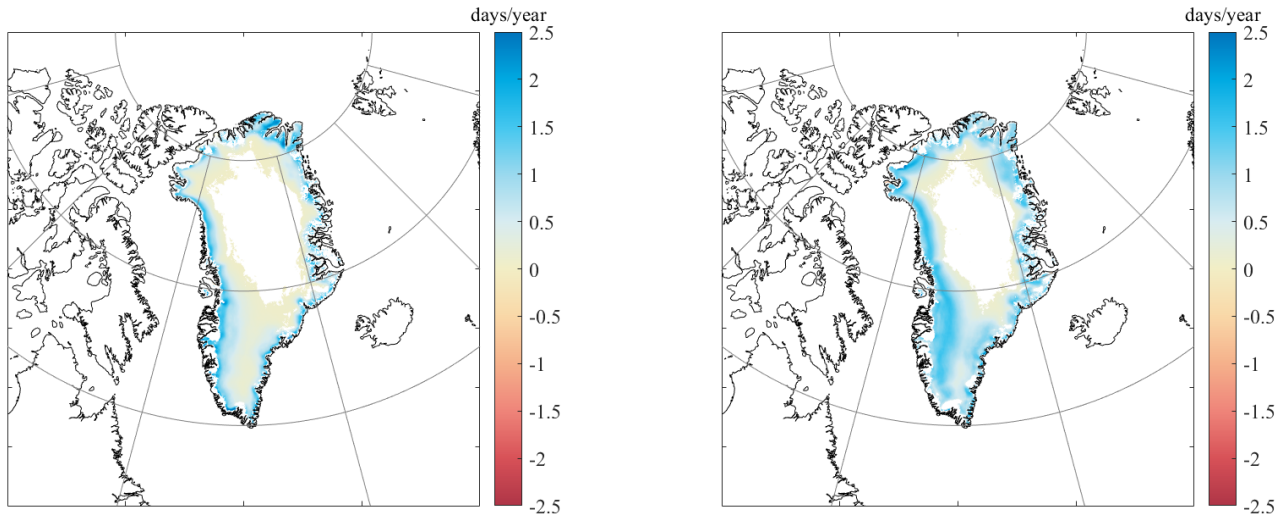


Figure 32: Maps of 95% statistically significant trends of melt duration (total number of melting days detected for each pixel) for algorithms 245 K and MEMLS2. ($\text{mean}_{\text{MD}245} = 0.5466 \text{ day/year}$, $\text{stdev}_{\text{MD}245} = 0.5033 \text{ day/year}$, $\text{mean}_{\text{MDMEMLS}} = 0.7841 \text{ day/year}$, $\text{stdev}_{\text{MDMEMLS}} = 0.4594 \text{ day/year}$).

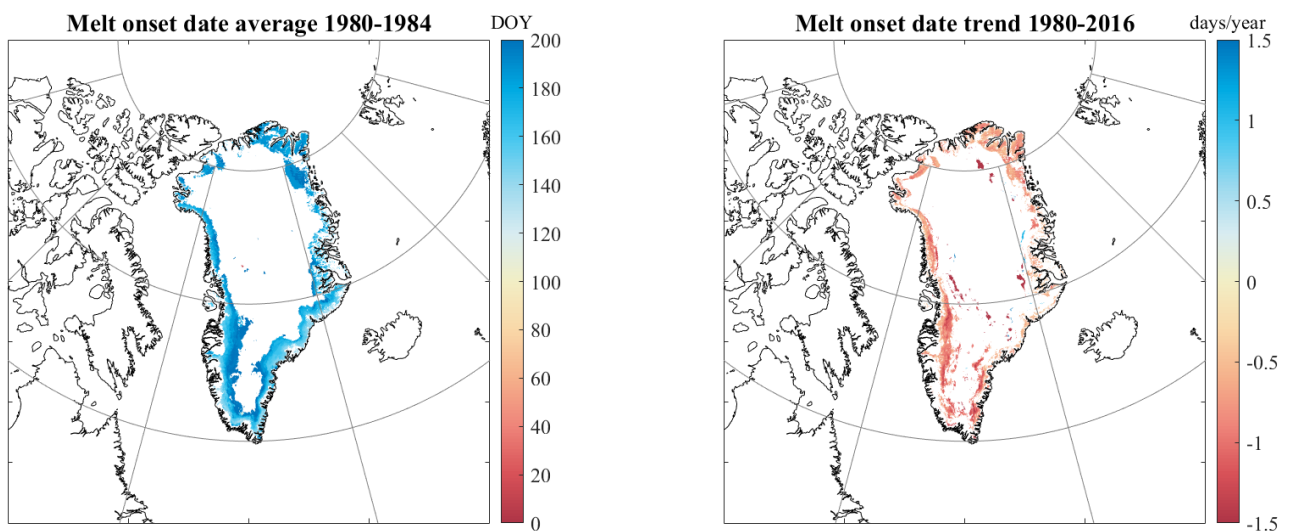


Figure 33: Maps of average melt onset date for the period 1980-1984 (MOD, left) and 95% statistically significant trends of melt onset date (right) computed following the proposed approach using 245k algorithm (statistics of the trends: $\text{mean}_{\text{MOD}} = -0.8577 \text{ day/year}$, $\text{stdev}_{\text{MOD}} = 0.5996 \text{ day/year}$).

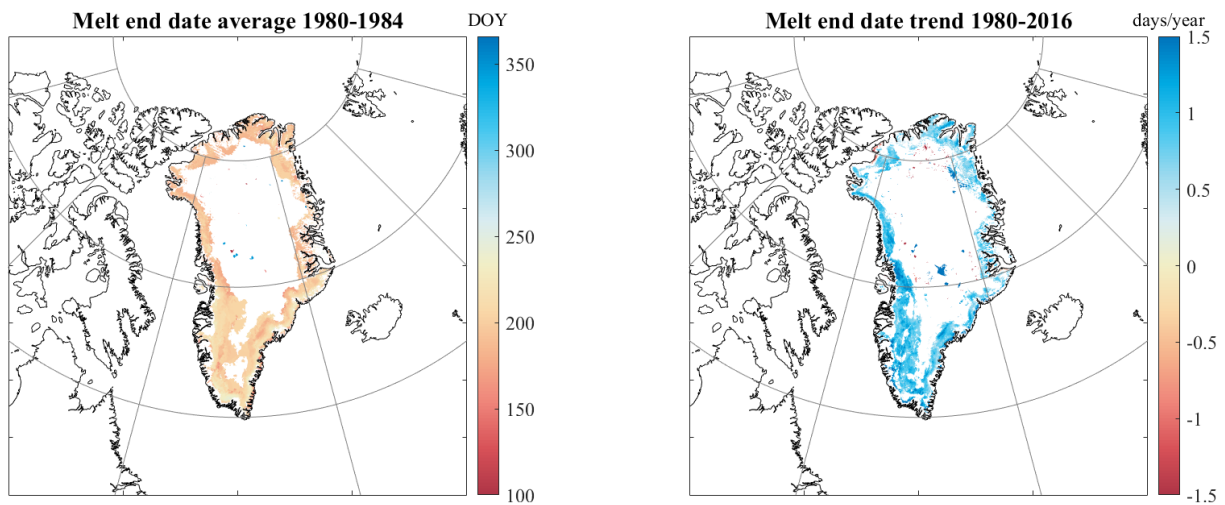


Figure 34: Maps of average melt end date for the period 1980-1984 (MED, left) and maps of 95% statistically significant trends of melt end date (right) computed following the proposed approach using 245k algorithm (trend statistics: $\text{mean}_{\text{MED}} = 0.8782$ day/year, $\text{stdev}_{\text{MED}} = 0.5677$ day/year).

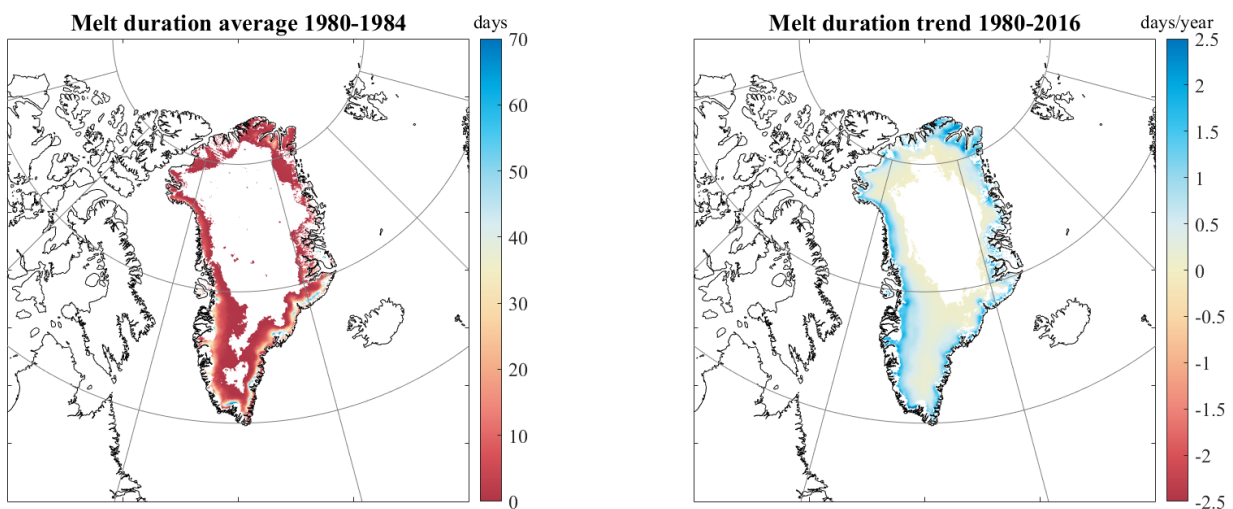


Figure 35: Maps of average melt duration for the period 1980-1984 (MOD, left) and 95% statistically significant trends of melt duration (right) computed following the proposed approach using 245k algorithm.

For what concerns melting onset and melting end dates the statistical significance reduces in areal extent. Melting onset and end date have been calculated by means of algorithm 245K according to the results presented in the previous part of this chapter. The statistically significant pixels presented a negative trend for MOD and positive for MED, with an average of melting season starting 0.8577 days earlier every year (with standard deviation of 0.5996 day/year) and ending 0.8782 day/year later (with standard deviation of 0.5677 day/year), indicating an average elongation of the melting season. Trends on melting season variable (computed as difference

between melt onset date and melt end date), as well as melt events detected before and after the melting season, present less statistically significant pixels. Nevertheless, the majority of statistically significant pixels is in the area of ablation with positive trend for melting season length, with an average of 0.3386 day/year and standard deviation 0.9342 day/year, and negative trends for melt events out of the melting season, with an average of -0.5985 day/year and standard deviation of 0.2802 day/year. This suggests that the increased average temperature recorded in the arctic in the past decades elongated the length of the melting season in Greenland, with major effects over the ablation zone (South-West Greenland, close to Swiss Camp Site and Jakobshavn Glacier). In this area, where the ice loss has been recorded as the most intensive in the period 2002-2016 from GRACE observations, the melting season is generally anticipated by some smaller melting events during day, detected by MEMLS algorithm as melting out of melting season according to the proposed approach, with snow re-freezing during night. The results obtained suggest a modification of the climatic condition with a reduction of small melting events in favor of intense melting, detected by 245K algorithm as part of the sustained melting season. According to this, isolated melting events will be shifted and recorded earlier and in periods when melting was not used to occur, as the records of last weeks prove, confirming that the occurrence of early and large melting events is increasing in Greenland ice sheet. In the next part of this chapter a case of extreme melting occurred in July 2012 will be presented.

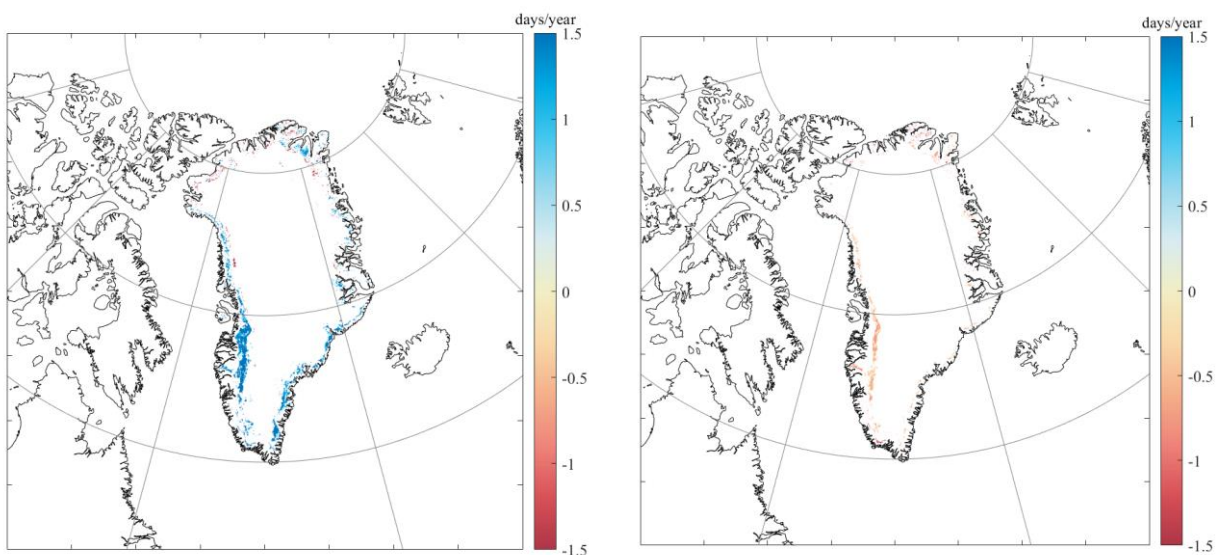


Figure 36: Maps of 95% statistically significant trends of melt season length (left; mean= 0.3386 day/year, std= 0.9342 day/year) and melt events detected out of the melting season (right; mean= -0.5985 day/year, std= 0.2802 day/year) computed following the proposed approach using 245k and MEMLS2 algorithms.

Finally, we calculate and discuss the synthetic parameters presented in Torinesi et al. (2003) and Picard & Fily (2006). For what concerns the mean melt duration (MMD) over the whole ice sheet, a positive highly statistically significant trend has been calculated according to both 245K and MEMLS algorithms with an increment of 0.34665 and 0.53903 days every year, respectively. The minimum MMD has been recorded in 1983 detecting 1.86 days on average according to 245K and 13.57 days according to MEMLS. The maximum MMD occurred in the extreme melting season of 2012, with 21.48 days for 245K and 45.75 days for MEMLS.

Also, in the case of maximum melting surface (MMS), both 245K and MEMLS algorithm detected highly statistically significant positive trends, with 20286.59 km²/year and 13647.97 km²/year, respectively. These values represent an increment of 1.19% and 0.8% every year of the total ice sheet surface. Also, for MMS the maximum has been recorded in 2012, presenting for both 245K and MEMLS algorithms a MMS equal to the 99% of the whole Greenland ice sheet. On the other hand, the minimum has been recorded in 1982, with values equal to the 20.9% of the total GrIS surface for 245K and 43.9% for MEMLS. Tedesco (2007) found that in the period 1992-2005 the maximum of MMS (TES in Tedesco's paper) is observed in 2002, while the minimum in 1994. To obtain that results, the DAV was applied to 37 GHz data at 25 km. Even if the melt detection approach is different, we use these coarser resolution results for a simple comparison with the outputs obtained with our approach for the high resolution data. For what concerns 1992, a MMS of 626425.8 km² has been recorded with 245K and 1088535 km² with MEMLS, versus 656875 km² obtained with the DAV applied to 25km*25km gridded data. It appears that 245K algorithm presents results similar to the DAV approach, with an underestimation (with respect to Tedesco) of 4.6% for 245K while MEMLS presents an increment of 65%. Considering 2002 local maximum year, MMS presents values of 1304785 km² for 245K and 1739976.6 km², versus 1555625 km² for DAV. In case of 245K the reduction in the estimation is of 16% while increase of 11.8% for MEMLS. Finally, the calculation of the melting index (MI) presents positive highly statistically significant trends, with a maximum in 2012 and a minimum in 1983.

In conclusion, surface melting has generally increased over Greenland ice sheet in the 37 years period considered, indicating a significant modification of the climatic conditions in the Arctic and possibly being a major cause of the significant mass loss recorded.

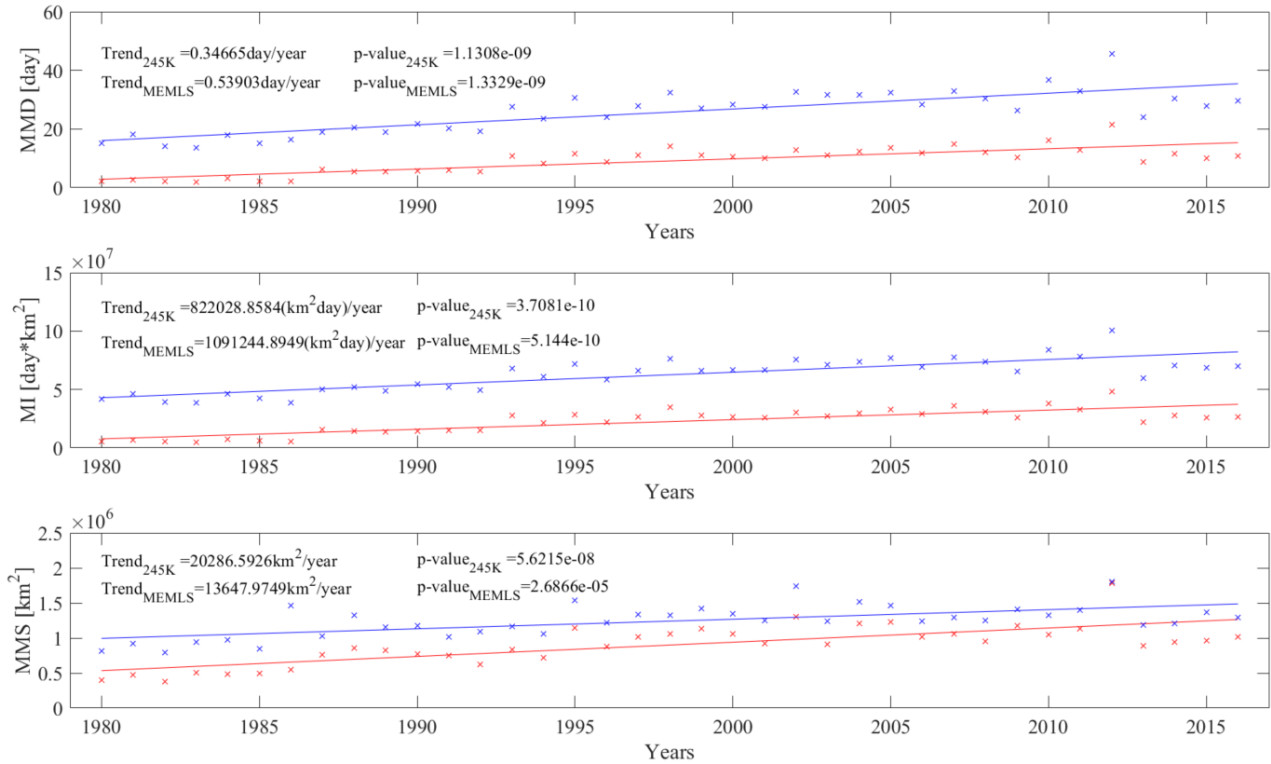


Figure 37: Statistically significant synthetic melting parameters for Greenland. Mean Melt Duration (MMD, mean number of melting days), Melting Index (MI, number of melting days times the area subjected to melting) and Maximum Melting Surface (MMS, surface that has been detected as melting at least once).

5.2.2 Antarctica

In the case of Antarctica, at pixel scale, melt duration (MD) only is presented, according to the different features and characteristics of the melting season seen at different location in the previous part of this chapter during the analysis of the local timeseries. For what concerns MMD, MI and MMS, all the three synthetic melting parameters have been computed and studied. Here the period of analysis is up to 2015-2016 Antarctic summer since 2017 data are not available completely.

At pixel scale, trends on melt duration have been firstly calculated for the time period 1980-2015, as done for Greenland. Antarctica, on the opposite to Greenland case, presents overall reduction of the melt duration at pixel scale. The 95% statistically significant trends present for the considered period a reduction of 0.2892 days every year with a standard deviation of 0.2642 in case of 245K and of 0.5228 days every year with a standard deviation of 0.3440 for MEMLS.

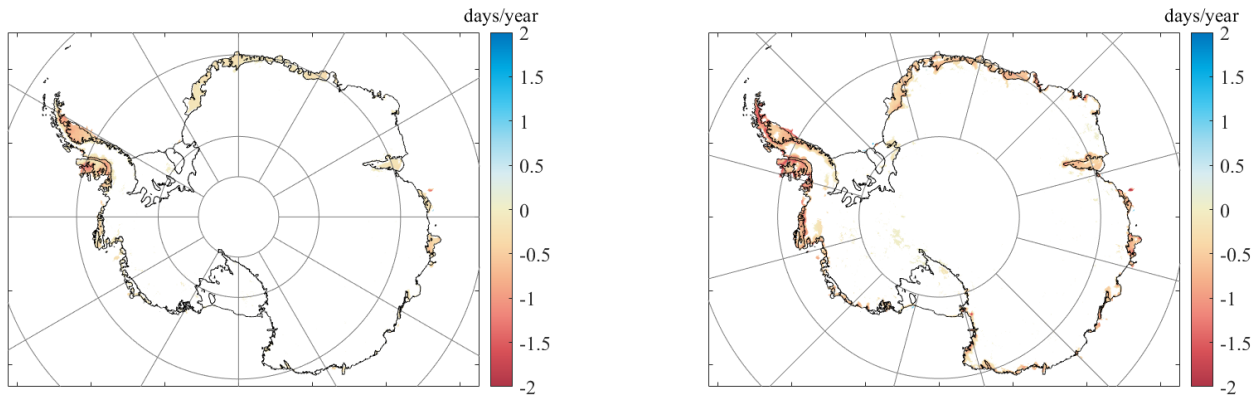


Figure 38: Antarctica melt duration trends (1980-2015) from melting maps obtained with 245K (left; mean=-0.2892 day/year, std=0.2642 day/year) and MEMLS2 (right; mean=-0.5228 day/year, std=0.3440 day/year) algorithms. All trends are negative, suggesting a reduction of melt duration.

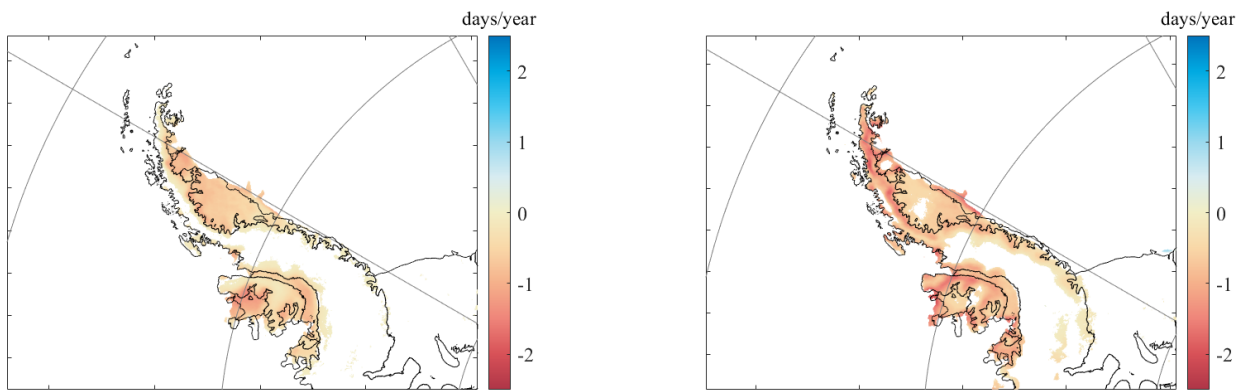


Figure 39: Melt duration trends (1980-2015) obtained over Antarctic Peninsula with 245K algorithm (left; mean=-0.4757 day/year, std= 0.3068 day/year) and MEMLS algorithm (right; mean=-0.7310 day/year, std=0.3772 day/year).

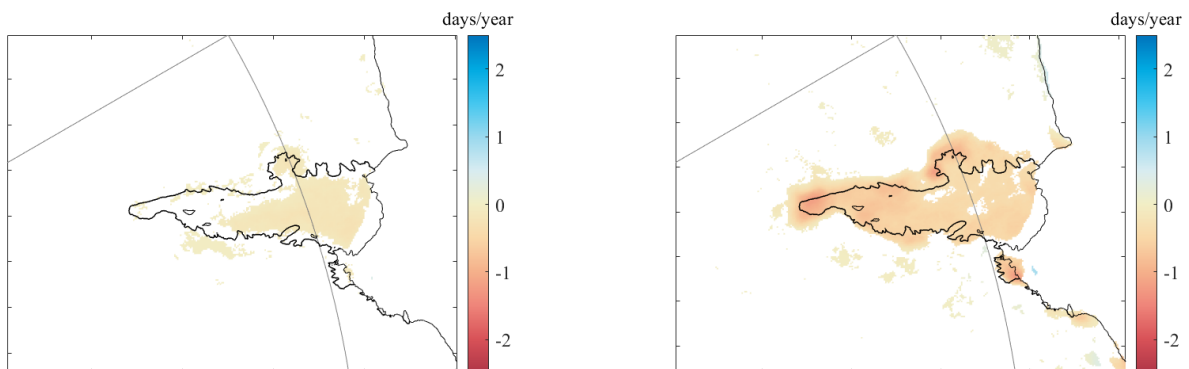


Figure 40: Melt duration trends (1980-2015) obtained over Amery ice shelf with 245K algorithm (left; mean=-0.1372day/year, std=0.0697 day/year) and MEMLS algorithm (right; mean=-0.4718 day/year, std=0.2215 day/year).

Considering the huge surface of the Antarctic ice sheet, we focused our attention on the two areas of interest shown in chapter 4: Antarctic Peninsula and the Amery ice shelf. In both cases the average of the trends obtained resulted negative, with a melt duration shortening of 0.48 and 0.14 days every year according to 245K (0.73 and 0.47 days/year for MEMLS), respectively for the Peninsula and Amery.

Since Picard & Fily (2006) suggested a possible bias coming from the use of long timeseries obtained from combination of multiple platforms, even after the consideration and the correction formula earlier presented has presented an improvement in the consistency of the timeseries, we decided to investigate MD trends considering SSM/I and SSMI/S data only, covering the period 1988-2016. The 29 years timeseries is still suitable for a long-term evaluation, being 30 years the usual temporal window considered to determine climatic conditions of a certain region. Also, by considering the reduced timeseries, negative trends are noticed. The reduction of melting season consists of 0.3522 days/year for 245K algorithm with standard deviation of 0.3505 and 0.6560 days/year for MEMLS with standard deviation of 0.5023.

In addition, we computed the synthetic melting parameters for the shortened timeseries. In case of MMD, a highly statistically significant negative trend of 0.17 years/day for 245K and 0.19 for MEMLS.

On the contrary, the MMS does not present a statistically significant trend, meaning that on average the area affected by melting has not increased or reduced.

For what concerns the variability of melting index, a statistically significant negative trend is observed. Overall negative trends are reported also by Torinesi et al. (2003) and Zwally & Fiegles (1994), highlighting the strong interannual variability. Considering the 245K algorithm, a negative trend of 1.8% every year has been found, similar value presented by Torinesi et al. in their work.

These results suggest that on the Antarctic ice sheet surface melting plays a minor role in the surface mass balance than in the case of Greenland and that it has been decreasing in the past years, maintaining a big interannual variability.

However, the uncertainties on the results over Antarctica are larger, considering that are either discordant and in accordance with the ones found in literature. In fact, even if considering different time periods, if in Torinesi et al. (2003) negative trends have been found except for the Peninsula (Figure 44), while Picard et al. (2007) found the opposite results (Figure 43a), with increasing melting all around Antarctica except for the peninsula. Also, Tedesco (2009) found results only in partial agreement with our results (Figure 43b), with the major differences on a

portion of Antarctic Peninsula. Thus, further investigation would be necessary to confirm the detected trends, by means of ice core analysis, comparison with other satellite data and surface mass balance modelling.

However, comparing the results obtained by Tedesco (2009), who adopted the same algorithms on 18.7 GHz and 19.35 GHz data, with our results it appears that the cumulative melting maps are mostly in agreement, confirming the applicability of these data to detect melting events (Figure 46).

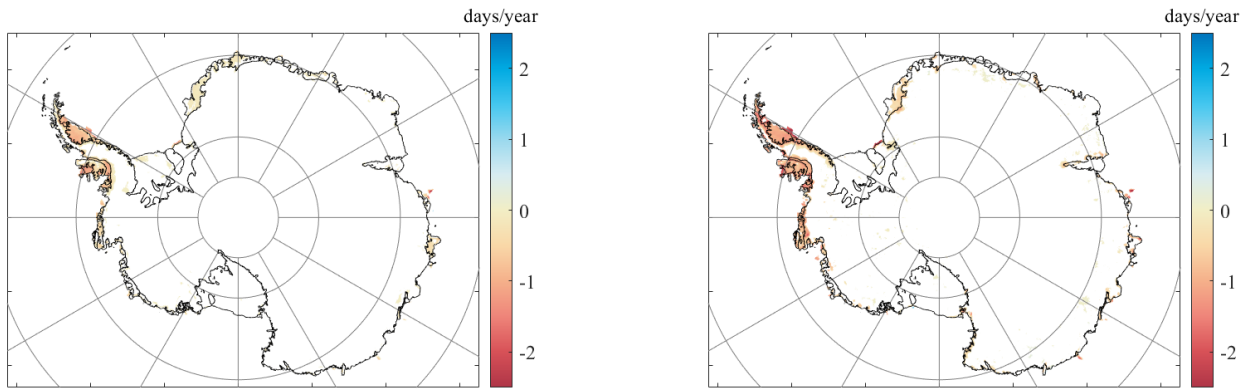


Figure 41: Melt duration trends (1988-2015) obtained over Antarctica with 245K algorithm (left; mean=-0.3522 day/year, std=0.3505 day/year) and MEMLS algorithm (right; mean=-0.6560 day/year, std=0.5023 day/year).

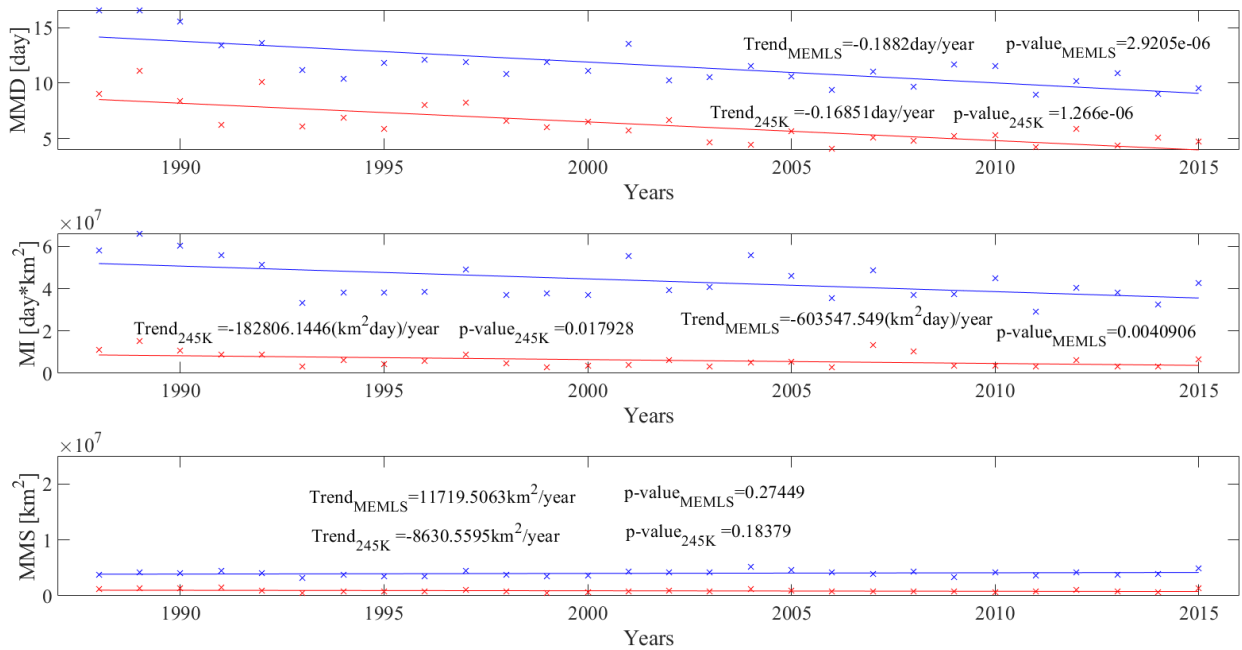


Figure 42: Synthetic melting parameters for Antarctica for the period 1988-2016. Mean Melt Duration (MMD, mean number of melting days), Melting Index (MI, number of melting days times the area subjected to melting) and Maximum Melting Surface (MMS, surface that has been detected as melting at least once).

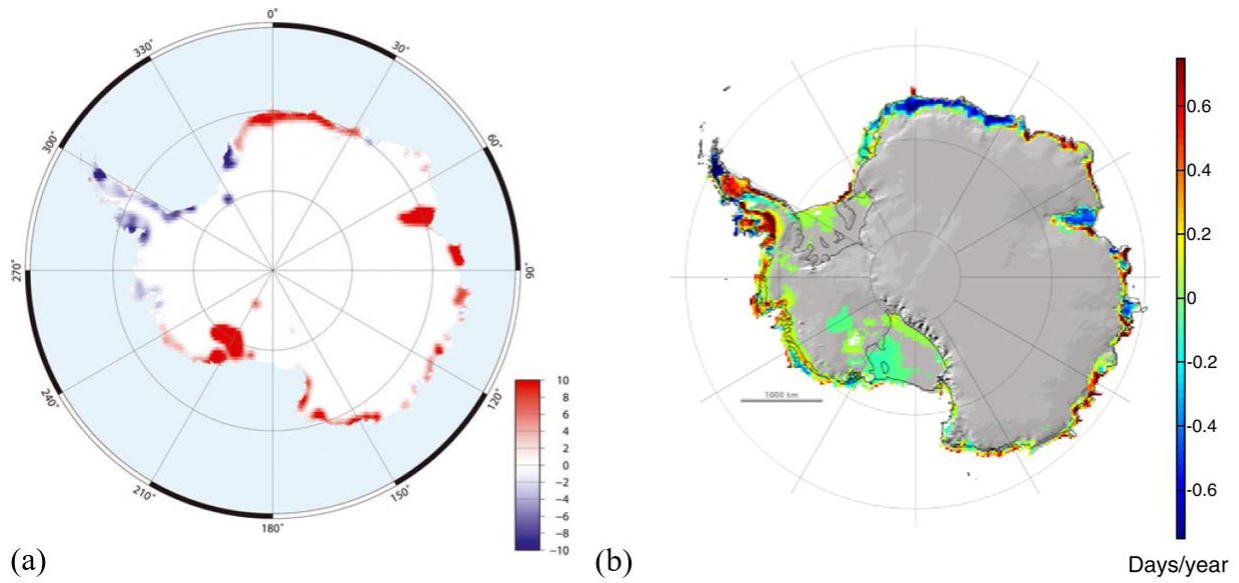


Figure 43: Results obtained by Picard et al. (2007) in panel (a) and Tedesco (2009) in panel (b) showing opposite trends for Peninsula (negative in the first and positive in the second) and the rest of Antarctica (positive in the first and negative in the second).

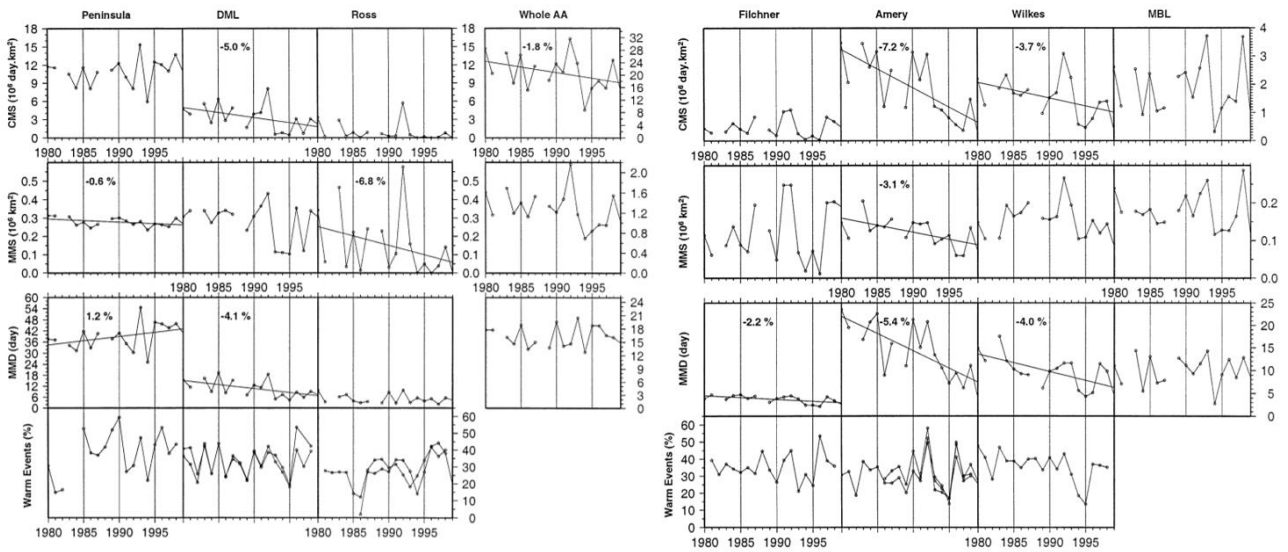
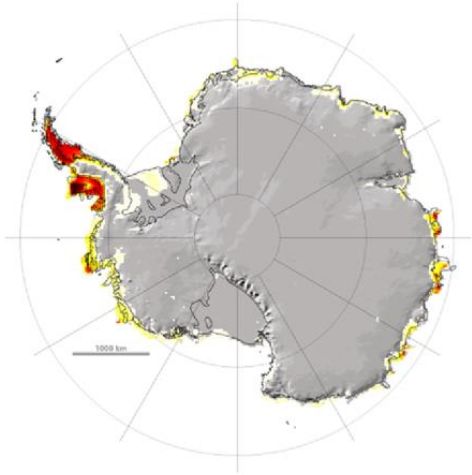
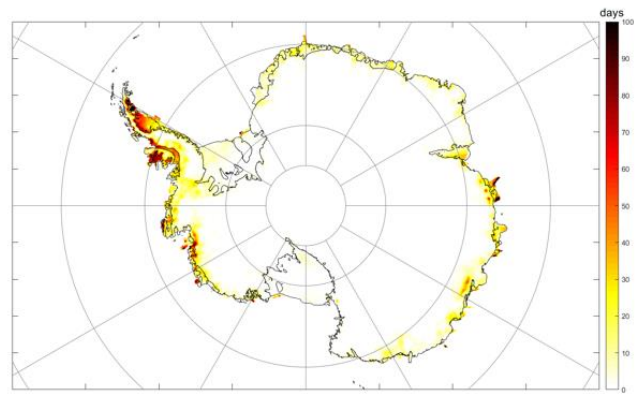


Figure 44: Results obtained by Torinesi et al. (2003). Positive values obtained on MMD of Antarctic Peninsula only.



(a)



(b)

Figure 45: Melt duration obtained by Tedesco (2009) and in this work for the summer 2008-2009.

5.3 2012: Greenland extreme melting event

Finally, we present the extreme melt event occurred across almost the whole Greenland ice sheet surface in 2012. Nghiem et al. (2012) firstly presented the satellite observation of the event, together with in situ verification from Summit station and NEEM site. Here we present the capability of the presented algorithms applied to the enhanced resolution data to map the extreme event.

The July 2012 melt event has been discovered by the scatterometer on the Indian Oceansat-2 satellite and confirmed by MODIS and SSMI/S data. In 2012, LWC has been detected over almost the entire GrIS, also in high altitude areas like Summit station, a generally dry area where snow does not undergo melting. Bennartz et al. (2013) proved the contribution of low-level liquid clouds in the enhancing melt extent. They coupled surface-based observations, remote sensing data and a surface energy balance to prove that the radiative properties of clouds made of liquid water droplets played a key part increasing the near-surface temperature. In Figure 46, melting maps created by means of MEMLS approach are presented. The selected days are the ones presented in Nghiem et al. (2012), in order to have a first qualitative comparison of the results obtained. It appears that the 3.125 km resolution maps well describe the spatial distribution of the melt events for the four days considered and it interesting to notice that MEMLS2 melting maps represents well the melting event previously mapped by means of a multisensory approach (OS2, MODIS, PMW). Our approach provides a good representation of the event using PMW data only.

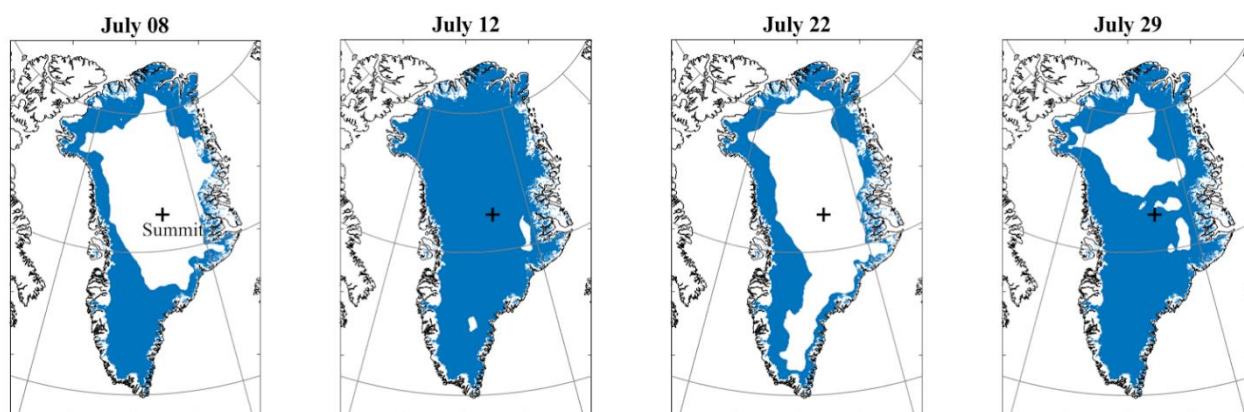


Figure 46: Melting maps of extreme event days of 2012 using MEMLS2. Summit station location is marked with the plus symbol.

On July 8th, the melt extent was according to the usual behavior of GrIS in summer melting season, covering South Greenland with a tendency to the ablation zone. On July 12th, the unprecedented melt event occurred, affecting the whole dry snow zone where melt is highly unlikely to occur. In ten days, the melted surface refroze reaching normal melt extent as shown by the map representing July 22nd. The refreezing process has however been followed by a second huge event on July 29th. This second event has not been discussed by Bennartz et al. (2013), and barely detected in Nghiem et al. (2012). As represented in the melting map, also this second event reached high altitude areas as Summit station. It is important to notice that Summit station is located at 3254 m a.s.l., and a melting event at these altitude and latitude are extremely rare, once every 150 years according to ice-core records from the same location (Buis & Cole, 2012). Considering that two strong melt events occurred, with presence of liquid water at Summit twice in less than 20 days, the melting season of 2012 represent an unprecedentedly extreme case for Greenland.

A comparison with AWS data is presented (Figure 47). It is possible to see in the brightness temperature time series that in case of July 12th (194th day of the year), both 245K and MEMLS thresholds are overcome, indicating a strong presence of liquid water at Summit, according to the surface/air temperature clearly overcoming 0 °C. After this first melt event surface temperature drops together with brightness temperature, indicating the refreezing of the water in the snowpack. Consequently, in coincidence with July 29th (211th day of the year) a second slightly weaker in magnitude but not in gradient increment of surface temperature, not reaching 0 °C and lasting for a shorter time, is accompanied by a local maxima of brightness temperature, overcoming MEMLS threshold only. As discussed earlier in this chapter, melt can occur even if surface temperature does not overcome the 0 °C threshold, being the energy balance of snow influenced by other factors. The July 29th second melt event shows the characteristics of what we called strictly surface melting, indicating the presence of liquid water in smaller amount and a melt event of weaker entity. The smaller strength of the second melt event is confirmed also by the fact that the melt extent is reduced with respect to July 12th and indicates that the presence of liquid water at Summit does not indicate the total extension of melting over the GrIS.

The 3.125 km passive microwave brightness temperature at 37 GHz (horizontal polarization) capability in detecting extreme melting events has been proved, observing a good match with in-situ data, being the smaller pixel more representative of the point location. The two large melt events occurred in 2012 have been confirmed by our analysis, showing the goodness of the melting maps produced also in case of extreme events.

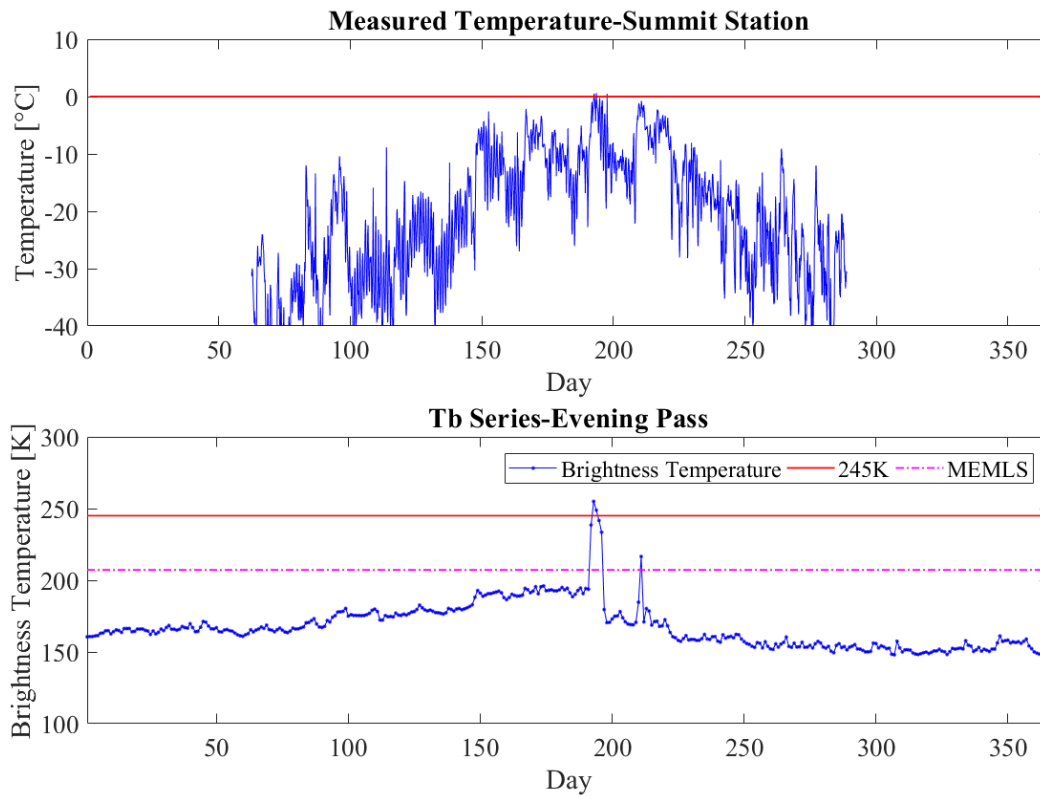


Figure 47: Timeseries of air temperature (at top) and brightness temperature (at bottom) recorded at Summit for year 2012. It is possible to see the main melt event of July 12th (characterized by positive air temperature) detected by 245K and MEMLS2 algorithms.

6 Conclusions

In this work the surface melting over Greenland and Antarctica ice sheets has been analyzed by means of a recently available passive microwave brightness temperatures dataset at the enhanced spatial resolution of 3.125 km.

First, in order to create the first and longest available timeseries of passive microwave brightness temperature at this resolution, the intercomparison of data from different satellites covering the time period of 37 years (1980-2016) has been performed. The results obtained showed the necessity of intercalibration equations to merge SMMR (1980-1987) and SMM/I (1987-now) data. These linear relations have been computed, applied to the data and tested showing an increment of consistency between the two sets of data.

Second, the brightness temperature data availability has been discussed. Since the first part of the dataset (SMMR data) are collected once every two days and considering that there are some missing data, we decided to perform interpolation over the ice sheet (area of our interest for this work, applying a LOCI mask). An algorithm has been written, creating a file containing two cell arrays of the interpolated brightness temperature, two maps containing the values of winter brightness temperature averages and two cell array containing, for each pixel, a vector indicating the temporal position of the interpolated values to keep track of the estimated data.

Third, the complete 37 years dataset has been used to study surface melting over Greenland and Antarctica ice sheet. Five algorithms has been applied to map surface melting, selected from literature. The performances these algorithms have been tested by means of automatic weather station data and a comparison with coarse resolution data has been done using also the outputs of a regional climate model (MAR). It resulted that the enhanced resolution data show lower errors than the coarse resolution for both ASW and MAR data and that, among the algorithms selected, 245K and MEMLS present the lower “overdetection” errors. The first, 245K, is the most conservative and resulted suitable to detect sustained melting; on the other hand MEMLS, designed to detect small amount of liquid water in the snowpack (0.2%) appears to be able to detect not only the sustained melting season but also early and late minor melt events. Better performances of MEMLS has been shown in Greenland than in Antarctica, suggesting the possibility of a multi-algorithm approach in order to detect the sustained melt onset and end date together with the days of melting occurring in a sporadic way before and after the melting season,

applied in the last chapter for Greenland. Then, the dataset of melting maps at 3.125 km resolution have been created for the period 1980-2016, for both Greenland and Antarctica.

After the creation of the dataset, the melting maps have been used to study variability and changes in surface melting seasons. For what concerns Greenland, from the analysis of synthetic melting parameters it resulted that the mean melt duration (MMD) has increased in the past 37 years of 0.35 to 0.54 days per year, that the cumulative melting surface (melt index, MI) increased of 1.8% every year (normalized with respect to the first year considered, 0.13% if normalized over the whole Greenland ice sheet and 365 days) and that the maximum melting surface increased of values between 0.17% and 1.19% every year according to the algorithm selected. The melt onset date occurred 0.86 days earlier while the melt end date occurred 0.87 days later every year on average (considering the only statistically significant trends). The number of sporadic melting days shows a negative trend, suggesting that the sporadic melting anticipating the sustained melting season slowly became part of it. Generally, in Greenland melting has increased in the past decades in both duration and surface extension. In the case of Antarctica, generally negative trends have been recorded for all the observed parameters, except in the case of maximum melting surface presenting any statistically significant trend. Our results are partially consistent with works found in literature, being both in agreement and disagreement according to the paper selected as comparison. Further investigations are necessary to understand the real behavior of surface melting in Antarctica, comparing data from different satellites, ice core data and model outputs. However, it does not void the shown capability of these algorithms and dataset in mapping melting.

Finally, the 2012 melting season has been presented and discussed, showing the capability of MEMLS algorithm to confirm the presence of liquid water at Summit station not only on July 12th, but also on July 29th.

References of section 3

Abdalati, W., & Steffen, K. (1995). Passive microwave-derived snow melt regions on the Greenland ice sheet. *Geophysical Research Letters*, 22(7), 787-790.

Alexander, P. M., M. Tedesco, X. Fettweis, R. Van De Wal, C.J.P.P. Smeets, and M.R. Van Den Broeke, 2014: Assessing spatio-temporal variability and trends in modelled and measured Greenland Ice Sheet albedo (2000–2013). *The Cryosphere*, 8, 2293–2312, doi: 10.5194/tc-8-293-2014.

Ashcraft, I. S., & Long, D. G. (2006). Comparison of methods for melt detection over Greenland using active and passive microwave measurements. *International Journal of Remote Sensing*, 27(12), 2469-2488.

Armstrong, R., K. Knowles, M. Brodzik and M. A. Hardman. 1994, updated current year. DMSP SSM/I-SSMIS Pathfinder Daily EASE-Grid Brightness Temperatures. Version 2. Boulder, Colorado USA: NASA DAAC at the National Snow and Ice Data Center.

Ballinger, T. J., Mote, T. L., Mattingly, K., Bliss, A. C., Hanna, E., van As, D., Prieto, M., Gharehchahi, S., Fettweis, X., Noël, B., Smeets, P. C. J. P., Ribergaard, M. H., and Cappelen, J.: Greenland Ice Sheet late-season melt: Investigating multi-scale drivers of K-transect events, *The Cryosphere Discuss.*, <https://doi.org/10.5194/tc-2018-285>, in review, 2019.

Brodzik, M. J. and K. W. Knowles. 2002. “EASE-Grid: a versatile set of equal-area projections and grids” in M. Goodchild (Ed.) *Discrete Global Grids*. National Center for Geographic Information & Analysis, Santa Barbara, CA: USA.

Brodzik, M. J., B. Billingsley, T. Haran, B. Raup and M. H. Savoie. 2012. EASE-Grid 2.0: Incremental but Significant Improvements for Earth-Gridded Data Sets. *ISPRS Int. J. Geo-Inf.*, 1:32–45. doi: 10.3390/ijgi101003.

Brodzik, M. J., Long, D. G., Hardman, M. A., Paget, A., & Armstrong, R. L. MEaSURES Calibrated Enhanced-Resolution Passive Microwave Daily EASE-Grid 2.0 Brightness Temperature ESDR, Version 1; National Snow and Ice Data Center: Boulder, CO, USA, 2016. Updated 2018. Digital Media. Available online: <http://nsidc.org/data/nsidc-0630> (accessed on 7 November 2018).

Brun, E., David, P., Sudul, M., & Brunot, G. (1992). A numerical model to simulate snow-cover stratigraphy for operational avalanche forecasting. *Journal of Glaciology*, 38(128), 13-22.

- Buis, A., & Cole, S. (2012). Satellites see unprecedented greenland ice sheet melt. NASA/JPL press release, 24, 2012-217.
- Dee, D. P., Uppala, S. M., Simmons, A. J., Berrisford, P., Poli, P., Kobayashi, S., ... & Bechtold, P. (2011). The ERA-Interim reanalysis: Configuration and performance of the data assimilation system. *Quarterly Journal of the royal meteorological society*, 137(656), 553-597.
- Farrar, M. R., & Smith, E. A. (1992). Spatial resolution enhancement of terrestrial features using deconvolved SSM/I microwave brightness temperatures. *IEEE Transactions on Geoscience and Remote Sensing*, 30(2), 349-355.
- Fettweis, X., Gallée, H., Lefebvre, F., & Van Ypersele, J. P. (2005). Greenland surface mass balance simulated by a regional climate model and comparison with satellite-derived data in 1990–1991. *Climate Dynamics*, 24(6), 623-640.
- Fettweis, X., Tedesco, M., Van de Broeke, M. R., & Ettema, J. (2011). Melting trends over the Greenland ice sheet (1958–2009) from spaceborne microwave data and regional climate models. *The Cryosphere*, 5(2), 359-375.
- Fettweis, X., Box, J., Agosta, C., Amory, C., Kittel, C., Lang, C., ... & Gallée, H. (2017). Reconstructions of the 1900–2015 Greenland ice sheet surface mass balance using the regional climate MAR model. *Cryosphere (The)*, 11, 1015-1033.
- Knowles, K. E., Njoku, G., Armstrong, R., & Brodzik, M. (2000). Nimbus-7 SMMR Pathfinder Daily EASE-Grid Brightness Temperatures, version 1. NASA National Snow Ice Data Center Distributed Active Archive Center: Boulder, CO, USA.
- Knowles, K., M. Savoie, R. Armstrong and M. Brodzik. 2006. AMSR-E/Aqua Daily EASE-Grid Brightness Temperatures. Boulder, Colorado USA: NASA DAAC at the National Snow and Ice Data Center.
- Picard, G., & Fily, M. (2006). Surface melting observations in Antarctica by microwave radiometers: Correcting 26-year time series from changes in acquisition hours. *Remote sensing of environment*, 104(3), 325-336.
- Picard, G., Fily, M., & Gallée, H. (2007). Surface melting derived from microwave radiometers: a climatic indicator in Antarctica. *Annals of Glaciology*, 46, 29-34.
- Ramage, J. M., & Isacks, B. L. (2002). Determination of melt-onset and refreeze timing on southeast Alaskan icefields using SSM/I diurnal amplitude variations. *Annals of Glaciology*, 34, 391-398.

Steffen, K., Abdalati, W., & Stroeve, J. (1993). Climate sensitivity studies of the Greenland ice sheet using satellite AVHRR, SMMR, SSM/I and in situ data. *Meteorology and Atmospheric Physics*, 51(3-4), 239-258.

Steffen, K., Box, J. E., & Abdalati, W. A. L. E. D. (1996). Greenland climate network: GC-Net. US Army Cold Regions Reattach and Engineering (CRREL), CRREL Special Report, 98-103.

Steiner, N., & Tedesco, M. (2014). A Wavelet Melt Detection Algorithm Applied to Enhanced Resolution Scatterometer Data over Antarctica (2000-2009).

Tedesco, M., Abdalati, W., & Zwally, H. J. (2007). Persistent surface snowmelt over Antarctica (1987–2006) from 19.35 GHz brightness temperatures. *Geophysical Research Letters*, 34(18).

Tedesco, M. (2007). Snowmelt detection over the Greenland ice sheet from SSM/I brightness temperature daily variations. *Geophysical Research Letters*, 34(2).

Tedesco, M., Serreze, M., & Fettweis, X. (2008). Diagnosing the extreme surface melt event over southwestern Greenland in 2007. *The Cryosphere Discussions*, 2(3), 383-397.

Tedesco, M. (2009). Assessment and development of snowmelt retrieval algorithms over Antarctica from K-band spaceborne brightness temperature (1979–2008). *Remote Sensing of Environment*, 113(5), 979-997.

Tedesco, M., Brodzik, M., Armstrong, R., Savoie, M., & Ramage, J. (2009). Pan arctic terrestrial snowmelt trends (1979–2008) from spaceborne passive microwave data and correlation with the Arctic Oscillation. *Geophysical Research Letters*, 36(21).

Tedesco, M. (2014). *Remote sensing of the cryosphere*. John Wiley & Sons.

Torinesi, O., Fily, M., & Genthon, C. (2003). Variability and trends of the summer melt period of Antarctic ice margins since 1980 from microwave sensors. *Journal of Climate*, 16(7), 1047-1060.

Ulaby, F. T., Moore, R. K., & Fung, A. K. (1986). *Microwave remote sensing: Active and passive. Volume 3-From theory to applications*.

van den Broeke, M. (2005). Strong surface melting preceded collapse of Antarctic Peninsula ice shelf. *Geophysical Research Letters*, 32(12).

Wang, S., Tedesco, M., Xu, M., & Alexander, P. M. (2018). Mapping Ice Algal Blooms in Southwest Greenland From Space. *Geophysical Research Letters*, 45(21), 11-779.

Wiesmann, A., & Mätzler, C. (1999). Microwave emission model of layered snowpacks. *Remote Sensing of Environment*, 70(3), 307-316.

Zwally, H. J., & Fiegles, S. (1994). Extent and duration of Antarctic surface melting. *Journal of Glaciology*, 40(136), 463-475.

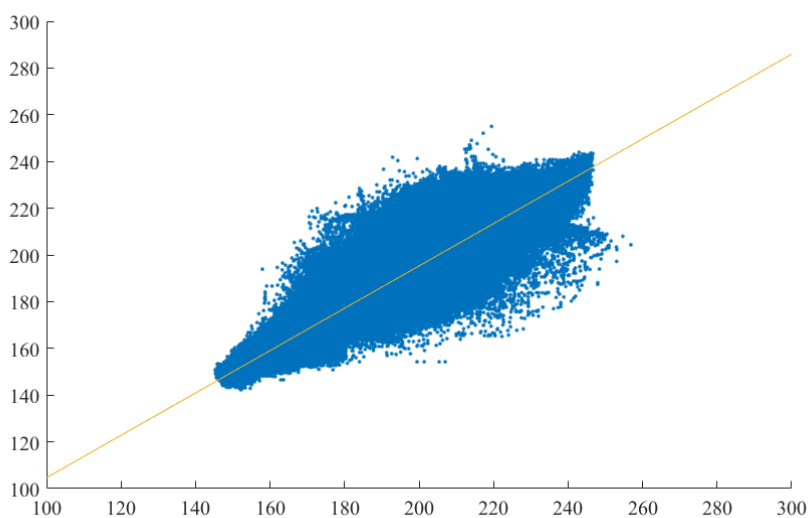
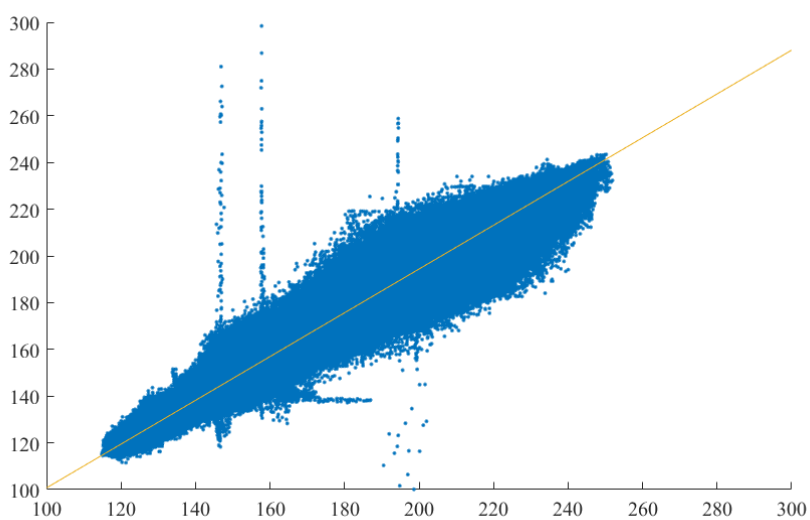
Zwally, H. J., Abdalati, W., Herring, T., Larson, K., Saba, J., & Steffen, K. (2002). Surface melt-induced acceleration of Greenland ice-sheet flow. *Science*, 297(5579), 218-222.

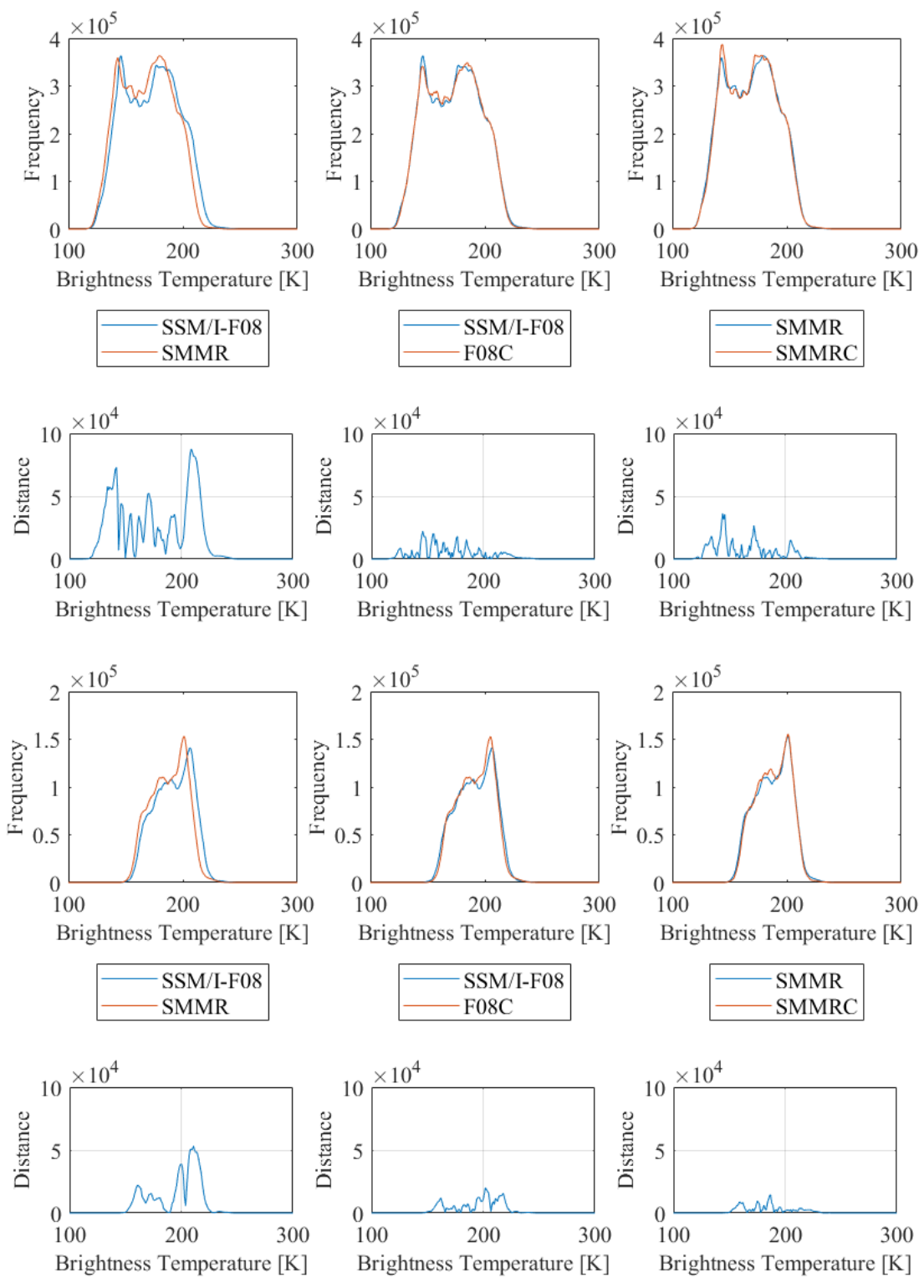
Appendix

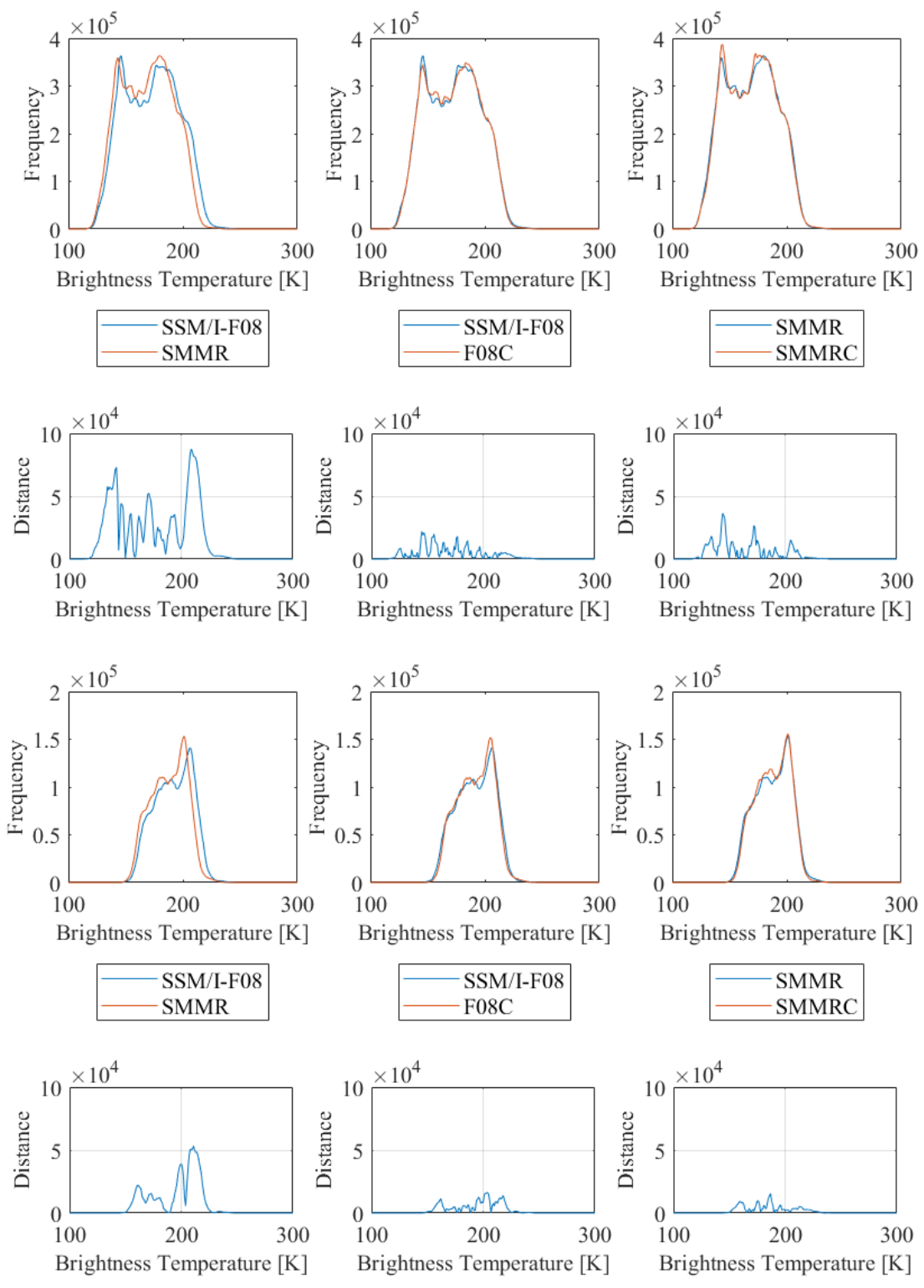
Antarctica

X=F08	m_1	m_2	q_1	q_2	R^2_2	d_1	d_2
Morning	0.9108	0.9062	13.2273	14.0605	0.9115	0.7414	0.7686
Evening	0.9368	0.9368	7.0417	7.0492	0.9796	0.3829	0.7728

X=SMMR	m_1	m_2	q_1	q_2	R^2_2	d_1	d_2
Morning	0.9991	1.0059	4.0517	2.8712	0.9115	0.6225	0.6633
Evening	1.0455	1.0457	-3.7954	-3.8374	0.9796	0.8138	0.8168



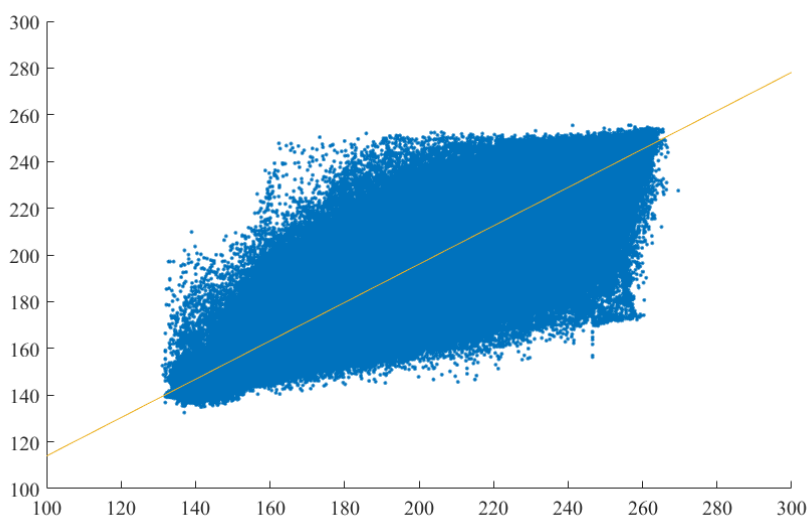
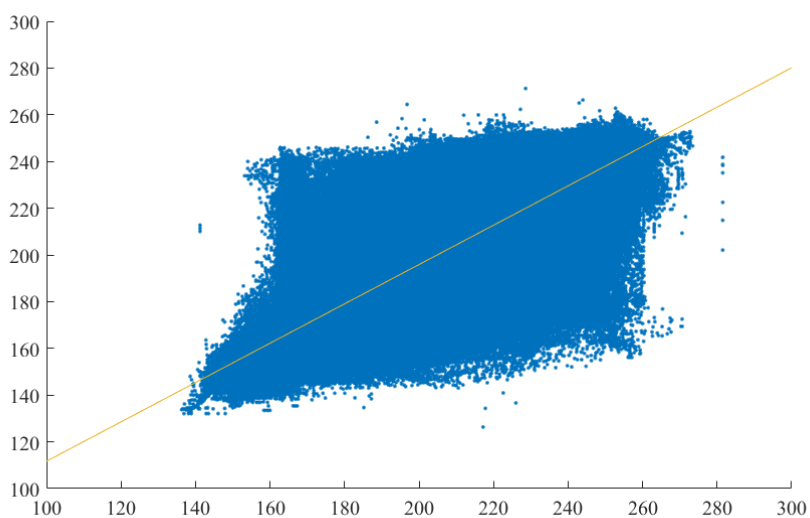


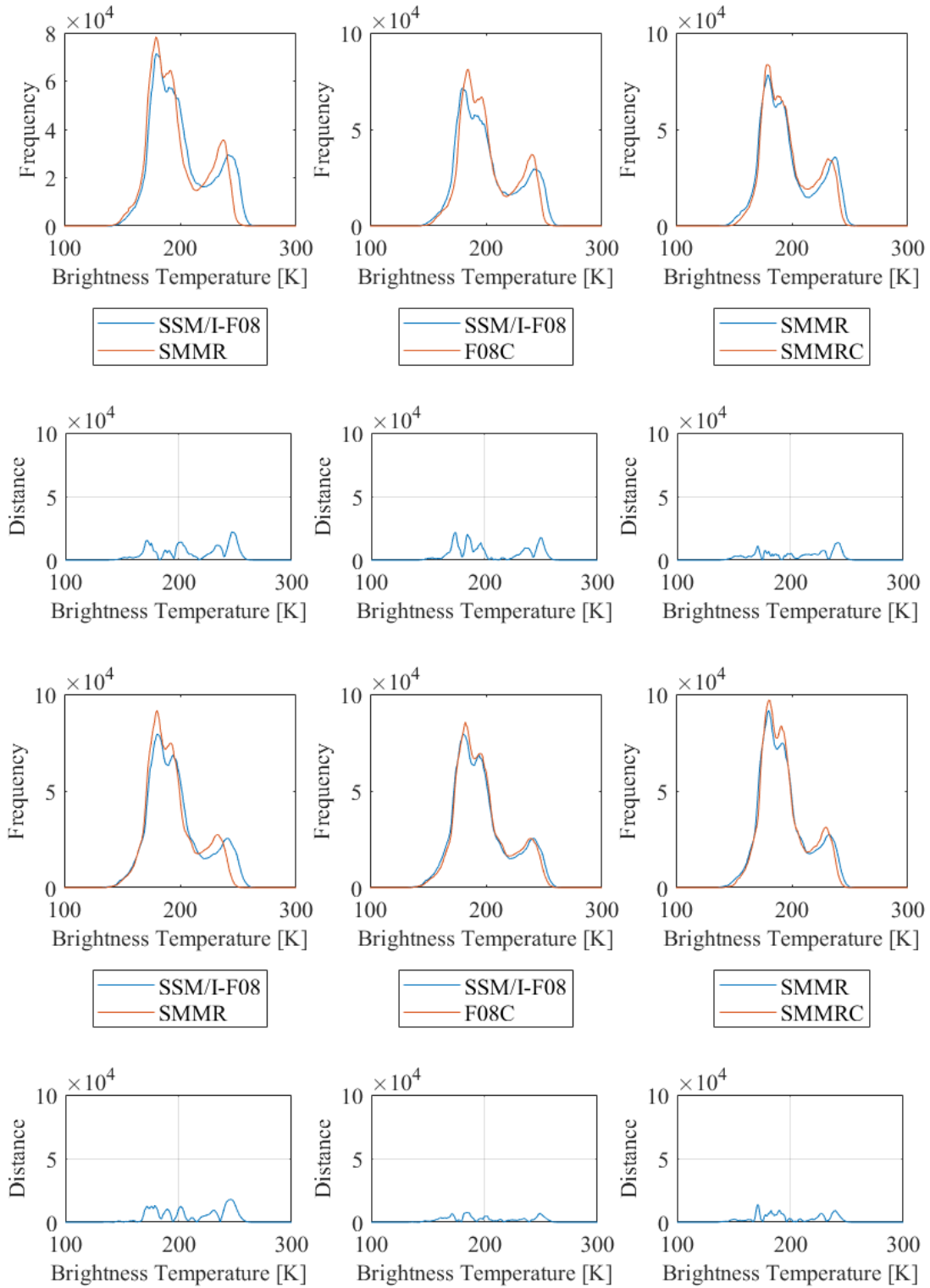


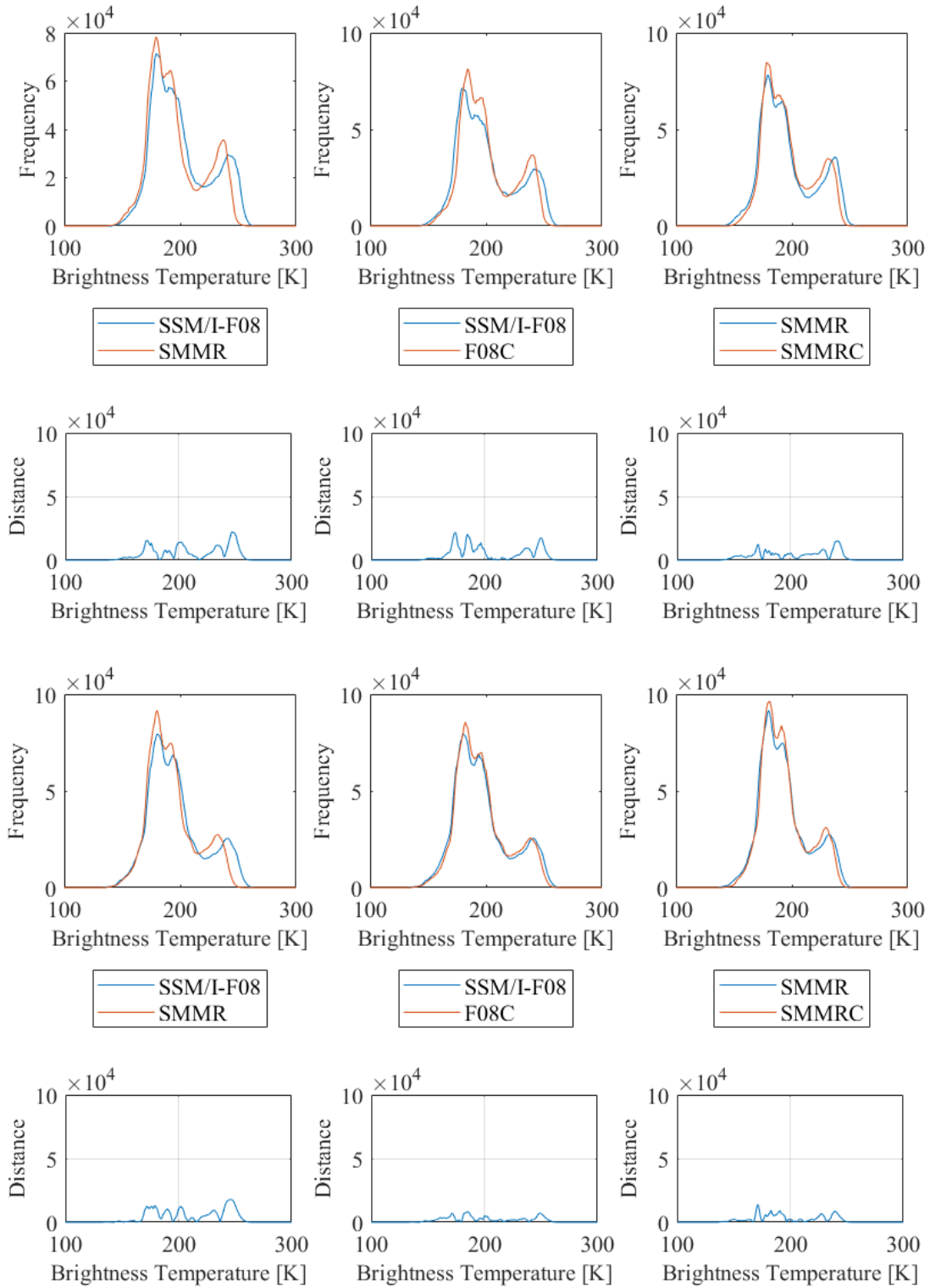
Greenland

X=F08	m ₁	m ₂	q ₁	q ₂	R ² ₂	d ₁	d ₂
Morning	0.818	0.821	32.3868	31.8562	0.8803	0.6865	0.4616
Evening	0.8494	0.8419	26.0269	27.5114	0.8127	0.1204	0.3316

X=SMMR	m ₁	m ₂	q ₁	q ₂	R ² ₂	d ₁	d ₂
Morning	1.0753	1.0722	-11.1399	-10.5807	0.8803	0.557	0.5157
Evening	0.9635	0.9653	11.4237	11.1226	0.8127	0.0937	0.1227



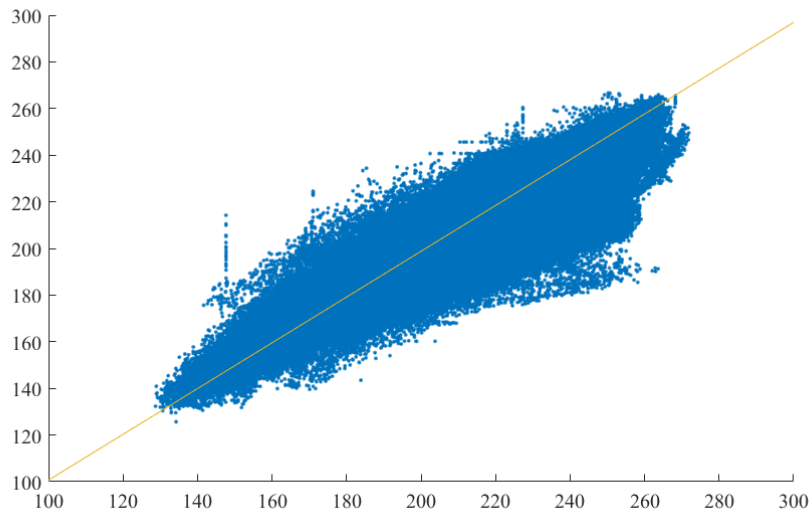
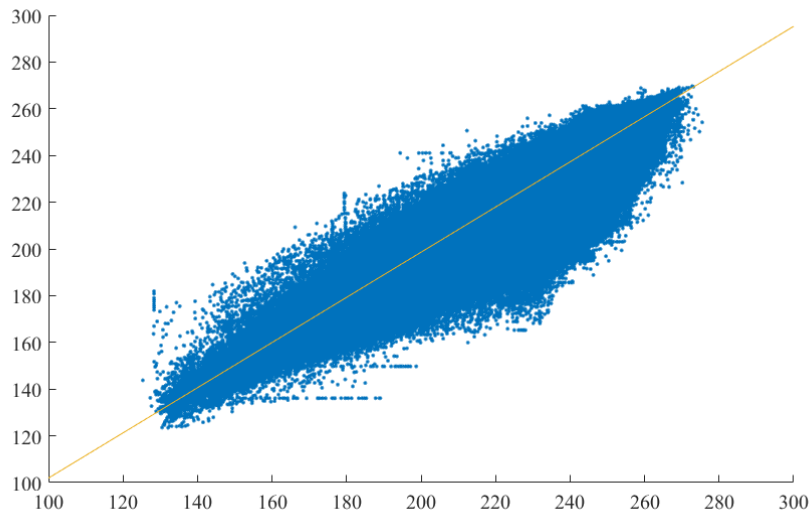


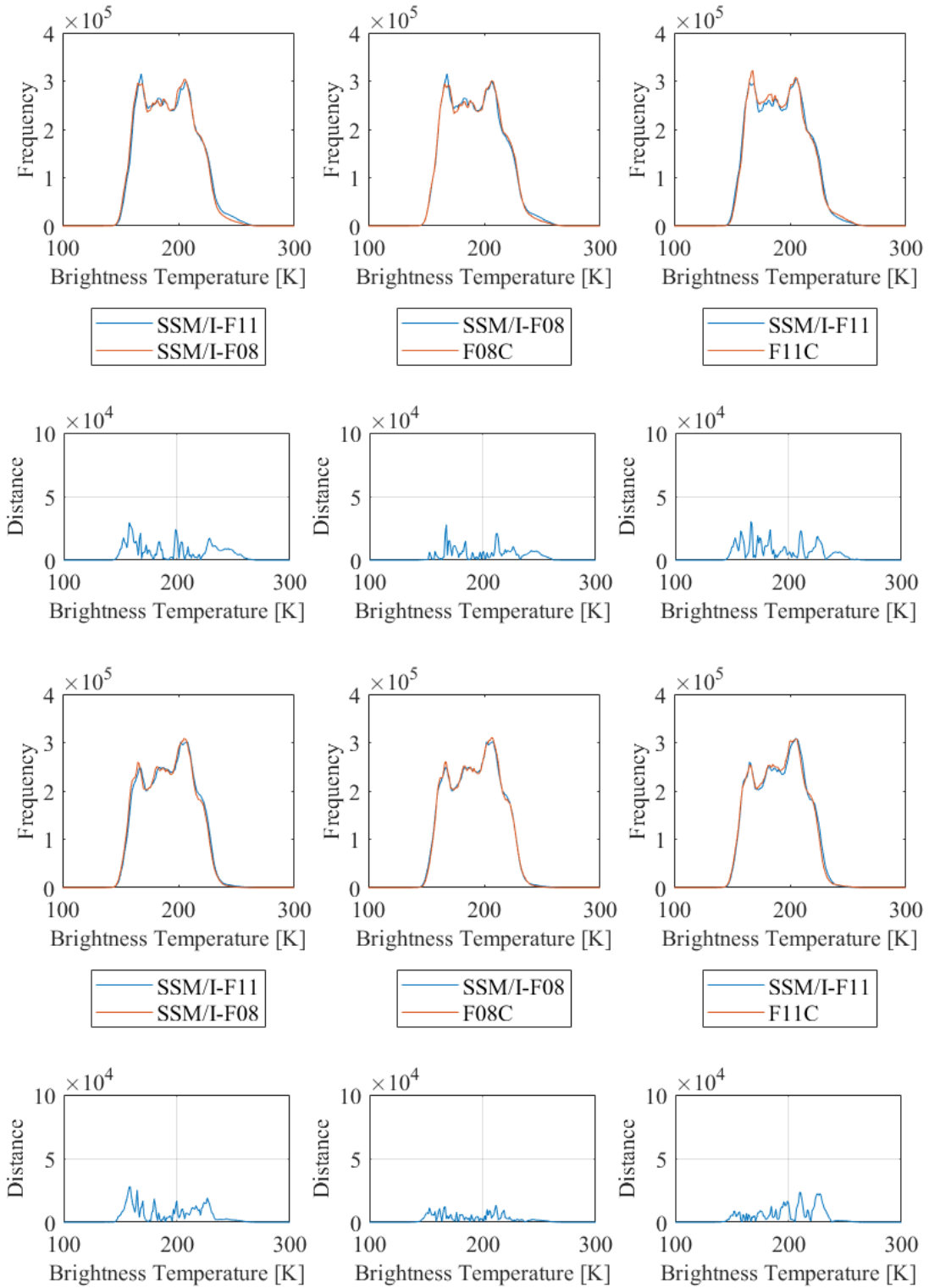


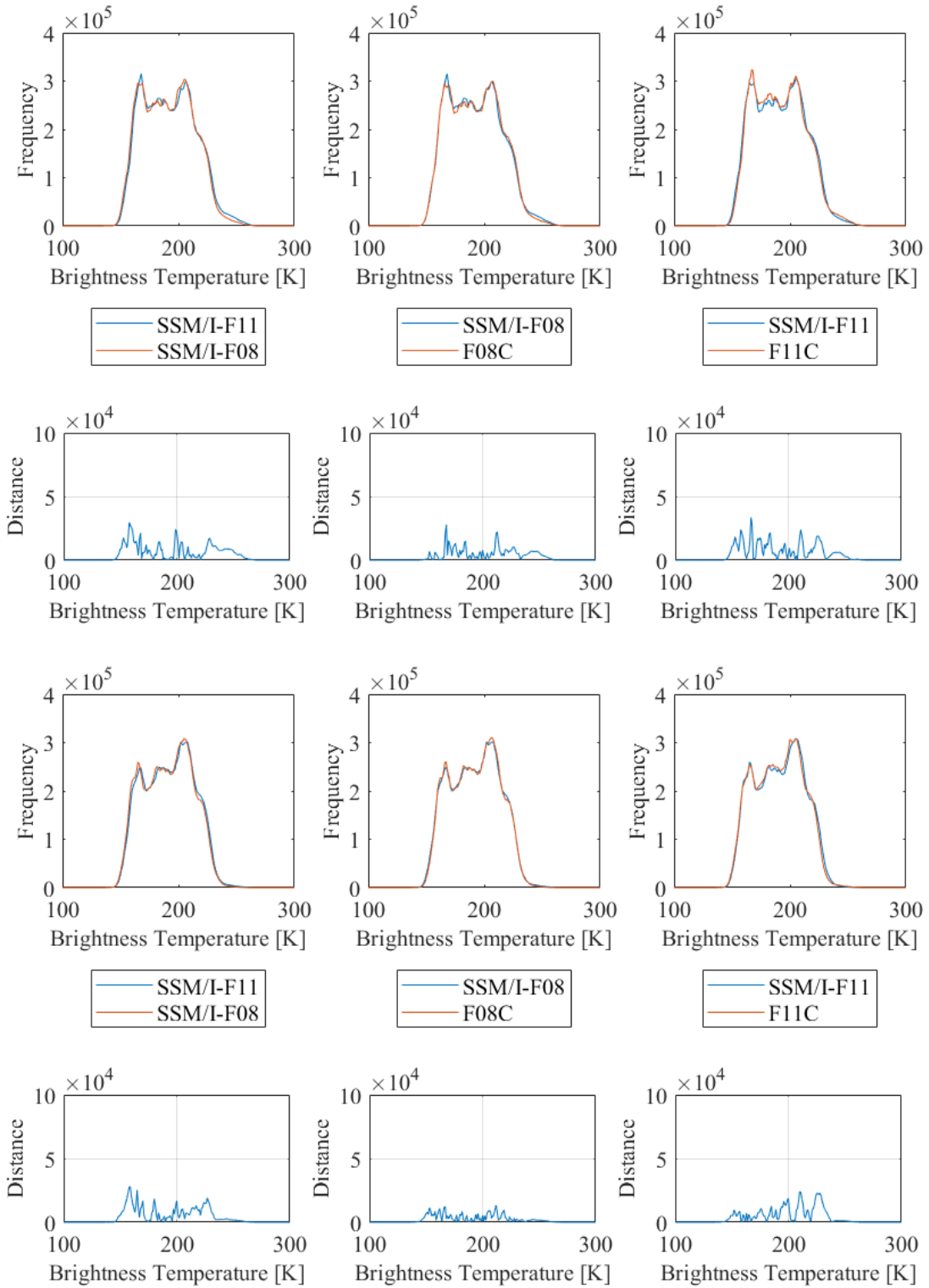
Antarctica

X=F11	m_1	m_2	q_1	q_2	R^2_2	d_1	d_2
Morning	0.9962	0.996	1.7969	1.8349	0.9787	0.4804	0.4901
Evening	1.011	1.0125	-0.9847	-1.2348	0.9774	0.344	0.3232

X=F08	m_1	m_2	q_1	q_2	R^2_2	d_1	d_2
Morning	0.9816	0.9813	2.4734	2.599	0.9787	0.1012	0.085
Evening	0.9683	0.9667	4.982	5.2688	0.9774	0.0135	-0.0094



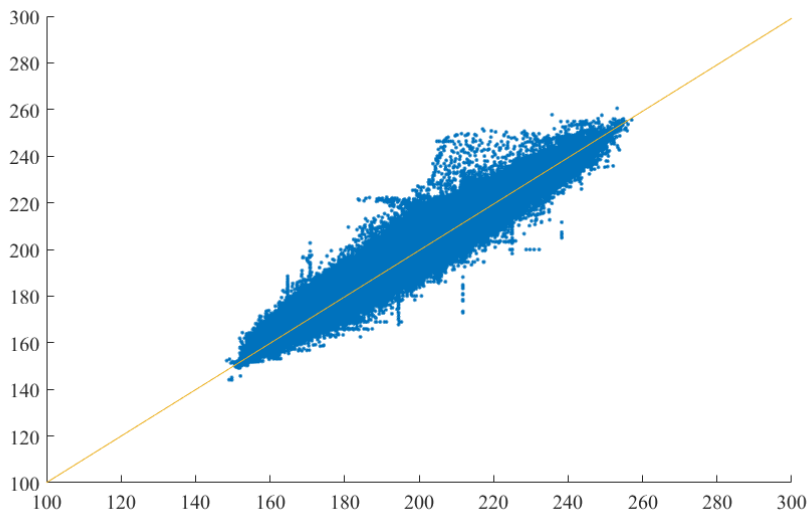
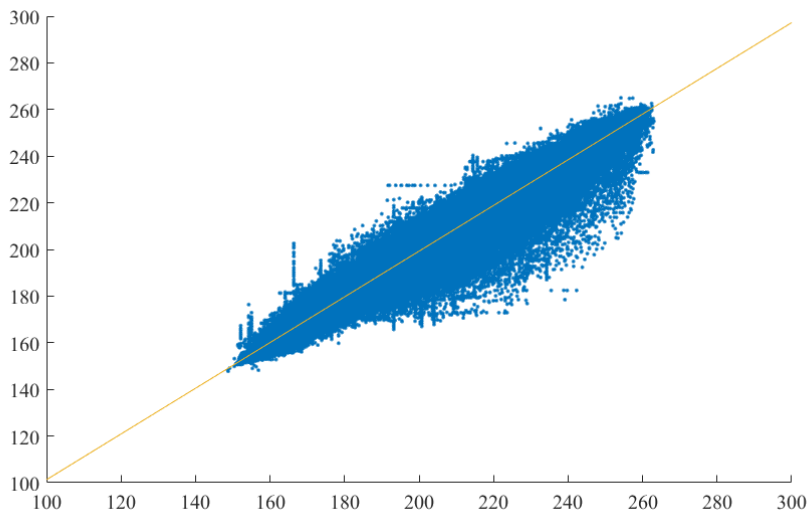


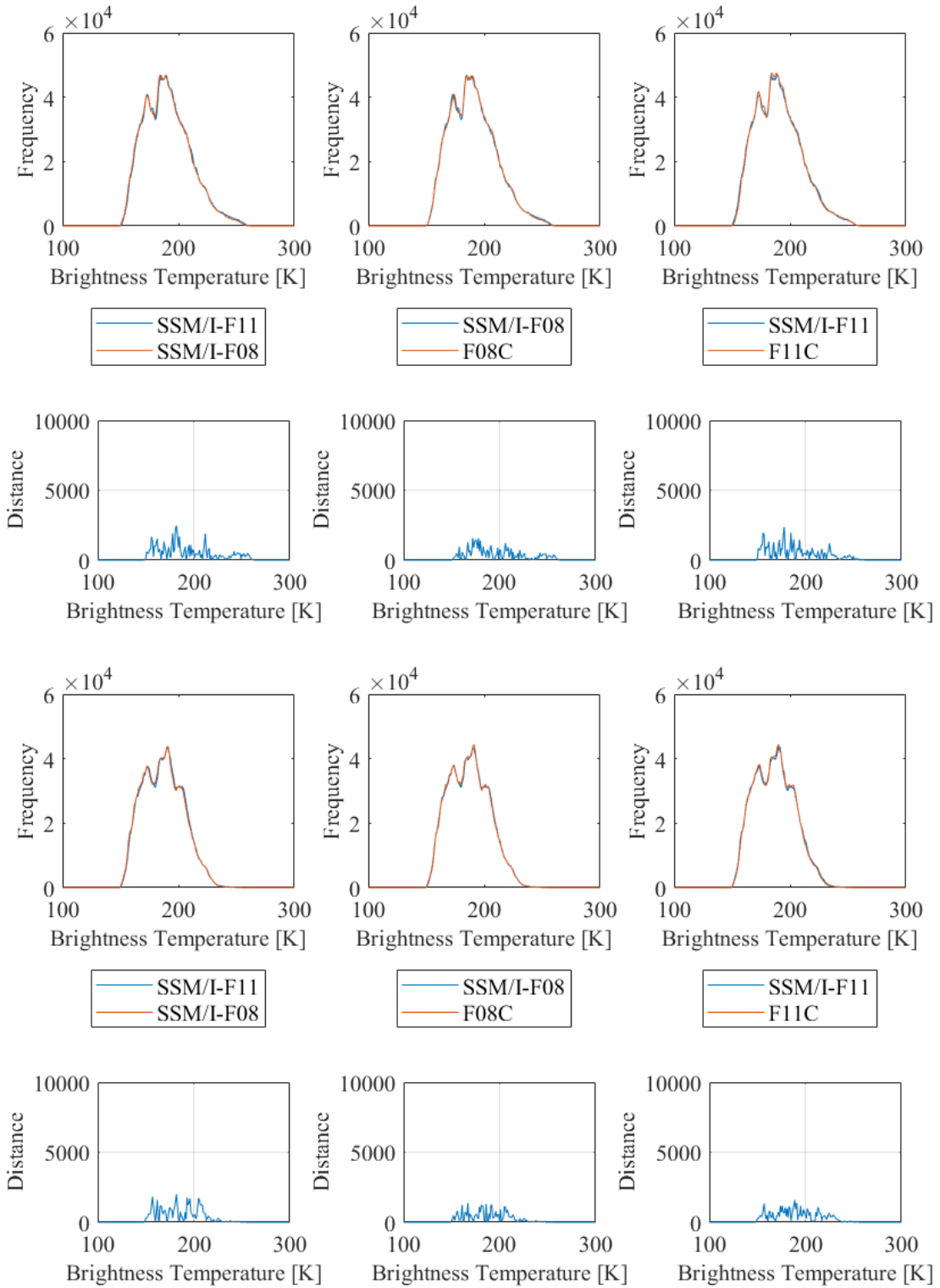


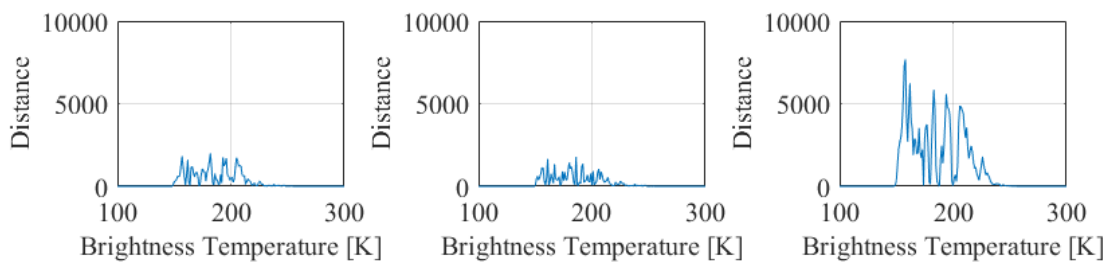
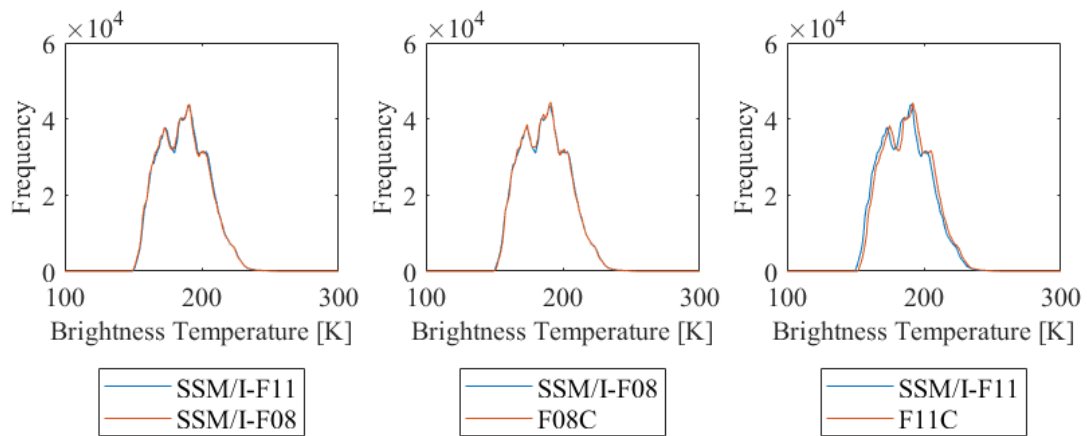
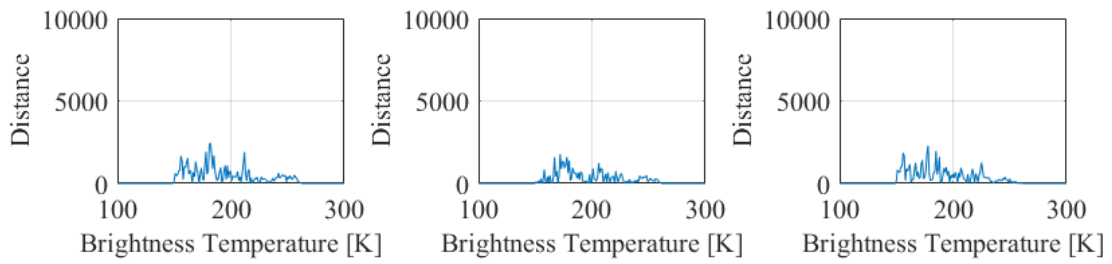
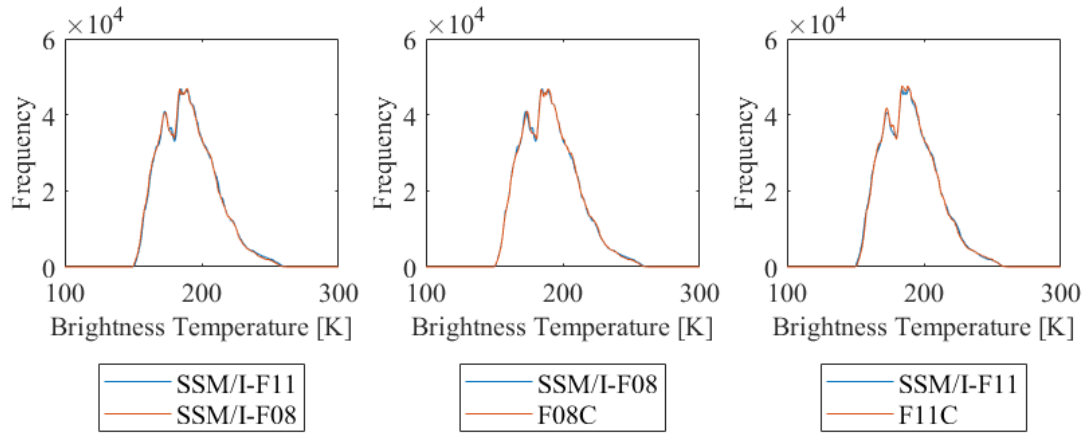
Greenland

X=F11	m_1	m_2	q_1	q_2	R^2_2	d_1	d_2
Morning	0.9912	0.9885	2.0405	2.537	0.9837	0.3112	-2.9053
Evening	0.9982	1.0021	0.9787	-0.00948	0.9819	0.248	0.3101

X=F08	m_1	m_2	q_1	q_2	R^2_2	d_1	d_2
Morning	0.9869	0.9951	2.2303	0.5283	0.9837	0.0988	0.2632
Evening	0.9799	0.9798	3.3319	3.711	0.9819	0.0791	0.1078



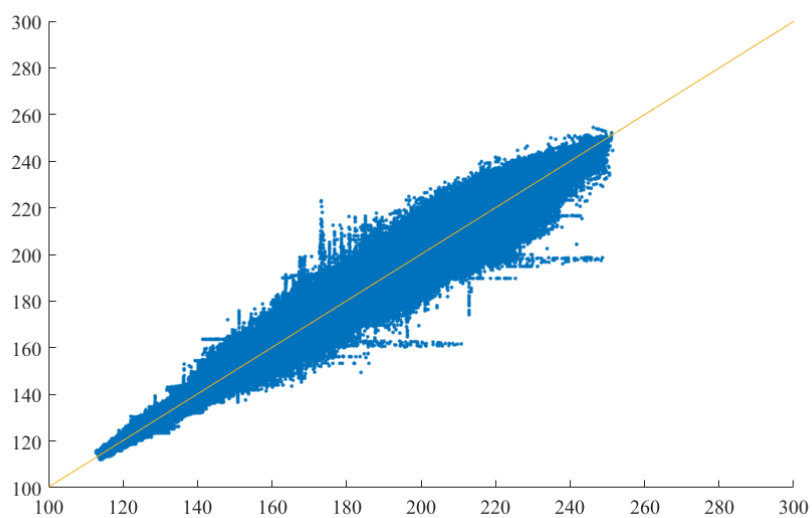
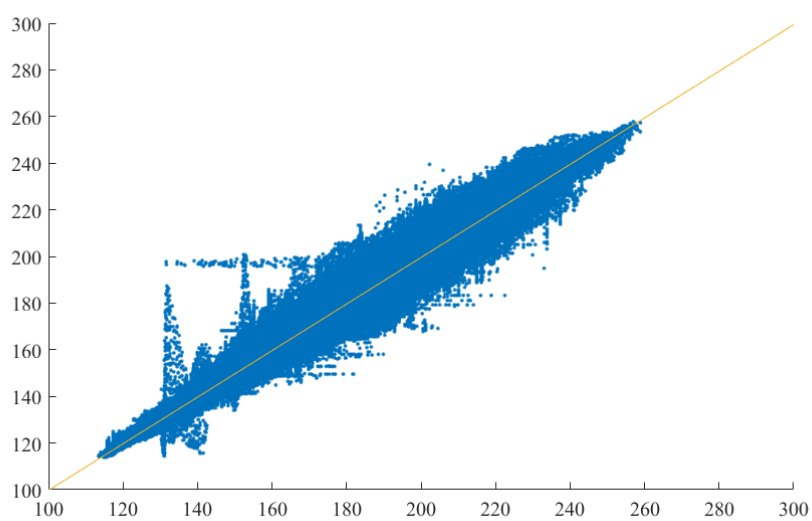


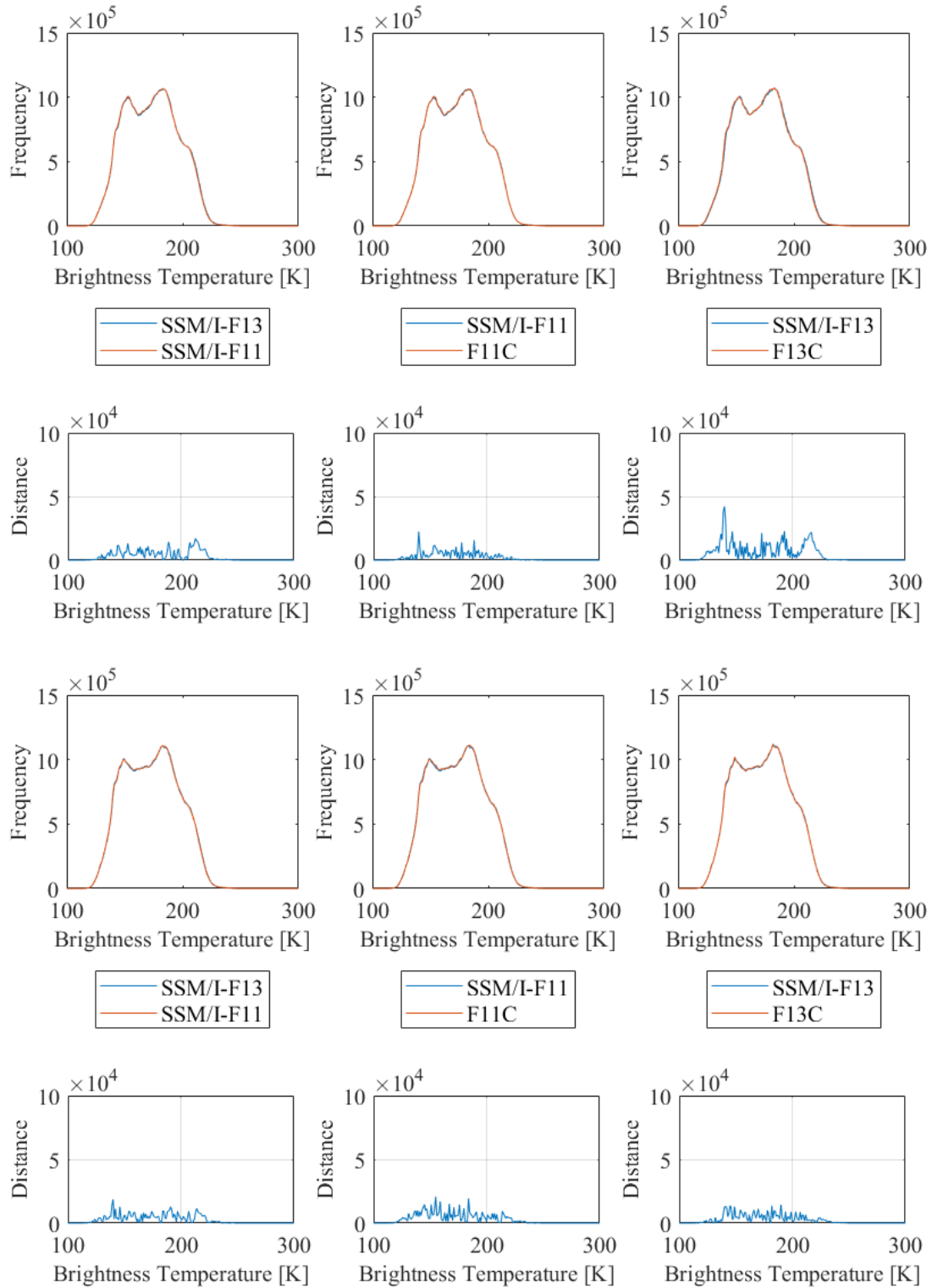


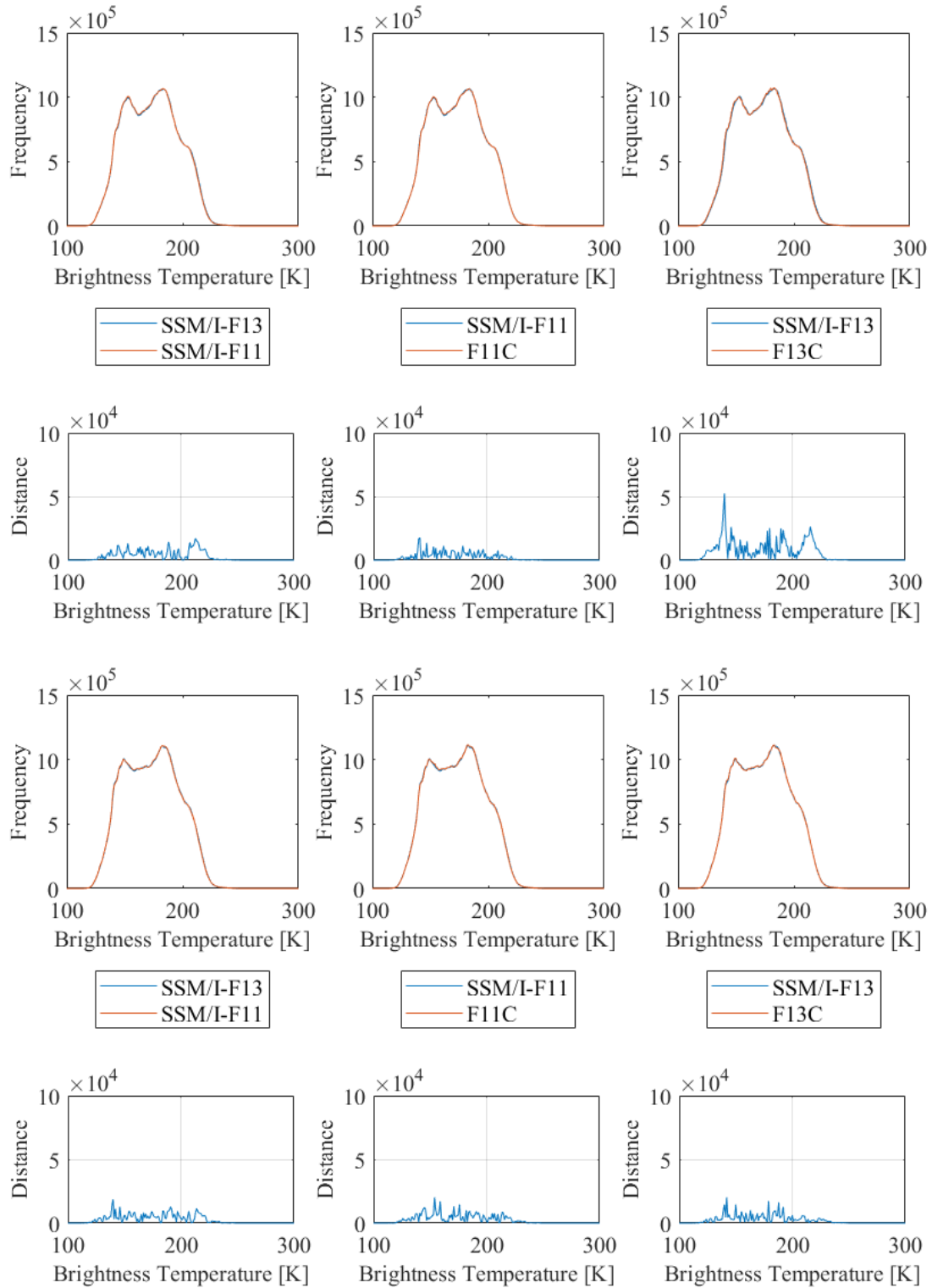
Antarctica

X=F13	m_1	m_2	q_1	q_2	R^2_2	d_1	d_2
Morning	0.9976	0.9976	0.2724	0.2924	0.9958	0.0388	0.1329
Evening	0.9947	0.9949	0.7067	0.6719	0.9967	-0.9685	-0.747

X=F11	m_1	m_2	q_1	q_2	R^2_2	d_1	d_2
Morning	0.9976	0.9982	0.563	0.4298	0.9958	-0.1349	0.0356
Evening	1.0016	1.0018	-0.0662	-0.1045	0.9967	0.2831	0.2558



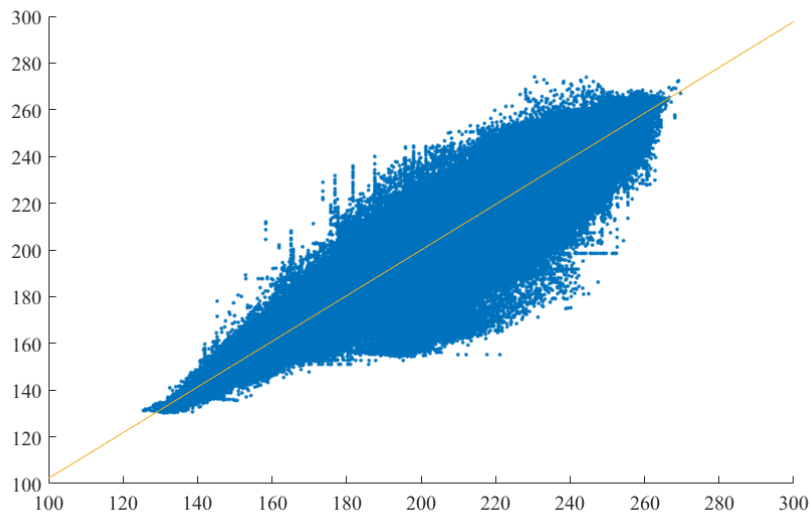
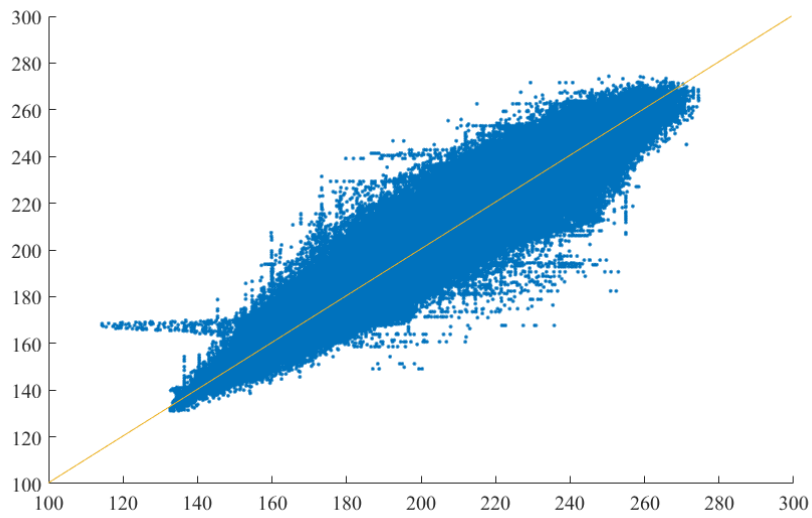


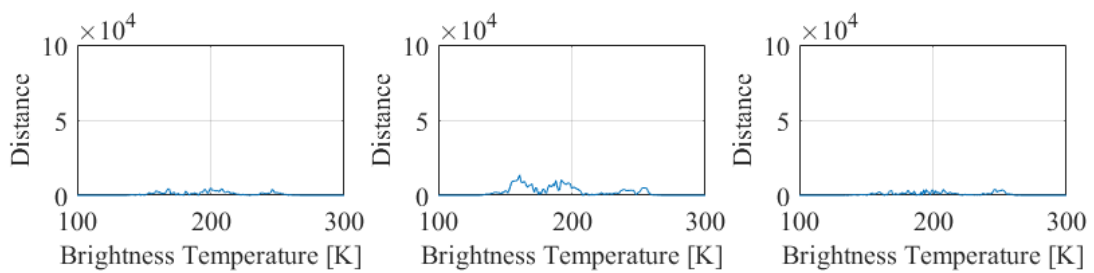
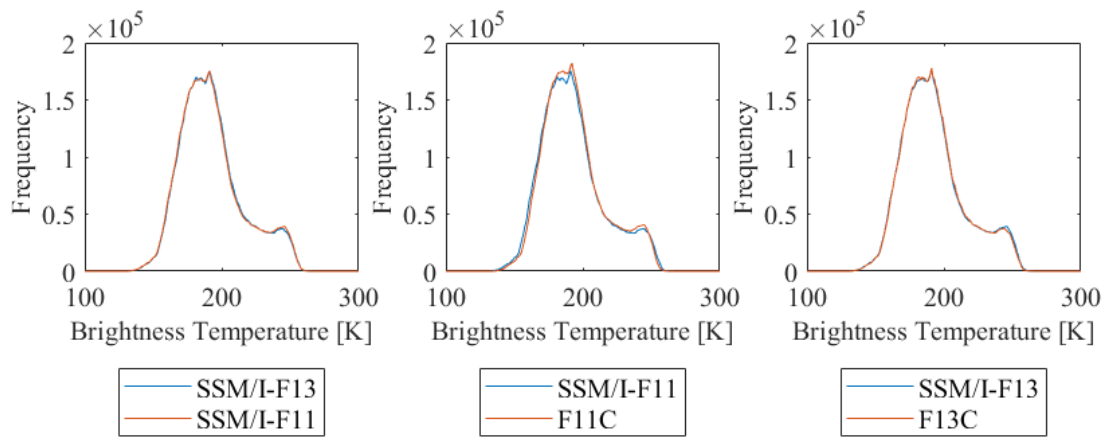
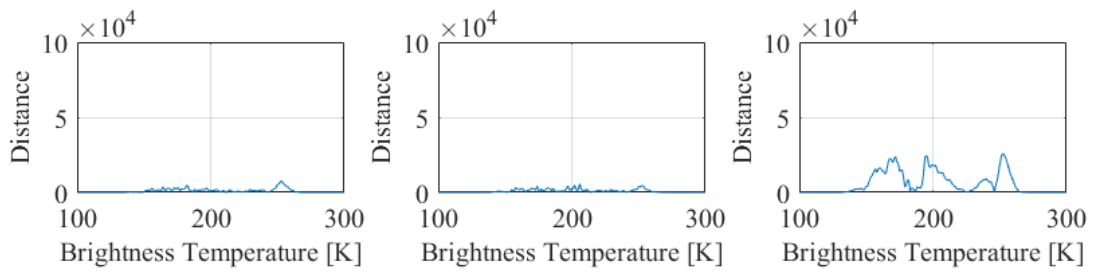
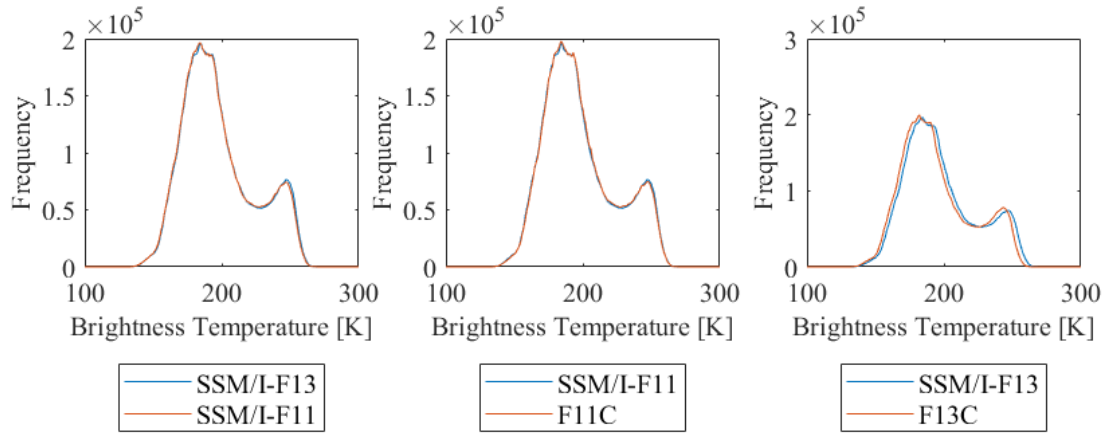


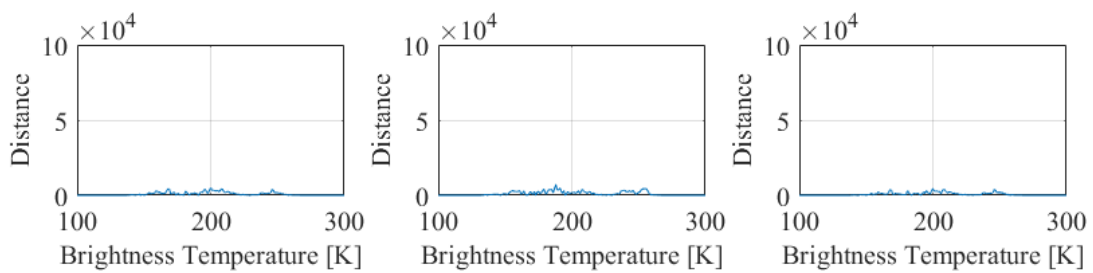
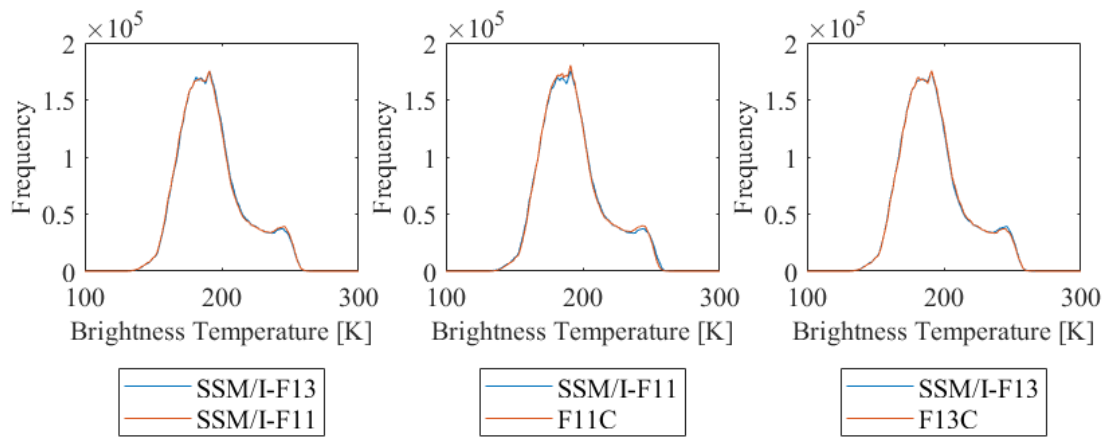
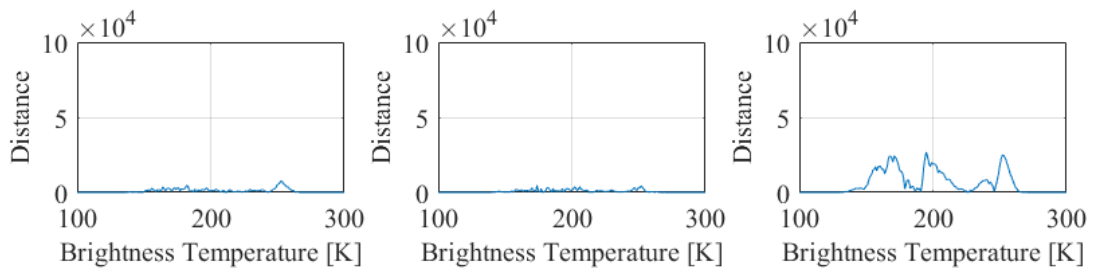
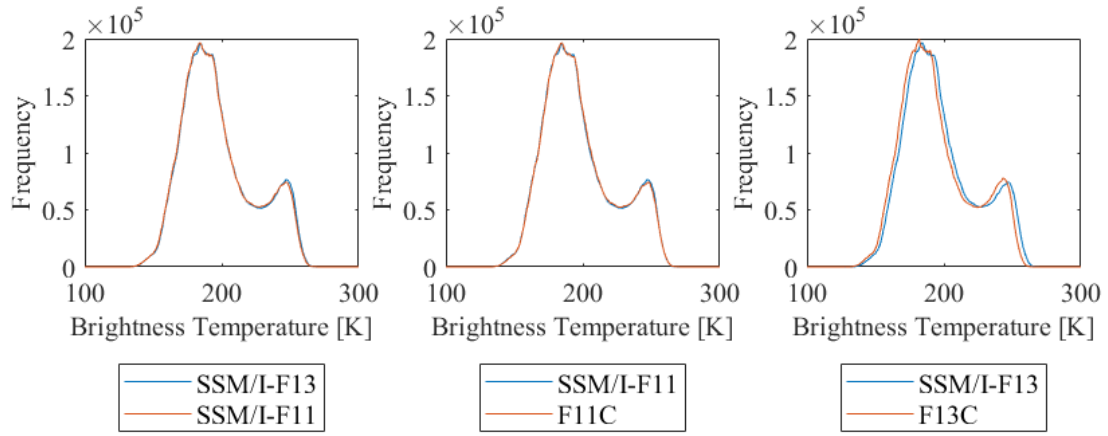
Greenland

X=F13	m_1	m_2	q_1	q_2	R^2_2	d_1	d_2
Morning	0.9955	1.0009	2.3279	-0.2618	0.9782	0.1096	0.1404
Evening	0.9811	0.9853	3.8308	0.1854	0.9868	-4.8218	-4.9828

X=F11	m_1	m_2	q_1	q_2	R^2_2	d_1	d_2
Morning	0.9615	0.9773	8.3219	4.4816	0.9782	-1.7261	-0.3199
Evening	0.9978	1.0015	0.9342	0.1854	0.9868	0.0955	0.2759



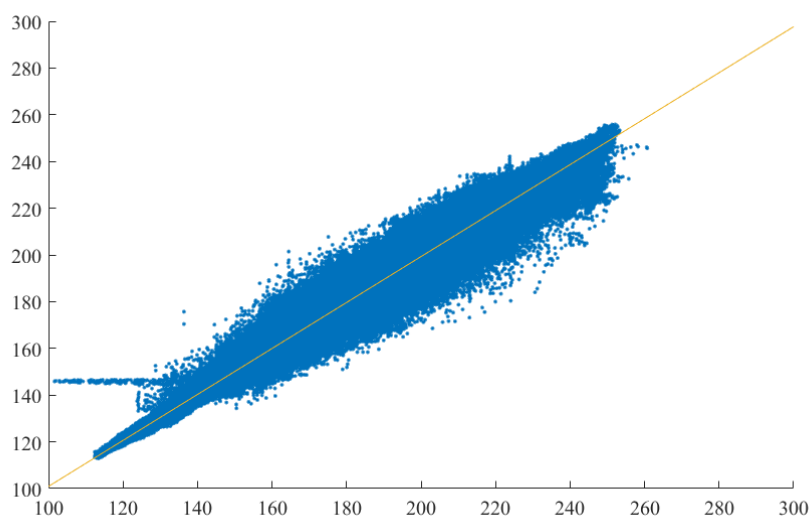
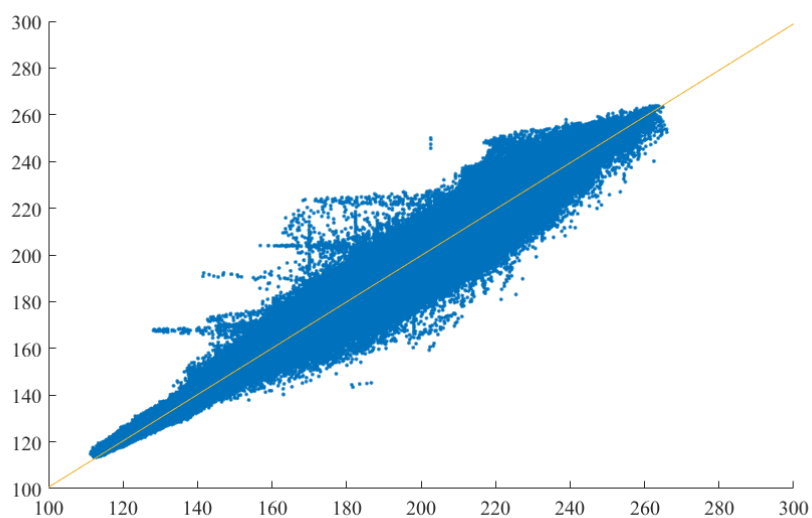


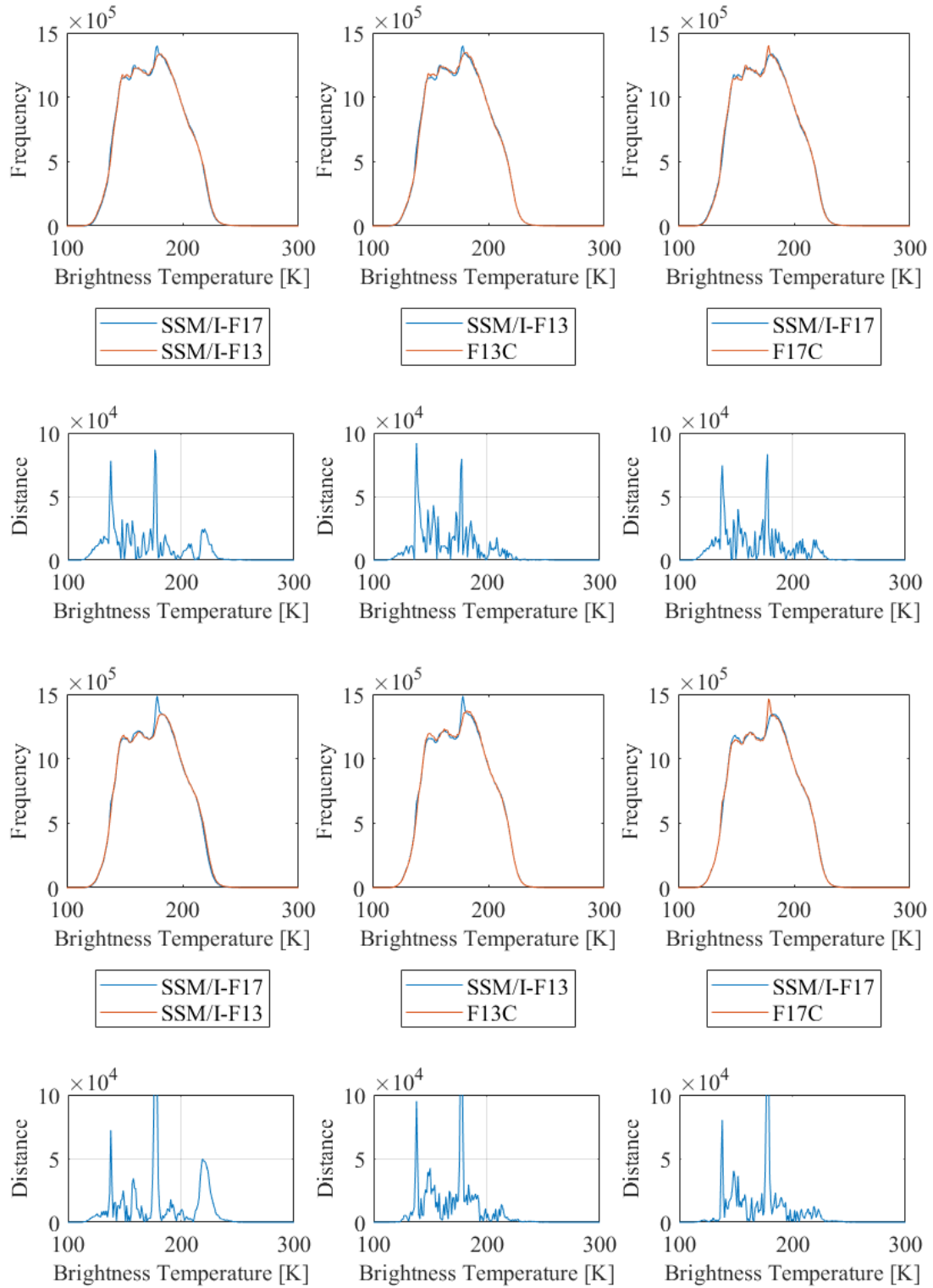


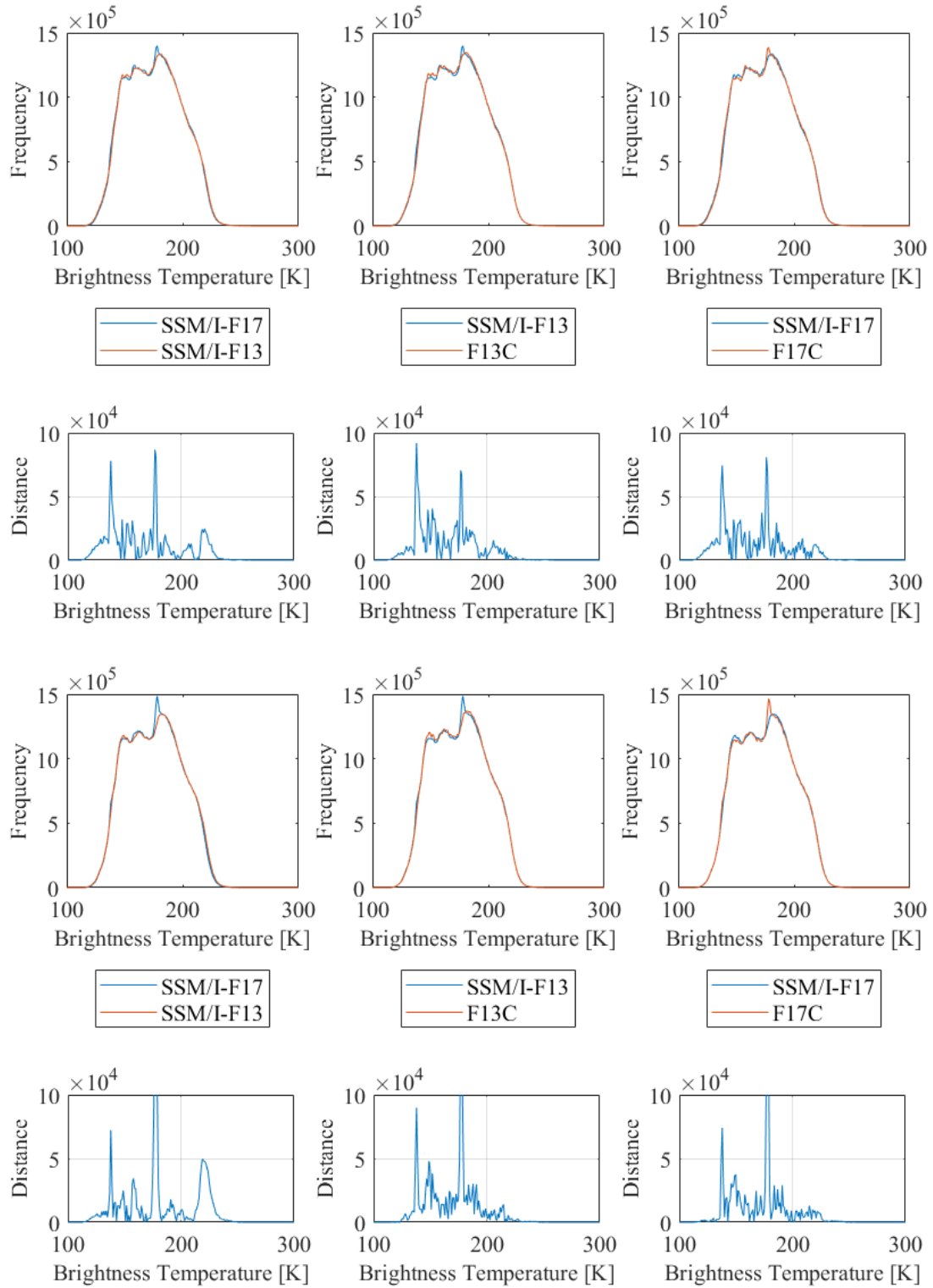
Antarctica

X=F17	m ₁	m ₂	q ₁	q ₂	R ² ₂	d ₁	d ₂
Morning	1.0125	1.0128	-1.9259	-1.9707	0.9963	0.1422	0.146
Evening	1.0036	1.0038	-0.5577	-0.5874	0.9954	-0.00061	0.0092

X=F13	m ₁	m ₂	q ₁	q ₂	R ² ₂	d ₁	d ₂
Morning	0.9839	0.9837	2.5686	2.5966	0.9963	0.2065	0.2044
Evening	0.992	0.9916	1.334	1.3932	0.9954	0.0224	0.0196







Greenland

X=F17	m_1	m_2	q_1	q_2	R^2_2	d_1	d_2
Morning	1.0194	1.0294	-3.0286	-5.0125	0.9809	-0.1086	-0.0045
Evening	1.0039	1.0069	-0.4384	-1.1614	0.9892	0.1403	0.2038

X=F13	m_1	m_2	q_1	q_2	R^2_2	d_1	d_2
Morning	0.959	0.9528	7.2671	8.3701	0.9809	-0.1942	-0.3522
Evening	0.982	0.9824	3.1997	3.2046	0.9892	0.2738	0.2536

